UNIVERSITY OF CALIFORNIA
RIVERSIDE

An Integrated Approach to Cloud Condensation Nuclei Analysis from Various Emissions Sources

A Dissertation submitted in partial satisfaction
of the requirements for the degree of

Doctor of Philosophy

in

Chemical and Environmental Engineering

by

Diep Ngoc Vu

March 2016

Dissertation Committee:
Dr. Akua Asa-Awuku, Chairperson
Dr. David R. Cocker III
Dr. Georgios Karavalakis

The Dissertation of Diep Ngoc Vu is approved:

_____

_____

_____

Committee Chairperson

University of California, Riverside

Acknowledgements

My Parents. Thank you for being my example of hard work, dedication, and love. On the days where I felt like quitting, I would remember that you never did – so, I never did.

My Family. Thank you for walking me to school, for helping me settle into college and then grad school and all the important moments in between; you've always been there to watching over me and encouraging me.

Dr. Akua Asa-Awuku. Thank you for believing in me, for guiding me through the ups and down of graduate school and for leading me towards the right direction when things went astray. You helped me begin my journey at graduate school and then you taught me how to accomplish more than I thought I would ever be able to during my time at UCR.

Dr. David Cocker. Thank you for always being available when I needed your help, your advice/guidance, and of course, all of your support.

Dr. Georgios Karavalakis. You came to me with countless research opportunities. Thank you for having confidence in my abilities.

Dr. Thomas Durbin. Thank you for all of your help and insightful thoughts.

Dr. Daniel Short. You made me smile on my first day here and you continued to make me smile until my very last.

Mr. Kurt Bumiller. I often walked into your office with not-so-great ideas. Thank you for never letting me leave with a bad idea and for never turning me away.

All of my Past and Current Colleagues. Thank you for kindly listening to all of my thoughts and ideas; for supporting the good ones and for gently letting me know which ones were crazy. Except for Daniel, he thought all of my ideas were great. Thank you for never saying ‘no’ when I would ask for help, especially, with all of those special little projects we all knew had a low probability of working. But, because I thought that it might-just-maybe-hopefully work, you still helped me. Thank you!

I would like to acknowledge the following financial support: Environmental Protection Agency Science to Achieve Results Graduate Fellowship, University of California Center on Economic Competitiveness in Transportation Graduate Fellowship, Esther F. Hays Graduate Fellowship, the UCR Department of Chemical and Environmental Engineering, Southern California Air Quality Management District, California Energy Commission, Coordinating Research Council, and the National Science Foundation. The text of Chapter 3, part or in full, is a reprint of the material as it appears in Vu et al. 2015; Integrating Cloud Condensation Nuclei Predictions with Fast Time Resolved Aerosol

Instrumentation to Determine the Hygroscopic Properties of Emissions over Transient Drive Cycles (Aer. Sci. & Tech., 49(11), 1149-1159).

Dedicated to my parents

ABSTRACT OF THE DISSERTATION

An Integrated Approach to Cloud Condensation Nuclei Analysis from Various Emissions Sources

by

Diep Ngoc Vu

Doctor of Philosophy, Graduate Program in Chemical and Environmental Engineering
University of California, Riverside, March 2016
Dr. Akua Asa-Awuku, Chairperson

Aerosols can indirectly effect the radiative balance of the environment by acting as Cloud Condensation Nuclei (CCN) and modifying the microphysical properties of clouds by forming droplets which can either scatter solar radiation back into space, or allow it to pass through and reach the surface of the earth. The potential to activate as CCN and form cloud droplets in the atmosphere is primarily a function of chemical composition and size, and can vary with the aerosol source (i.e. combustion, sea salt, etc.). However, information in regards to the CCN activity of different primary and secondary aerosol sources is limited and not always well defined due to the complexity of the particles. As a result, the aerosol-cloud-climate relationship is not well understood and is the largest source of uncertainty in radiative forcing estimates.

Unique methods to estimate the CCN potential of aerosols derived from different emission sources will be presented. First, a method of analysis to observe and predict the aerosol morphology in CCN activation data for various aerosol compositions

representative of emissions sources was developed to investigate the effect of mixing states on aerosol hygrosocopicity. Next, a method of characterizing rapidly changing particle hygroscopicity generated by vehicles operating over transient drive cycles was developed and utilized to gain information related to the hygroscopicity of emissions derived from the use different biofuels in modern gasoline vehicles. This study was extended to investigate the effect of using biodiesel and renewable diesel fuels in modern diesel vehicles equipped with advanced emissions control technologies on aerosol hygroscopicity and CCN activity. Although modeling atmospheric interactions is highly dependent on source emissions data such as that provided in this work, aerosol emissions from vehicles may be subject to rapid physical and chemical changes during atmospheric aging which can modify the hygroscopic properties. Thus, to assess the effect of atmospheric interactions on chemical and physical CCN transformations a new mobile atmospheric chamber was developed to age and characterize fresh vehicle emissions derived from modern gasoline vehicles. By investigating both fresh and aged emissions, this work presented provides a comprehensive understanding of the aerosol hygroscopicity from the emissions source to its aged state in the atmosphere.

Table of Contents

List of Figures

List of Tables

Chapter 1 – Introduction

1.1. Motivation: Impact of emissions sources on the aerosol indirect effect

Primary aerosols are emitted directly into to the atmosphere from a variety of biogenic or anthropogenic emissions sources. Whereas secondary aerosols occur during atmospheric aging processes such as the oxidation and gas-to-particle partitioning of low volatile organic compounds. These atmospheric aerosols can act as Cloud Condensation Nuclei (CCN) and modify the microphysical properties of clouds by forming droplets that scatter solar radiation back into space, or allow it to pass through and reach the surface of the earth. The potential of these aerosols to activate as CCN is primarily a function of chemical composition, size and morphology and vary with the emissions source (Dusek et al. 2006). However, there is limited information on the CCN activity of various primary and secondary sources due to the complexity of the particles. As a result, the aerosol-cloud-climate relationship is not well understood and is the largest source of uncertainty in radiative forcing estimates (IPCC, 2013). Thus, research on the CCN activity of various emissions sources is required to fill the information gap and better understand the impact of different emissions sources on aerosol chemistry and cloud interactions.

Sources that will be explored in this work include combustion aerosol or black carbon (BC) which can originate from incomplete combustion of fuel from engines, inorganic salts typically found in the atmosphere, other primary aerosols, and secondary aerosols (SA) which form from nucleation, condensation and the oxidation of volatile organic compounds (Hallquist et al, 2009). BC concentrations in the atmosphere have steadily increased over the last century, therefore, it is vital to quantify the mixing behavior

of BC and other constituents present in the atmosphere (Lamarque et al., 2010). BC is generally considered to be hydrophobic and not CCN active. However, even small amounts of soluble material (i.e. an inorganic salt such as sodium chloride) or slightly soluble material (water soluble organic carbon) can have a significant effect on the water uptake properties of insoluble compounds when internally mixed (Dusek et al., 2006; Bilde et al., 2004). For example, water soluble organic carbon (WSOC) has the ability to promote CCN activity by contributing solute and serving as a surfactant with the potential to depress surface tension (Shulman et al. 1996) thereby lowering the required critical supersaturation to activate and increasing CCN. However, it has also been observed to hinder CCN activity by lowering the rate at which water condenses onto the droplet (Asa-Awuku et al. 2007). And, if mixed with a highly soluble inorganic salt that readily deliquesces, the aerosol hygrosocopicity can be greatly enhanced and the effect of the WSOC may not be observed (e.g., but not limited to, Padro et al., 2012; Svenningsson et al., 2005; Cruz and Pandis, 1998). Accounting for mixing state and extent of mixing can greatly improve CCN concentration predictions (e.g., but not limited to, Padró et al.; 2013, Wex et al., 2010). However, ambient aerosols generally exist as complex heterogeneous mixtures of different species where the hygroscopic or water uptake properties of aerosols may be significantly different from their individual components. Thus, determining the CCN activity of internally mixed multiple component aerosols and mixing behavior still remains highly complex and not clearly understood, and thus is an active area of research.

Recent work indicates the addition of oxygenated biofuels and renewable fuels could modify the hygroscopic properties of diesel emissions (Happonen et al., 2013) and

gasoline emissions (Short et al., 2015); the latter of which exhibited potentially high CCN activity. As emissions regulations become more stringent, the demand for engine modifications and after treatment technology that can reduce gas phase and/or particulate phase pollution continues to grow. However, the chemical and physical properties of vehicles emissions are highly dependent on the type of control technology, fuel, and driving conditions. Thus the contribution of emissions derived from new vehicle technologies and fuel formulations from transient vehicle studies to the CCN budget is currently not well known. Fresh emissions may not directly play a large role in regional indirect effects, however modeling atmospheric interactions is highly dependent on source emissions data, as it is necessary to be able to account for atmospheric interactions such as transport, coagulation, transformations, etc. Information in regards to the amount and how CCN active these primary emissions are important as it provides a measure of their direct contribution into the atmosphere and can aid in predicting its behavior in the presence of other species.

Fresh vehicle emissions have been characterized with hydrophobic properties, which will inhibit the uptake of water and limit the ability to activate as cloud droplets. However, at regional scales where the aerosols have undergone atmospheric aging, the hygroscopicity can be modified under atmospheric conditions, such as oxidation and the condensation of soluble materials (Wittbom et al., 2014) and can exhibit higher CCN activity (Asa-Awuku et al.,2011). This suggests that the aging of vehicle emission aerosols could exhibit different physical and chemical properties than the fresh aerosols emitted from the vehicle tailpipe.

Vehicle emissions are a large source of secondary organic aerosol (SOA) precursors in urban regions, where gasoline derived SOA dominates over diesel derived SOA (Bahreini et al., 2012). This is consistent with chamber studies investigating large SOA to POA ratios for gasoline vehicle emissions (e.g., but not limited to, Nordin et al., 2014; Gordon et al., 2014, Platt et al., 2013). However, many of these studies focused more on the older technology vehicles, such as Port Fuel Injection (PFI) vehicles, with less attention on current generation vehicles such as gasoline direct injection (GDI) vehicles. With the push to reduce fuel consumption, GDI technology is estimated to become the preferred standard for gasoline light-duty vehicles in both the United States (CARB, 2010). However, because of the direct injection of fuel into the combustion chamber, fuel impingement on the piston walls during combustion could lead to higher soot formation and total hydrocarbons emissions, which is a drawback of GDI technology (Karavalakis et al., 2014). This effect may be more prominent during cold starts when the three way catalyst (TWC) is cold and the oxidation efficiency is low.

Because the chemical and physical properties of gasoline emissions can vary with the different vehicle types, fuel sources, and driving conditions, research in regards to atmospherically processed vehicle emissions derived from GDI vehicles needs to be investigated. These aged aerosols can impact regional visibility and modify clouds, thus it is important to understand the fresh vehicle emissions, but also the evolution of these fresh vehicle emissions as their hygroscopic properties are modified downwind from the tailpipe.

1.2. Outline of Dissertation

Chapter 2 investigates the influence of mixing state on activation curves to improve the experimental CCN activation analysis techniques of complex mixtures. A method of CCN data analysis for multicomponent mixtures of varying mixing states and its relationship to activation curves consisting of one or more activation points was developed using simplified two component systems of varying solubility generated under internal and external mixing conditions. κ-Köhler theory predictions were completed for different organic and inorganic mixtures and compared to experimentally derived kappa values and respective mixing states.

The work in chapter 3 investigates a fast-resolved closure method to capture the Cloud Condensation Nuclei (CCN) properties of aerosol by operating an Engine Exhaust Particle Sizer (EEPS, 10Hz) in parallel with a Continuous Flow Streamwise Thermal Gradient CCN Counter (CCNC). Current methods to measure relevant particle distributions have scan times that may be too long to capture the physical and chemical changes of the aerosol emitted. This is because scanning electrical mobility measurements require scan times longer than the time in which an instantaneous vehicle acceleration occurs to obtain a full size distribution, which may not be ideal for transient testing. To bypass this limitation, traditional CCN measurements were integrated with fast time resolved aerosol sizing instrumentation to characterize CCN properties. With improved scanning speed, size distributions can be measured at a much higher frequency and used for closure studies to characterize the fast changing hygroscopic properties of emissions.

Chapter 4 investigates the impact of various biodiesel and renewable diesel fuels on the supersaturated hygroscopic properties of emissions downstream of light duty vehicles equipped with direct injection diesel engines and advanced emission control technologies while operating on alternative fuels. They were tested over two transient drive cycles; Federal Test Procedure (FTP) and Highway Fuel Economy Test Cycle. The fuels in this study include a Federal ultra-low sulfur diesel (FED ULSD), a California Air Recourses Board (CARB) ULSD, fatty acid methyl esters (FAMEs), commonly known as biodiesel, produced from soybean oil (SME), waste cooking oil (WCO), and animal fat oil (AFME), respectively, and a hydrogenated vegetable oil (HVO). The second objective of this study was to evaluate the impact of advanced emissions control DPF regeneration on aerosol hygroscopicity. Emission control technologies have been demonstrated to effectively reduce diesel emissions, rates. However, under certain operating conditions, such as DPF regenerations, there are significantly more particle emissions and particle hygroscopicity may be greatly modified. Several studies have investigated the changes in physical and chemical properties of aerosols derived during DPF regeneration, but there has been little attention on the particle hygroscopicity.

Chapter 5 investigates the SOA forming potential of emissions generated from a fleet of modern technology GDI vehicles operating under realistic driving conditions. The exhaust for each vehicle was collected in Center for Environmental Research and Technology (CE-CERT) new Mobile Atmospheric Chamber (MACh) while driven over the Unified Cycle (UC) using a chassis dynamometer and subsequently, photochemically aged. Real-time particle and gaseous phase measurements were collected to characterize

the chemical and physical properties of the aged emissions. Details of the characterization of a new mobile atmospheric chamber (MACh) and the effect of photochemically aging emissions for two modern light duty passenger GDI vehicles while operating on a chassis dynamometer.are presented. Chapter 6 extends on the GDI SOA characterization by investigating the SOA forming potential of two additional GDI vehicles. And lastly, Chapter 7 concludes the findings of this dissertation work.

1.1 References

Asa-Awuku, A., and Nenes, A. (2007). Effect of solute dissolution kinetics on cloud droplet formation: Extended Köhler theory, J. Geophys. Res., 112, D22201, doi:10.1029/2005JD006934.

Bilde, M. and Svenningsson, B. (2004). CCN activation of slightly soluble organics: the importance of small amounts of inorganic salt and particle phase. Tellus B, 56(2), 128-134, doi:10.1111/j.1600-0889.2004.00090.

Cruz, C. N. and Pandis, S. N. (1998). The effect of organic coatings on the cloud condensation nuclei activation of inorganic atmospheric aerosol, J. of Geo. Res., 103(D11), 13111-13123.

Dusek, U., G. P. Frank, L. Hildebrandt, J. Curtius, J. Schneider, S. Walter, D. Chand, F. Drewnick, S. Hings, D. Jung, S. Borrmann, and M. O. Andreae (2006b). Size matters more than chemistry for cloud-nucleating ability of aerosol particles. Science, 312 (5778) 1375–1378.

Gordon, T. D., Presto, A. A., May, A. A., Nguyen, N. T., Lipsky, E. M., Donahue, N. M., Gutierrez, A., Zhang, M., Maddox, C., Rieger, P., Chattopadhyay, S., Maldonado, H., Maricq, M. M., and Robinson, A. L. (2014). Secondary organic aerosol formation exceeds primary particulate matter emissions for light-duty gasoline vehicles, Atmos. Chem. Phys., 14, 4661-4678, doi:10.5194/acp-14-4661-2014.

Hallquist, M., Wenger, J. C., Baltensperger, U., Rudich, Y., Simpson, D., Claeys, M., Dommen, J., Donahue, N. M., George, C., Goldstein, A. H., Hamilton, J. F., Herrmann, H., Hoffmann, T., Iinuma, Y., Jang, M., Jenkin, M. E., Jimenez, J. L., Kiendler-Scharr, A., Maenhaut, W., McFiggans, G., Mentel, Th. F., Monod, A., Prévôt, A. S. H., Seinfeld, J. H., Surratt, J. D., Szmigielski, R., and Wildt, J. (2009). The formation, properties and impact of secondary organic aerosol: current and emerging issues, Atmos. Chem. Phys., 9, 5155-5236, doi:10.5194/acp-9-5155-2009.

Happonen, M., Heikkilä, J., Aakko-Saksa, P., Murtonen, T., Lehto, K., Rostedt, A., Sarjovaara, T., Larmi, M., Keskinen, J., and Virtanen, A. (2013). Diesel exhaust emissions and particle hygroscopicity with HVO fuel-oxygenate blend, Fuel 103:380-386, doi:10.1016/j.fuel.2012.09.006.

IPCC, 2013: Summary for Policymakers. In: Climate Change 2013: The Physical Science Basis. Contribution of Working Group I to the Fifth Assessment Report of the Intergovernmental Panel on Climate Change [Stocker, T.F., D. Qin, G.-K. Plattner, M. Tignor, S.K. Allen, J. Boschung, A. Nauels, Y. Xia, V. Bex and P.M. Midgley (eds.)]. Cambridge University Press, Cambridge, United Kingdom and New York, NY, USA.

Köhler, H. (1936), The nucleus in and the growth of hygroscopic droplets, Transactions of the Faraday Society, 43, 1152.

Lamarque, J.-F., et al. (2010). Historical (1850–2000) gridded anthropogenic and biomass burning emissions of reactive gases and aerosols:Methodology and application, Atmos. Chem. Phys., 10, 7017–7039, doi:10.5194/acp-10-7017-2010.

Nordin, E. Z., Eriksson, A. C., Roldin, P., Nilsson, P. T., Carlsson, J. E., Kajos, M. K., Hellén, H., Wittbom, C., Rissler, J., Löndahl, J., Swietlicki, E., Svenningsson, B., Bohgard, M., Kulmala, M., Hallquist, M., and Pagels, J. H. (2013). Secondary organic aerosol formation from idling gasoline passenger vehicle emissions investi gated in a smog chamber, Atmos. Chem. Phys., 13, 6101–6116, doi:10.5194/acp-13-6101-2013.

Padró, L. T., Moore, R. H., Zhang, X., Rastogi, N., Weber, R. J., and Nenes, A. (2012). Mixing state and compositional effects on CCN activity and droplet growth kinetics of size-resolved CCN in an urban environment, Atmos. Chem. Phys., 12, 10239-10255, doi:10.5194/acp-12-10239-2012.

Platt, S. M., El Haddad, I., Zardini, A. A., Clairotte, M., Astorga, C., Wolf, R., Slowik, J. G., Temime-Roussel, B., Marchand, N., Ježek, I., Drinovec, L., Močnik, G., Möhler, O., Richter, R., Barmet, P., Bianchi, F., Baltensperger, U., and Prévôt, A. S. H. (2013). Secondary organic aerosol formation from gasoline vehicle emissions in a new mobile environmental reaction chamber, Atmos. Chem. Phys., 13:9141-9158, doi:10.5194/acp-13-9141-2013.

Short, D., Vu, D., Durbin, T., Karavalakis, G., and Asa-Awuku, A. (2015). Particle Speciation of Iso-Butanol and Ethanol Blended Gasoline in Light-Duty Port Fuel Injection, Vehicles, J. of Aerosol Sci. 84:39-52.

Shulman, M., M. Jacobson, R. Charlson, R. Synovec, and T. Young (1996), Dissolution behaviour and surface tension effects of organic compounds in nucleating cloud droplets, Geophys. Res. Lett., 23, 277– 280.

Svenningsson, B., Rissler, J., Swietlicki, E., Mircea, M., Bilde, M., Facchini, M. C., Decesari, S., Fuzzi, S., Zhou, J., Mønster, J., and Rosenørn, T. (2006). Hygroscopic growth and critical supersaturations for mixed aerosol particles of inorganic and organic compounds of atmospheric relevance, Atmos. Chem. Phys., 6, 1937-1952, doi:10.5194/acp-6-1937-2006.

Chapter 2 - External and Internal CCN Mixtures: Defining Experimental Data and Analysis

2.1 Introduction

Atmospheric cloud condensation nuclei (CCN) are comprised of complex heterogeneous mixtures of organic and inorganic compounds. The chemical and physical diversity present in these complex mixtures can greatly complicate the quantification of aerosol cloud interactions, thereby making it difficult to predict CCN activity. However, knowledge of the mixing state and the chemical composition can greatly improve CCN predictions and has been the focus of several studies (e.g. but no limited to, Liu et al, 2012; Padro et al., 2012; Svenningsson et al., 2005; Henning et al., 2005; Abbatt, et al., 2005; Bilde and Svenningsson, 2003).

It is well accepted that the water content and the point of activation is dependent on more factors than just the critical supersaturation and dry diameter for CCN active aerosols (Petters and Kreidenweis, 2007). The mixing state and level of mixing can substantially influence CCN activity. The droplet growth and activation of slightly soluble organics can be substantaially modified with internally mixed with an inorganic salts that readily deliquesces (e.g., but not limited to, Padro et al., 2012; Svenningsson et al., 2005; Cruz and Pandis, 1998). Although inorganic salts are well characterized, the quantification of CCN activity is complicated when they're internally mixed with a complex organic. Thus, simple mixing rules may no longer be appropriate. It has been observed that mixed aerosols can activate at lower supersaturations than their bulk constituents and organic compounds that may not traditionally be considered as water soluble may aid in the formation of a cloud

droplet by acting as a surfactant, depressing surface tension, or simply by contributing mass (Padro et al., 2007; Svenningsson et al., 2006; Facchini et al, 2000; Cruz and Pandis, 1998). In addition, the deliquescent limitation is removed when there's a sufficiently large enough fraction of salt which allows the slightly soluble core to dissolve before activation, thus lowering the required supersaturation (Sullivan et al. 2009).

To help minimize the complexity in characterizing aerosol water uptake properties, CCN data analysis has been simplified by assuming that a) the aerosols share a similar or uniform hygrosocopicity, b) the CCN data sets consist of large fractions of doubly charged aerosols and c) all CCN active aerosols have unlimited solubility. As a result, a single sigmoidal fit is applied over the entire aerosol sample containing aerosolized organic/inorganic aqueous solutions, assuming that the first sigmoid fully consisted of multiply-charged particles. However, this method of analysis may not be fully representative of the different hygroscopicities present in the aerosol sample.

Previous studies addressed aerosols with singular or internally mixed binary chemical species (Petters and Kredenweiss, 2007; Shulman et al. 1996, Bilde and Svenningsson 2004, Sullvian et al. 2009, Broekhuizen et al., 2004). However, ambient measurements indicate complex aerosol populations consisting of both external and internal mixtures (e.g., but not limited to, Lance et al., 2012; Padró et al., 2012; Ervens et al., 2007). By accounting for the mixing states and extent of mixing, CCN concentration predictions can be greatly improve (Padró et al.; 2013, Wex et al., 2010).

In this work, we seek to improve the experimental CCN activation analysis techniques of complex mixtures by investigating the influence of mixing state on activation curves.

To understand the impact of mixing state on CCN activation, simplified two component mixtures with varying hygroscopicities were created under both internal and external mixing conditions. In addition, the hygroscopic properties of black carbon mixed with atmospherically relevant constituents of varying hygroscopicity were investigated.

2.2 κ-Köhler Theory

Using the generalized κ-Köhler equation presented by Petters and Kredenweiss (2007 and 2008), droplet growth in the supersaturated regimes for a selected dry diameter can be modelled for an aerosol assuming infinite solubility.

$$lnS_c = \left(\frac{4A^3\rho_w M_s}{27v\rho_s M_w D_d^3}\right)^{1/2}, \quad where\ A = \frac{4\sigma_{s/a}M_w}{RT\rho_w} \qquad (1)$$

$$\kappa = \frac{4A^3}{27D_d^3 ln^2 S_c} \qquad (2)$$

$\sigma_{s/a}$ is the surface tension, M_w is the molecular weight of water, R the universal gas constant, T is the temperature at activation, and ρ_w is the density of water. Surface tension and density of water were calculated according to temperature dependent parameterizations presented by Seinfeld and Pandis (1998) and Pruppacher and Klett (1997) (Rose et al., 2008). The surface tension of the solution is assumed to be that of pure water.

2.3 Experimental

2.3.1 Aerosol Sources

The CCN activity of two component aerosol mixtures under internal and external mixing conditions were investigated in this study. A Collison-type atomizer generated singular-component solutions of ammonium sulfate, ($(NH_4)_2SO_4$, Acros 99.5%), sodium chloride, (NaCl, Acros 99+%) and succinic acid ($C_4H_6O_4$, Acros 99%) and subsequent internal mixture combinations as described in Sect. 4.2.1. All solutions were prepared using Millipore© DI water (18 mΩ, < 100ppb). Atomized wet droplets are dried with a heated column and a silica gel diffusion dryer. Succinic acid, classified as a slightly soluble dicarboxylic acid (Saxena and Hildeman, 1996), $(NH_4)_2SO_4$, and NaCl are all relevant model atmospheric compounds with varying degrees of solubility and hygroscopcity. An AVL Particle Generator, (APG) was used to generate black carbonaceous soot. It consists of a propane burner followed by a volatile particle remover. The burner was operated at 400°C with a propane and air flow rate of 15 ml/min and 1.0 l/min, respectively. The structure of agglomerates of spherical soot particles generated by the APG is similar to soot derived from diesel engines. Mixing combustion aerosols with atmospherically relevant constituents will allow us to observe the water uptake properties at different supersaturations.

2.3.2 **Internal Aerosol Mixtures: Succinic Acid and Sodium Chloride**

Internal mixtures of aerosol can be formed by mixing compounds in solution (e.g., but not limited, Gibson et al., 2007; Hameri et al., 2002). Internal solutions of a highly soluble compound, NaCl, and a slightly soluble compound, succinic acid, are selected. Five aqueous solutions of succinic acid and NaCl with molar ratios of 100:0, 87:13, 69:31, 43:57, 0:100 were aerosolized using a single atomizer, dried, and sample directly into a Scanning Mobility Particle Sizer (SMPS) and CCN Counter (CCNC). Details of the instruments are described in Section 4.4.

2.3.3 External Aerosol Mixtures: Mixing Apparatus: Flow Tube

To characterize and modify mixing states, a laminar flow tube mixing apparatus was constructed to control and modify the extent of mixing of multiple components (Fig. 1 & 2). The first aerosol stream is introduced into the flow tube by a ¼" stainless steel (SS) tube. The second aerosol stream is also introduced by a ¼" SS tube, but is expanded to an outer concentric ¾" SS tube using a SS Swagelok tee connection. The two aerosol flows are initially mixed together at the exit of ¼" tube and mixes within the ¾" SS tube for an additional 12" before it enters the quartz tube where it continues to mix. By repositioning the inlet system or modifying the flow rate in the tube, the residence time can be modified to achieve the desired mixing state fraction. Pressure and temperature of the flow tube is maintained at ambient conditions.

The extent of mixing in the laminar flow tube mixer has been modeled by Computational Fluid Dynamics simulation (CFD - Comsol) to test and improve the aerosol mixing capabilities of the laminar flow tube mixer (Fig. 2-1). CFD modeling optimized dimensions to increase the flow velocities and thus the local Reynolds numbers to maximize the mixing behaviors of the two concentric flow streams introduced by the adjustable inlet system. Particle losses do occur within the laminar flow tube system but do not affect the intrinsic aerosol properties presented here.

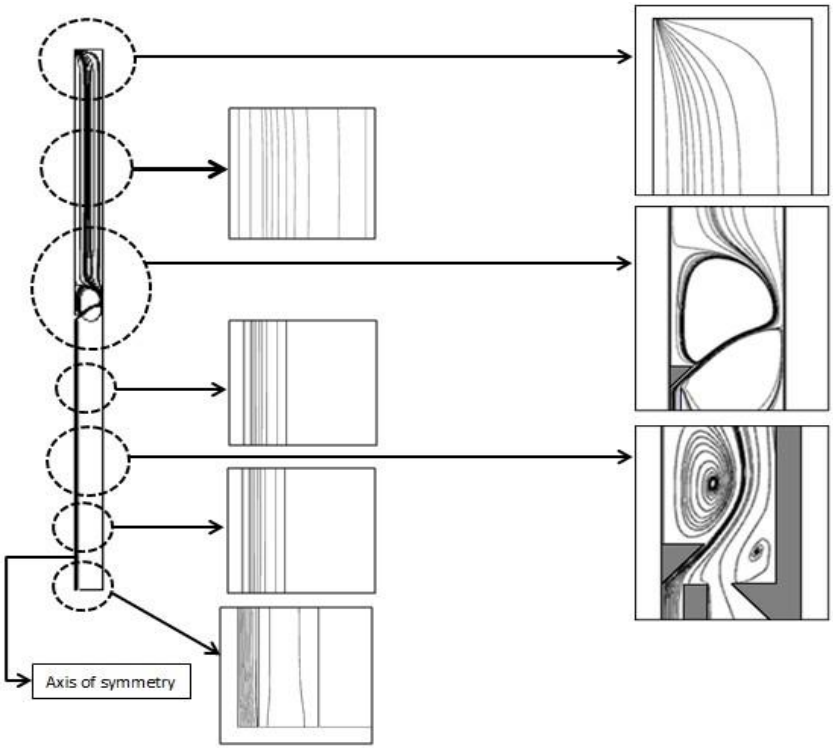

Figure 2-1. Fluid dynamics simulation results of the flow stream transporting behaviors in the laminar flow tube mixer

2.3.4 Modified Mixing States: External to Internal

Individual single component aqueous solutions of ammonium sulfate (AS), $(NH_4)_2SO_4$, and succinic acid (SA) were aerosolized, dried with a heater and a silica gel diffusion column, and individually introduced to the flow tube through two injection ports to obtain activation data under externally mixed conditions (Fig. 2). Combustion aerosol was introduced to the flow tube using the APG.

To induce internal mixing, aerosol water was introduced to the aerosol stream for the atomized aerosol sources. The wetted aerosols can come in contact through diffusion and coalesce to form an internally mixed aerosol. This was accomplished by removing the heating source for the driers and only partially drying the atomized aerosols with the silica gel columns. Flow tube experiments with AS/SA and combustion aerosol/SA were each completed under both external and internal mixing conditions.

2.3.5 CCN Activity and Chemical Composition Measurement

CCN activation is measured with particle sizing and counting instrumentation in parallel with CCN counting instrumentation. This technique is standard and has been used in numerous publications (e.g., but not limited to, Padro et al., 2012; Moore et al., 2010). The development of a single continuous-flow thermal gradient diffusion column CCN Counter, CCNC (Droplet Measurement Technologies, Inc.) has provided rapid (~1 Hz) and robust CCN data (Lance et al. 2006, Roberts and Nenes 2010). Aerosols with a S_c lower

than the supersaturation in the column activate and form droplets. These droplets are detected and counted using an optical particle counter at the exit of the column.

A TSI 3080 Electrostatic Classifier selects and measures aerosol size distributions. Polydisperse aerosol streams are passed through a bi-polar krypton-85 charger and then through a differential mobility analyzer, DMA where the aerosols are sized according to electrical mobility with a sheath to aerosol flow ratio of 10:1. The monodispersed flow is then split to a CPC and a CCN counter to obtain the CCN/CN. The CN concentrations were obtain using a condensation particle counter, CPC (TSI 3772, TSI 3776).

The CCNC is operated at 0.5 lpm with a sheath to aerosol flow ratio of 10:1 and is calibrated with $(NH_4)_2SO_4$ to determine the column supersaturation (Rose et al. 2008). Operating the CCN in parallel with the CPC allows for the simultaneous measurements of the total CN and CCN of the monodispersed aerosols. By operating the DMA in scanning voltage mode and maintaining a constant column supersaturation, the CCN/CN, or activation ratio, as a function of dry diameter can be obtained for a given supersaturation. These size resolved CCN distributions obtained through scanning mobility CCN analysis (SMCA) are used to obtain an activation curve (Moore et al. 2010).

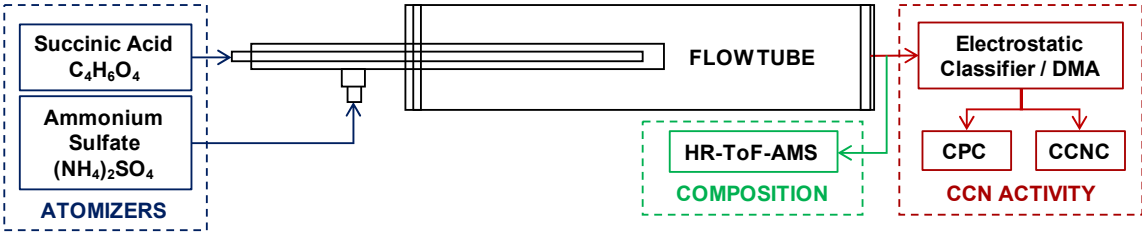

Figure 2-2. External and Internal Mixtures with gradual mixing in flow tube

An Aerodyne high-resolution time-of-flight aerosol mass spectrometer (HR-ToF-AMS) measured the nonrefractory bulk composition (DeCarlo et al., 2006). The HR-ToF-AMS was operated in V-mode to track the concentration and vacuum aerodynamic diameter as the aerosol fractions were modified.

2.4 Analysis of CCN Activation Data

CCN data analysis of single component aerosols, such as AS, are well understood. The activation of a single known component, such as AS yields a simple sigmoidal activation curve (Fig. 3a). However ambient aerosols generally exist as complex heterogeneous mixtures of organic and inorganic species. CCN data sets from ambient and chamber studies, which consist of these aerosol mixtures, may not show a single clean activation curve but instead can exhibit multiple activation curves not associated with doubly charged particles (Fig. 3b).

SMCA was used to determine the CCN/CN as a function of dry activation diameters for the multicomponent aerosols, and thus, distinguish multiple activation curves. Externally mixed aerosol fractions in activation curves have been previously observed in ambient studies by Lance et al. (2013), Moore et al. (2012), and Bougiatioti et al., (2011). For those studies, E was defined as the soluble fraction, and 1-E the insoluble mixed fraction. For this study the first curve is defined as the soluble externally mixed fraction (EMF) with an asymptote, or plateau of η.

The supersaturation and critical dry diameter are related through $\boldsymbol{\kappa}$ (eqn 2) to describe the CCN activity and to determine the effect of mixing states of multiple components on

the supersaturated hygroscopic properties of aerosols. A sigmoidal fit through the EMF is completed to determine the particle dry diameter of the more hygroscopic species. A second sigmoidal fit is completed for the second activation curve. An example is shown in fig. 2-3 for an external mixture of AS and SA. A sigmoid is fit for the more hygroscopic species, AS, and then a second for the less hygroscopic species, SA. The activation diameters are consistent with those expected for the two heterogenous compounds and agree with Kohler predicted activation values for AS and SA. Doubly charge aerosols are indicated in fig. 2-3 a and b and are a minimal contrubtion to the activation curves.

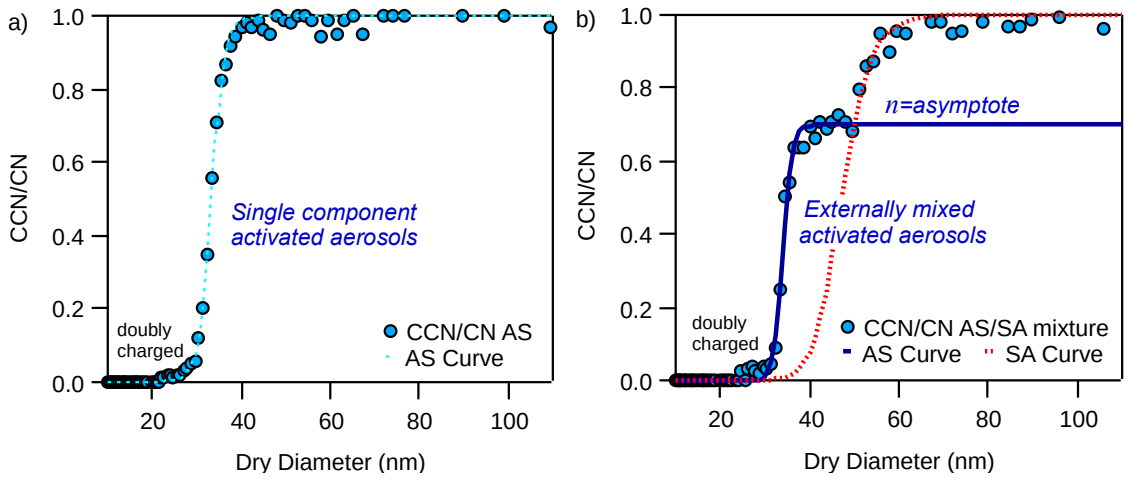

Figure 2-3. Example of charge corrected a) a single component activation curve b) a multiple activation curve from an externally mixed system.

To track the change in organic/inorganic fractions, the mixed aerosols were analyzed with a high-resolution time of flight mass spectrometer (HR-Tof-AMS) to provide the mass fraction. The mass size distribution was integrated and normalized for each compound per scan according to the total mass that was measured. The mass size distribution was then converted to number size distribution. The diameters were converted from aerodynamic diameter to electrical mobility diameter using a density of 1.56 g cm^{-3} and 1.77 g cm^{-3} for

succinic acid and ammonium sulfate, respectively. The aerosols are assumed to be spherical. Then for each superstation and fraction, the EMF was calculated between the two respective activation diameters and correlated to the EMF that was determined from SMCA to determine the plateau height (η).

2.5 Results and Discussion

2.5.1 Internal Mixtures

Aerosolized internal mixed solutions exhibit single CCN activation curves for all five solutions of succinic acid and NaCl solutions (Fig 2-4). As the internal mixture salt fraction increased at a given supersaturation, the single curve was maintained and shifted towards a lower activation diameter, which is indicative of and consistent with more hygroscopic aerosol. Using the simple mixing rule, a multicomponent hygrosocopicity parameter can be theoretically derived based on the expected kappa values for each individual component hygrosocopicity ($\boldsymbol{\kappa_i}$), and the volume fraction of each component (ε_i) (Petters and Kredenweis, 2007).

$$\boldsymbol{\kappa} = \sum_{\boldsymbol{i}} \boldsymbol{\varepsilon_i \kappa_i} \qquad (\mathbf{3})$$

Eqn 3 was applied for each mixture to determine $\boldsymbol{\kappa}$ and compared to the experimental values (Figure 5). These internal mixtures do not strongly follow the simple mixing rule for every mixture. Shulman et al. (1996) showed that for slightly soluble compounds internally mixed with salts resulted in surface tension depression and thus a lower required

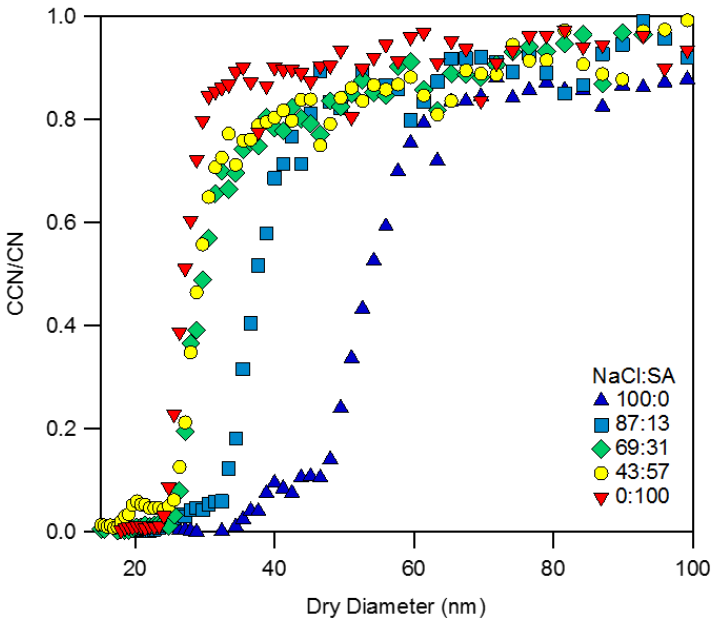

Figure 2-4. Activation curves for two component internal mixtures of NaCl and succinic acid (SA) at SS 0.72%. Doubly charged aerosols are present but are all below 0.1.

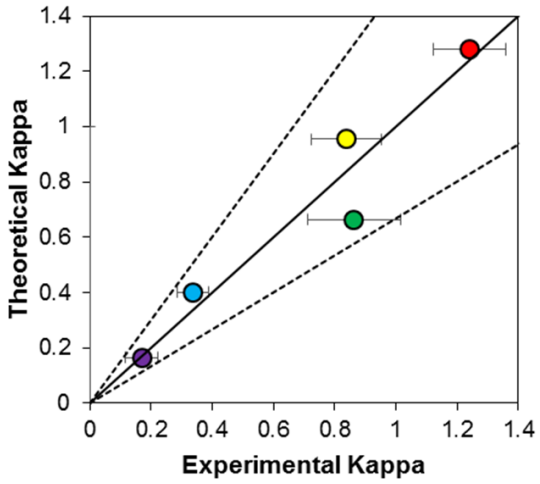

Figure 2-5. Internally mixed aerosols. Multicomponent hygrosocopicity parameter predictions vs experimentally derived kappa values

critical supersaturation. Accounting for surface tension depressions could improve hygroscopcity improvements for internal mixtures.

2.5.2 Externally Mixed Hygroscopic fraction, η

Data sets yielding multiple activation curves were successfully created by mixing compounds of varying hygroscopicity in the flow tube. A slightly soluble organic aerosol, SA, and a soluble inorganic salt aerosol, AS, were selected. To determine the concentration dependence of the EMF plateau and to modify the activation curves, the inorganic fraction was modified by gradually increasing the concentration of ammonium sulfate in the flow tube followed by the introduction of water. The CCNC was operated at a single Sc of 0.8%.

The apparent kappa values from fitting the two individual activation curves for the external part of the mixing experiment and subsequent internal mixing are shown in figure 6a. Clear and separate curves are observed until internal mixing conditions; at this point the separate curves converge into a single one (figure 6b). The data agreed well with Köhler Theory and single parameter (κ) thermodynamic predictions of droplet activation. The activation curves were characteristic of AS, and SA; the activation diameters agreed with theory. It is expected that as the particles become more mixed over time, and move from an externally mixed state to an internally mixed state that their hygroscopicity would be modified. Under dry conditions, the aerosols maintained an external mixture and multiple activation curves were observed to be constant.

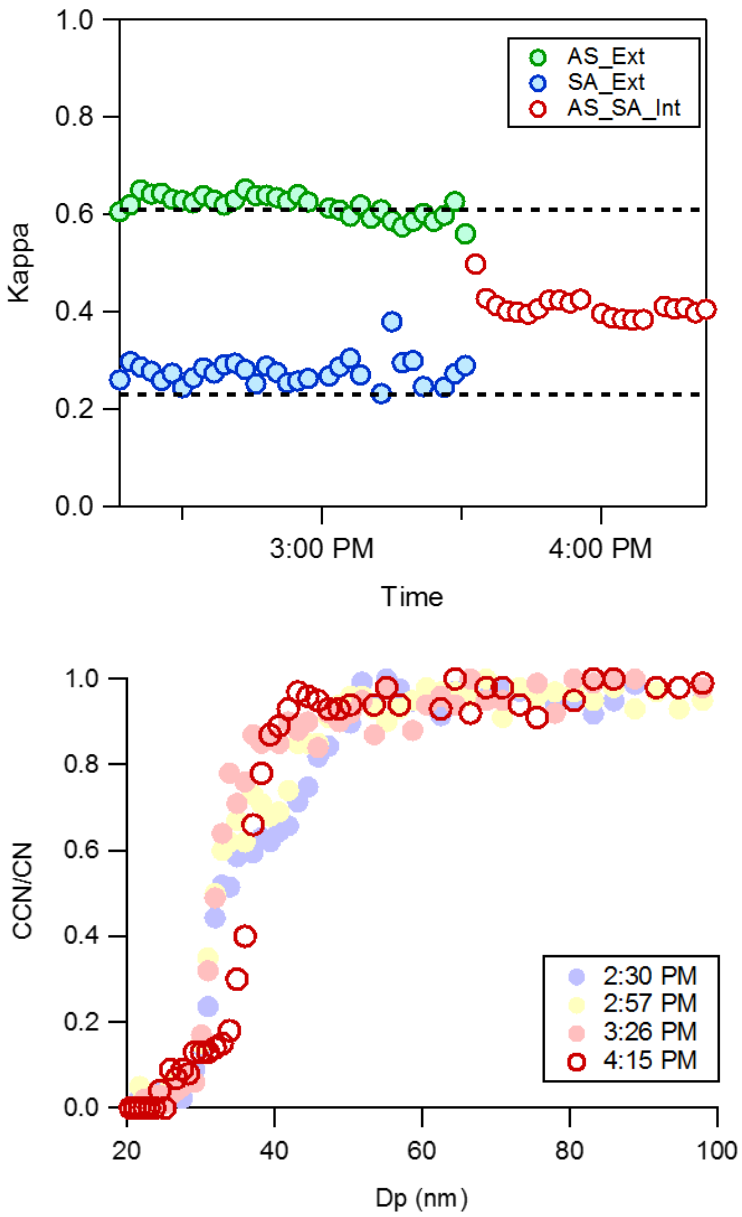

Figure 2-6. a) apparent kappa values for the external part of the mixing experiment until 3:45 pm where internal mixing conditions were introduced. The two dotted lines indicate the theoretically derived kappa values for succinic acid, κ=0.231, and ammonium sulfate, κ=0.61. B) activation curves, under external and then mixing conditions

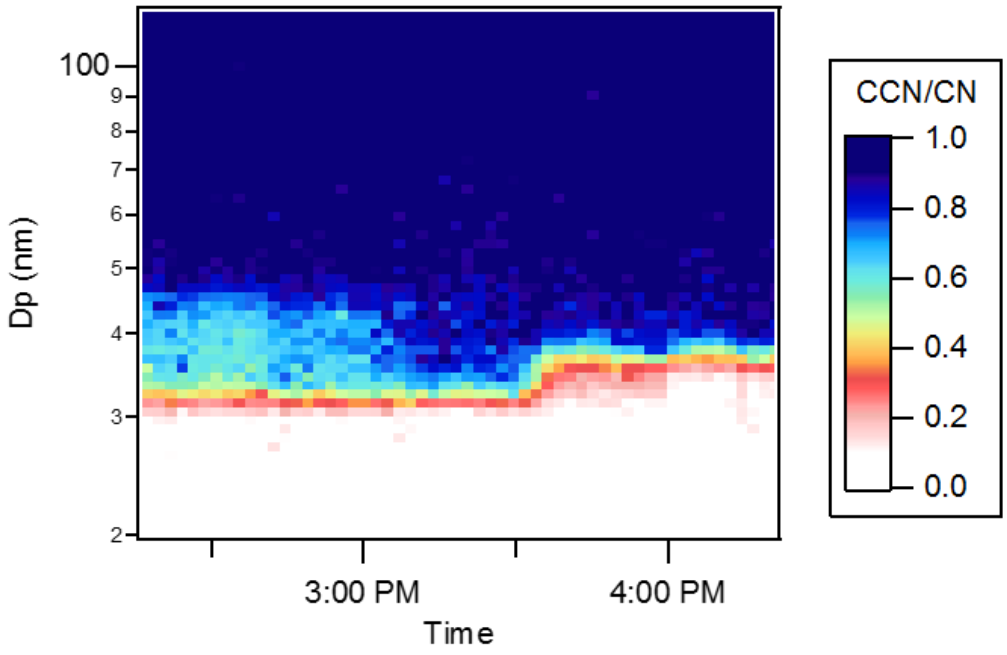

Figure 2-7. CCN/CN vs. Dry diameter data as a function of time.

Under humid conditions, external mixing was initially observed; however, the aerosol water promoted internal mixing and the activation curves were observed to converge into a single curve and that their hygroscopicity would be modified. Results suggest aerosol water as a significant factor in mixing. This behavior has been observed in other studies where water was shown to lower the viscosity of particles, thus increasing their diffusivity (Ye et al, 2016).

The increase in AS is consistent with the increase in the plateau heights derived from SMCA. However, the AS fraction according to the AMS data are slightly lower for the higher concentration. A second flow tube experiment was conducted to test the lower concentrations to see if they would yield lower plateau heights. The detection efficiency for the lower sizes in the AMS (<50nm) can effect the AS fraction detected by the AMS.

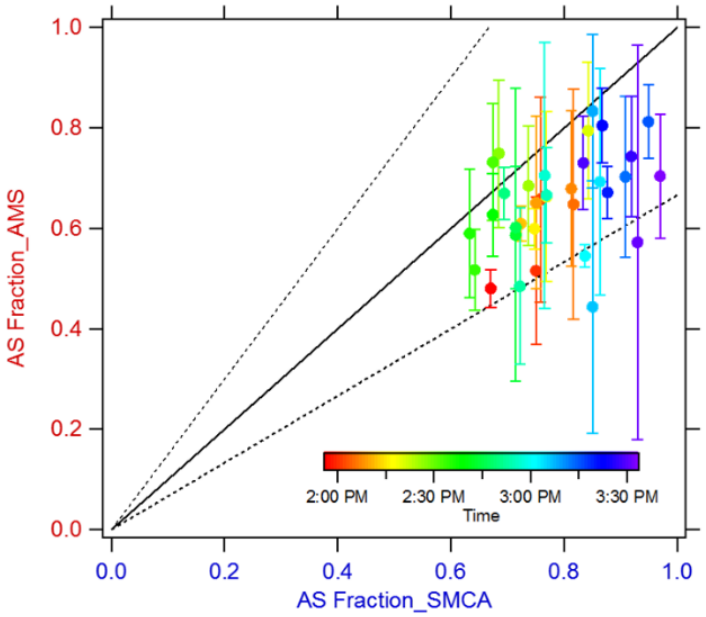

Figure 2-8. Plateau heights derived from AMS data vs. SMCA

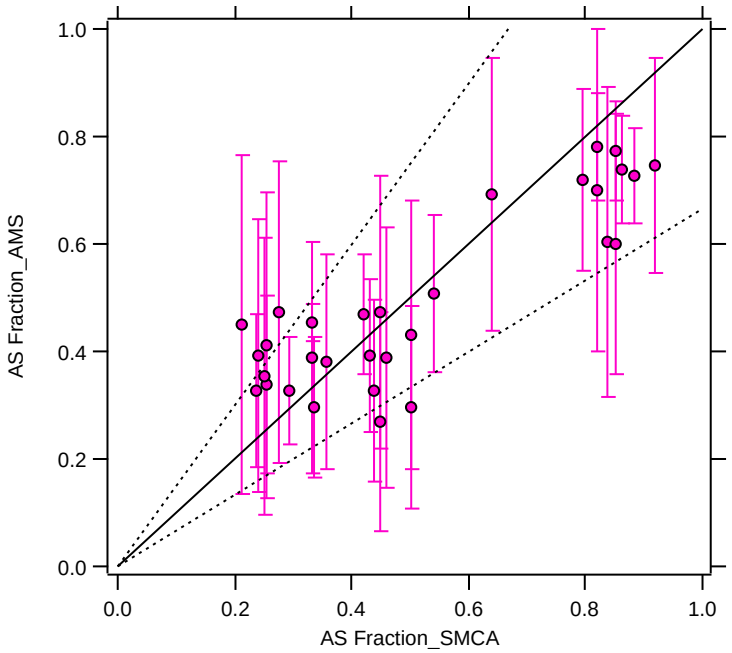

Figure 2-9. Plateau heights derived from AMS data vs. SMCA.

Thus, the CCNC supersaturation was modified from 0.2 to 1.2% as well to test the effect of activation diameter on closure. Results show good agreement.

2.5.3 Combustion aerosol

To investigate the impact of mixing fresh combustion emissions with organic aerosols on CCN spectra, the CCN activation spectra of combustion was first defined using combustion aerosol derived from the APG and is presented in Figure (2-10). BC activated at a diameter of 132.5nm with a high supersaturation of 2.2%; and the apparent hygrosocopicity of combustion aerosol was measured at κ=0.001, which is consistent with kappa values reported for fresh combustion aerosol in chapters 3 and 4.

Next, to investigate the influence of modifying externally mixed hygroscopic aerosol fractions with non-hygroscopic BC, the combustion aerosol was externally mixed with various concentrations of AS and NaCl in two separate experiments. These experiments were completed at a supersaturation of 1.1%. At this supersaturation, the combustion aerosol is not expected to activate, so the activated fractions should be reflected with the plateau heights.

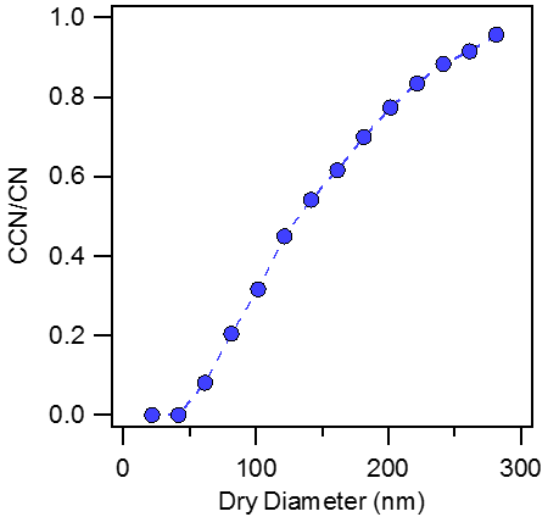

Figure 2-10. Combustion aerosol activation curve (SS 2.2%, $D_{p,50}$ 132.5, $\boldsymbol{\kappa}$=0.001)

For each mixture, the combustion aerosol was first introduced to the flow tube, and then followed by the inorganic; the concentration of inorganic in the flow tube was then slowly increased. The initial combustion size distribution at the start of the experiment and the modified CCN activation fractions of the aerosol mixtures are presented in Figure 2-11a and b. For both the AS and NaCl, the activation points were consistent with the expected activation diameters of the respective inorganic salts. However, at the larger sizes where the combustion concentration increases, the activation curves were depressed beyond the critical activation point of the inorganic salts. This is because the combustion aerosol is not CCN active at this S_c or size and the depressions is reflective of the non hygroscopic combustion aerosol fraction in the aerosol sample. As the concentration of inorganic salts increase, the increased activated fraction is reflected in the CCN spectra where the plateau heights are observed to increase with increasing soluble concentrations.

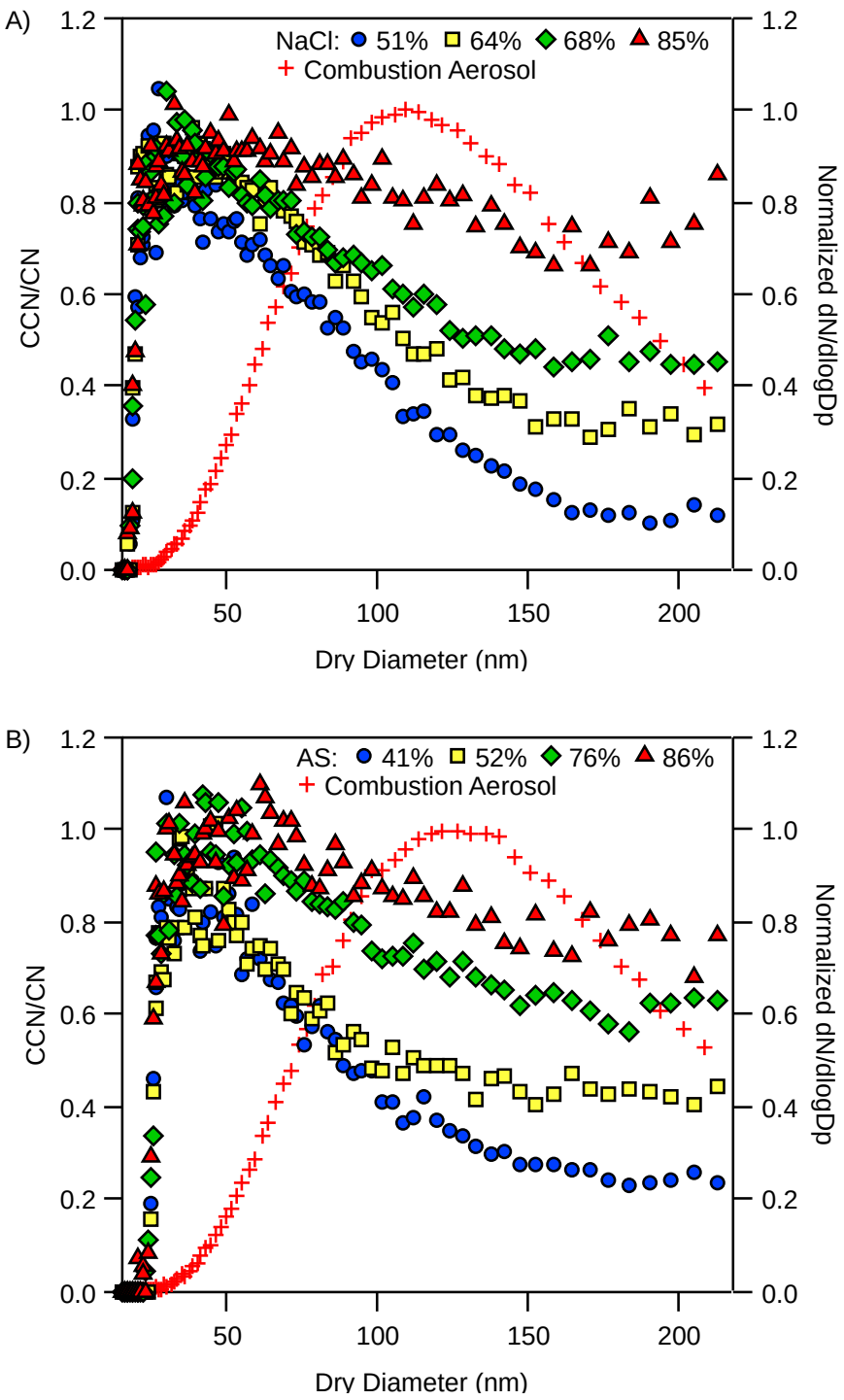

Figure 2-11. Combustion aerosols externally mixed with inorganics a) NaCl externally mixed with concentrations modified from 51% to 85% over the course of 60 min b) AS externally mixed with concentrations from 41% to 86% over a course of 75 min. Red crosses represent the initial size distribution of the combustion aerosol.

To investigate the effect of internally mixing slightly soluble organic with non-activated insoluble aerosols (e.g. increased in SOA mass fractions from the condensation of SOA on combustion aerosols during atmospheric aging), succinic acid (SA) was mixed with combustion aerosol. The SA was introduced to the flow tube at various concentrations, followed by the combustion aerosol from the APG, under dry externally mixed conditions, bimodal peaks were obtained (figure 2-12).

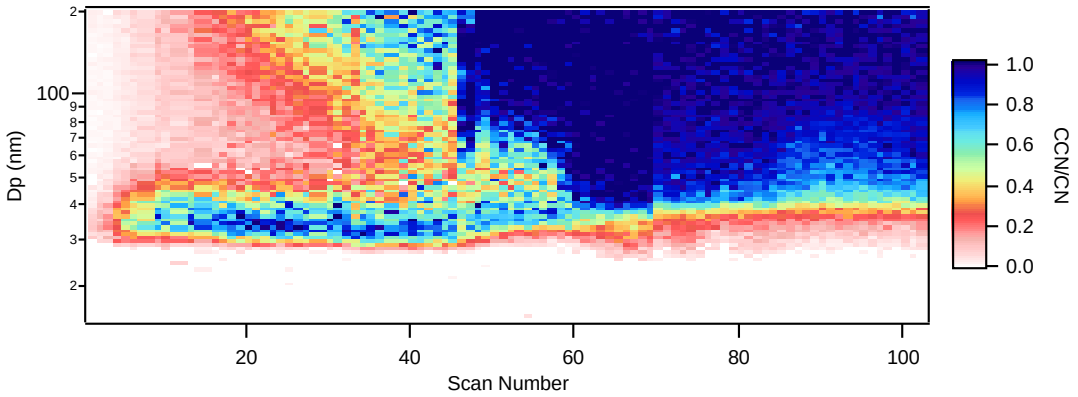

Figure 2-12. Time series SA and combustion aerosol mixture in flow tube

Assuming the first of the two peaks is the SA, and the second is a mixture of the combustion aerosol and SA, the initial point of activation agrees with that of succinic acid where SA aerosols all activate beyond the activation point. At the point where the concentration of combustion aerosol begins to increase, the CCN/CN is initially lowered to reflect the lower concentration of the activated SA relative to the non-activated BC concetration. However, the CCN/CN begins increasing again. This indicates that there may be some internal mixing occurring through coagulation or that internal mixing may be occurring in the activation column of the CCNC as aerosol wetting was not initiated until scan 70.

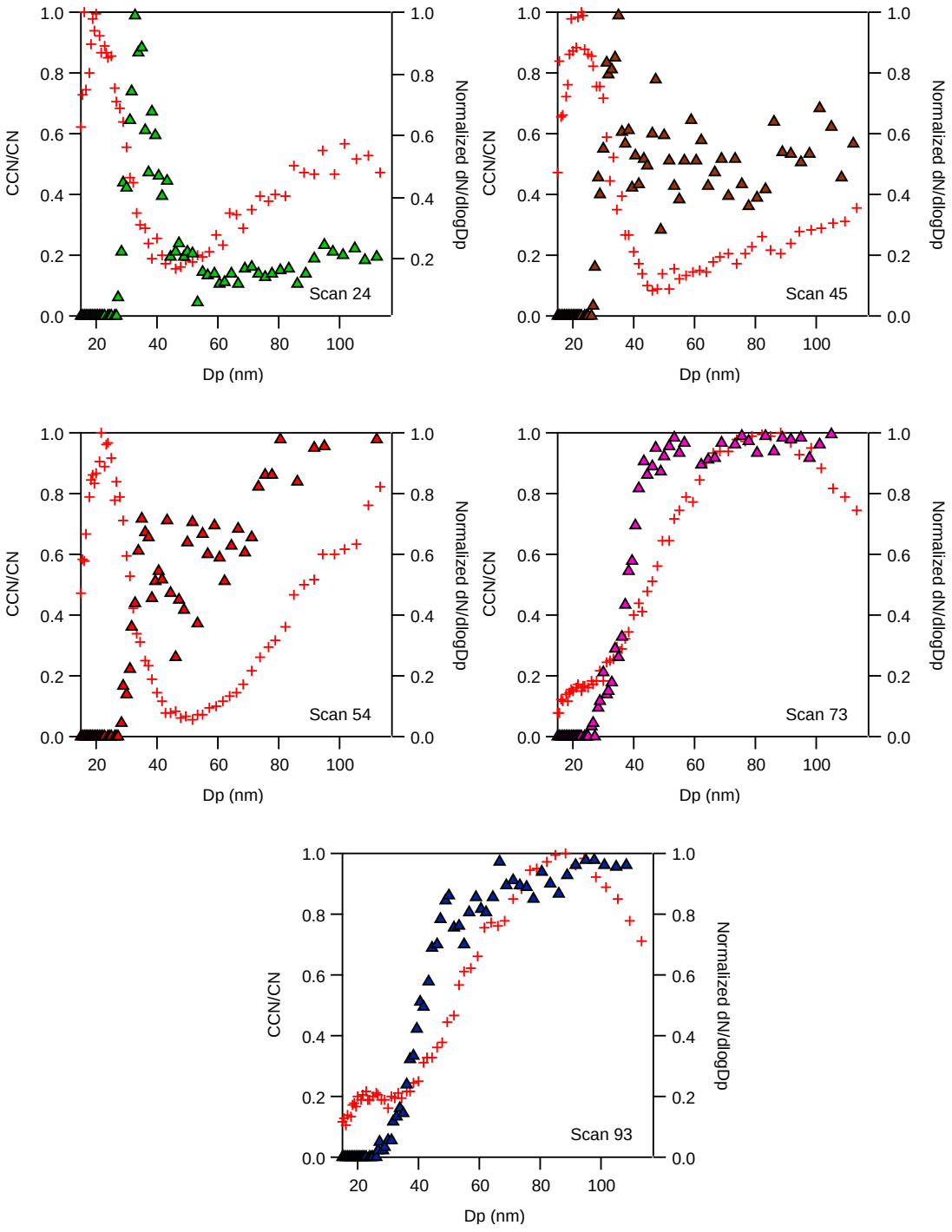

Figure 2-13. Succinic Acid and Combustion Aerosol mixtures for Scans 24, 45, 54, 73, and 98. Aerosol water is introduced at ~ scan 70 to promote internal mixing.

However, when water was introduced, internal mixing was observed to strongly influence the mixing state, where the multiple activation curves converge into a single one. This is consistent with previous work (e.g., but not limited to Cruz and Pandis, 1998) that has observed a strong influence in the activation of insoluble compounds when internally mixed with a more soluble compound. But with continued mixing, it becomes apparent that there is still some degree of external mixing towards the end (scan 93) where there is a slight depression in the plateau of the CCN spectra. In addition, there a shift towards a larger activation diameter as well.

2.6 Conclusion

Results indicate that the activation curve of aerosol sample provides insight as to the type of mixing (e.g. internal vs. external) and the various levels of hygrosopicities that are chemically representative. Modifications in the concentrations of externally mixed non-hygroscopic aerosols are reflective of the CCN activated concentrations. This is consistent with CCN spectra observed in ambient studies, which have attributed increases in plateau height to the level of internal mixing of soluble materials on externally-mixed unactivated aerosols. As the non-hygroscopic combustion aerosol becomes coated or internally mixed with the organic material, the CCN activity of the combustion aerosol is modified. Data also confirms that aerosol water is a significant factor in promoting phase mixing and can be used to control mixing states. Under dry conditions, the aerosols maintained an external mixture under dry conditions, activation curves remained separate and constant. However, humid conditions promoted internal mixing and the activation curves were observed to

converge. Preliminary results suggest that the aerosol morphology can be observed in CCN activation data and can be revisited in complex aerosol data sets to understand the extent of mixing.

2.7 Acknowledgements

This work was supported by the University of California Transportation Center and the U.S. Environmental Protection Agency (EPA) grant number 83504001. Diep Vu thanks the U.S. Environmental Protection Agency (EPA) STAR Fellowship Assistance Agreement no. FP-91751101. The contents of this paper are solely the responsibility of the grantee and do not necessarily represent the official views of the EPA. Further, the EPA does not endorse the purchase of any commercial products or services mentioned in the publication.

2.8 References

Abbatt, J. P. D., Broekhuizen, K., and Kumar, P. P. (2005). Cloud condensation nucleus activity of internally mixed ammonium sulfate/organic acid aerosol particles, Atmospheric Environment, 39, 4767-4778.

Asa-Awuku, A., Miracolo, M. A., Kroll, J. H., Robinson, A. L., and Donahue, N. M. (2009). Mixing and phase partitioning of primary and secondary organic aerosols, Geophys. Res. Lett., 36, L15827, doi:10.1029/2009GL039301.

Bilde, M. and Svenningsson, B. (2004). CCN activation of slightly soluble organics: The importance of small amounts of inorganic salt and particle phase, Tellus, 56B, 128–134.

Bougiatioti, A., Nenes, A., Fountoukis, C., Kalivitis, N., Pandis, S. N., and Mihalopoulos, N. (2011). Size-resolved CCN distributions and activation kinetics of aged continental and marine aerosol, Atmos. Chem. Phys., 11, 8791-8808, doi:10.5194/acp-11-8791-2011.

Broekhuizen, K., Kumar, P. P., and Abbatt, J. P. D. (2004). Partially soluble organics as cloud condensation nuclei: Role of trace soluble and surface active species, Geophys. Res. Lett., 31, D01107, doi:10.1029/2003GL018203.

Chan, M. N., Kreidenweis, S. M., and Chan, C. K. (2008). Measurements of the hygroscopic and deliquescence properties of organic compounds of different solubilities in water and their relationship with cloud condensation nuclei activities, Environ. Sci. Technol., 42, 3602–3608.

Cruz, C. N. and Pandis, S. N. (1998). The effect of organic coatings on the cloud condensation nuclei activation of inorganic atmospheric aerosol, J. of Geo. Res., 103(D11), 13111-13123.

Ervens, B., Cubison, M., Andrews, E., Feingold, G., Ogren, J. A., Jimenez, J. L., DeCarlo, P., and Nenes, A. (2007). Prediction of cloud condensation nucleus number concentration using measurements of aerosol size distributions and composition and light scattering enhancement due to humidity, J. Geophys. Res., 112, D10S32, doi:10.1029/2006JD007426.

Gibson, E. R., Gierlus, K. M., Hudson, P. K., and Grassian, V. H. (2007). Generation of Internally Mixed Insoluble and Soluble Aerosol Particles to Investigate the Impact of Atmospheric Aging and Heterogeneous Processing on the CCN Activity of Mineral Dust Aerosol, Aer. Sci. and Tech., 41, 914-924, doi: 10.1080/02786820701557222.

Hameri , K. , Charlson , R. and Hansson , H. C. (2002). Hygroscopic Properties of Mixed Ammonium Sulfate and Carboxylic Acids Particles. AIChE J., 48, 1309–1316.

Henning, S., Rosenørn, T., D'Anna, B., Gola, A. A., Svenningsson, B., and Bilde, M. (2005). Cloud droplet activation and surface tension of mixtures of slightly soluble organics and inorganic salt, Atmos. Chem. Phys., 5, 575-582, doi:10.5194/acp-5-575-2005.

Kreidenweis, S. M., Petters, M. D. and DeMott, P.J. (2006). Deliquescence-controlled activation of organic aerosols, Geophys. Res. Lett., 33, L06801, doi:10.1029/2005GL024863.

Lance, S., Raatikainen, T., Onasch, T., Worsnop, D. R., Yu, X.Y., Alexander, M. L., Stolzenburg, M. R., McMurry, P. H., Smith, J. N., and Nenes, A. (2012). Aerosol mixing-state, hygroscopic growth and cloud activation efficiency during MIRAGE 2006, Atmos. Chem. Phys. Discuss., 12, 15709–15742, doi:10.5194/acpd-12-15709-2012.

Lance, S., Onasch, T., Warsnop, D., Yu, X. Y., Alexander, L., Stolzenberg, M., McMurry, P., Smith, J.N., Nenes., A. (2013). Aerosol Mixing-State and Cloud Activation Efficiency during the MILAGRO Campaign, Atmos. Chem. Phys., 13, 5049-5062, doi:10.5194/acp-13-5049-2013.

Liu, D., Allan, J., Whitehead, J., Young, D., Flynn, M., Coe, H., McFiggans, G., Fleming, Z. L., and Bandy, B. (2013). Ambient black carbon particle hygroscopic properties controlled by mixing state and composition, Atmos. Chem. Phys., 13, 2015-2029, doi:10.5194/acp-13-2015-2013.

Moore, . H., Nenes., A. and Medina., J. (2010). Scanning Mobility CCN Analysis - A Method for Fast Measurements of Size-Resolved CCN Distributions and Activation Kinetics, Aerosol Science and Technology, 44, 861-871.

Moore, R. H., Cerully, K., Bahreini, R., Brock, C. A., Middlebrook, A. M. and Nenes, A. (2012). Hygroscopicity and composition of California CCN during summer 2010, J. Geophys. Res., 117, D00V12, doi:10.1029/2011JD017352.

Padró, L. T., Asa-Awuku, A., Morrison, R., and Nenes, A. (2007). Inferring thermodynamic properties from CCN activation experiments: single-component and binary aerosols, Atmos. Chem. Phys., 7, 5263-5274, doi:10.5194/acp-7-5263-2007.

Padró, L. T., Moore, R. H., Zhang, X., Rastogi, N., Weber, R. J., and Nenes, A. (2012). Mixing state and compositional effects on CCN activity and droplet growth kinetics of size-resolved CCN in an urban environment, Atmos. Chem. Phys., 12, 10239-10255, doi:10.5194/acp-12-10239-2012.

Petters, M. D. and Kreidenweis, S. M. (2007). A single parameter representation of hygroscopic growth and cloud condensation nucleus activity, Atmos. Chem. Phys., 7, 1961-1971, doi:10.5194/acp-7-1961-2007.

Petters, M. D. and Kreidenweis, S. M. (2008). A single parameter representation of hygroscopic growth and cloud condensation nucleus activity – Part 2: Including solubility, Atmos. Chem. Phys., 8, 6273-6279, doi:10.5194/acp-8-6273-2008.

Shulman, M. L., Jacobson, M. C., Charlson, R. J., Synovec, R. E., and Young, T. E. (1996). Dissolution behavior and surface tension effects of organic compounds in nucleating cloud droplets, Geophys. Res. Lett., 23, 277–280.

Sullivan R. C., Moore M., Petters, M. D., Kreidenweis S. M., Roberts G. C., and Prather, K. A. (2009). Effect of chemical mixing state on the hygroscopicty and cloud nucleating properties of calcium mineral dust particles, Atmos. Chem. Phys., 9, 3303-3316.

Svenningsson, B., Rissler, J., Swietlicki, E., Mircea, M., Bilde, M., Facchini, M. C., Decesari, S., Fuzzi, S., Zhou, J., Mønster, J., and Rosenørn, T. (2006). Hygroscopic growth and critical supersaturations for mixed aerosol particles of inorganic and organic compounds of atmospheric relevance, Atmos. Chem. Phys., 6, 1937-1952, doi:10.5194/acp-6-1937-2006.

Wex, H., McFiggans, G., Henning, S., and Stratmann, F. (2010). Influence of the external mixing state of atmospheric aerosol on derived CCN number concentrations, Geophys. Res. Lett., 37, L10805, doi:10.1029/2010GL043337.

Ye, Q., Robinson, E. S., Ding, X., Ye, P., Sullivan, R., and Robinson, N. (2016). Secondary organic aerosols are crunchy when dry but runny when wet: direct observation of semi-volatile organic materials mixing within atmospherically-relevant secondary organic aerosols. Submitted to Proceedings of the National Academy of Science.

Chapter 3 - Integrating Cloud Condensation Nuclei Predictions with Fast Time Resolved Aerosol Instrumentation to Determine the Hygroscopic Properties of Emissions over Transient Drive Cycles

3.1 Introduction

Aerosols that activate to form cloud droplets when exposed to a supersaturated environment greater than its characteristic critical supersaturation, SS, are Cloud Condensation Nuclei (CCN). This SS is highly dependent on curvature (Kelvin effect) and solute (Raoult effect) properties of the aerosol (Köhler, 1936, Dusek et al., 2006). By acting as CCN, aerosols can modify the microphysical properties of clouds by forming droplets that either scatter solar radiation back into space or allow energy to pass through and reach the surface of the earth, thereby indirectly influencing the radiative balance of the environment (Twomey, 1974). Unfortunately, these aerosol-cloud interactions and their relationship with climate are not well defined and is currently a large contributor to the uncertainty in radiative forcing estimates (IPCC, 2013).

Primary combustion aerosols (biomass burning, fossil fuels, and biofuels) can contribute to the CCN budget by directly increasing the particle number concentrations in the atmosphere. If they contain a fraction of soluble material at a large enough size, they may potentially be CCN active. In addition, they can serve as seeds for more soluble material to condense onto and become CCN active (Andreae and Rosenfeld, 2008 and references therein). Carbonaceous combustion aerosols are estimated to account for approximately 52-64% of the global CCN budget, with a global mean aerosol indirect effect of -0.34 W m^{-2}. Aerosols derived from fossil fuels and biofuels are predicted to have the strongest cooling effect; they make up only one third of the mass from all aerosols

derived from combustion fuels but account for -0.23 W m^{-2} or two thirds of the overall forcing (Spracklen et al., 2011). These carbonaceous aerosols may play an important role in the CCN budget.

Vehicle emissions are a significant source of primary carbonaceous combustion aerosols in urban atmospheres (Rose et al., 2006). Fresh vehicle emissions have been classified with low CCN activity (Tritscher et al., 2011), which may be attributed to *i)* insoluble materials present in the aerosols, *ii)* an externally mixed state where the condensation of soluble material is less probable, or *iii)* small sizes where a large fraction of these aerosols are emitted in the nucleation mode directly off the tailpipe (Andreae and Rosenfeld, 2008 and references therein; Karjalainen et al., 2014). Insoluble materials in fresh vehicle emissions, predominately soot, have been characterized with low hygroscopic growth (Dua et al., 1999; Weingartner et al., 1997). Furthermore, freshly emitted soot is typically in an externally mixed state, so the condensation of soluble materials has not occurred and the soot maintains low hygroscopicity (Hasegawa and Ohta, 2002; Rose et al., 2011). However, recent work indicates the addition of oxygenated biofuels could modify the hygroscopic properties of diesel emissions (Happonen et al., 2013) and gasoline emissions (Short et al., 2015); the latter of which exhibited potentially high CCN activity. In addition, lower elemental carbon (EC)/organic carbon (OC) fractions have been shown to correlate with higher water soluble organic carbon (WSOC) fractions for vehicles operating with biodiesel than when operating with diesel (Cheung et al., 2009). The lower soot formation was attributed to the higher oxygen content of the biofuels, which increased oxidation and inhibited carbon chain formation. The higher oxygen content present in the

higher biofuel concentration blends may lead to an increase in the WSOC to OC ratios, thereby modifying the hygroscopicty of the emissions.

One of the most widely used biofuels in the United States is ethanol, which is commonly blended at 10% ethanol and 90% gasoline (E10). However, with the Renewable Fuel Standard (RFS2) requiring 36 billion gallons of renewable fuel to be blended into transportation fuel by 2022 (USEPA, 2007) there is now interest in blending higher concentrations of ethanol into gasoline. Another biofuel, iso-butanol, is also gaining popularity due to its favorable properties when compared to gasoline. Compared to ethanol, iso-butanol is less corrosive, has a higher energy content, lower volatility, and higher tolerance to water contamination (Morela et al., 2012). The aerosol composition, size, and mixing state, which can impact the hygroscopicity of the aerosols, is dependent of the vehicle technology, fuel source, and driving conditions. With biofuel use expected to grow, it is important to understand the effect of biofuels and increasing oxygenated fuel content on the hygroscopic properties of vehicle emissions. However research related to the hygroscopicity of emissions derived from the use of different ethanol and iso-butanol blends is limited, especially when utilized in vehicles with modern engine technologies (Short et al., 2015).

For emissions sources, composition is highly dependent on the combustion conditions, which means CCN activation can vary substantially with time (Yao et al., 2006). Number concentrations can change on a second-by-second basis (e.g., but not limited to, particle number concentration time traces available in Karavalakis et al., 2014). Consequently, Scanning Mobility CCN Analysis (SMCA) (Moore et al., 2014) requires

scan times to measure relevant particle distributions that may be too long to capture the changes on a second-by-second basis. Scanning electrical mobility measurements have scan times longer than the time in which an instantaneous vehicle acceleration occurs to obtain a full size distribution, and are not ideal for transient testing. To bypass this limitation, CCN predictions using traditional CCN measurements can be integrated with fast (~ 1 Hz) time resolved aerosol sizing instrumentation on a second-by-second basis. With improved scanning speeds, size distributions can be measured at much higher frequencies and used for closure studies (Asa-Awuku et al., 2011). To estimate the CCN potential of aerosols derived from a transient emission source, a method to capture the changing hygroscopicity of emissions from vehicles operating on transient drive cycles is implemented using an Engine Exhaust Particle Sizer, EEPS.

An EEPS is commonly used for measuring emissions from both transient and steady state driving cycles and roadside measurements (Ayala et al., 2005; Wang et al., 2006; Yao et al., 2006; Karavalakis et al., 2015). Although the EEPS has a lower size resolution than the SMPS, it provides a full particle size distribution every second. The application of the EEPS for diesel exhaust has been demonstrated and found to agree with other sizing and particle number concentration measurement instruments (e.g., but not limited to, Johnson et al., 2004; Kittelson et al., 2006; Zervas and Dorlhène 2007). Johnson et al. (2004) measured size distributions using both a Scanning Mobility Particle Sizer (SMPS) and the EEPS for a diesel generator operating on steady state conditions. The size distributions obtained from the two instruments agreed well, with a ±20% deviation from the mean when comparing total counts with a TSI 3022 Condensation Particle Counter

(CPC). This was attributed to the higher sampling efficiency off the EEPS; as the higher sampling speed of the EEPs minimized diffusional losses (EEPS 10 L/min vs SMPS 1.5 L/min) thereby measuring higher particle concentrations below 12 nm. Zervas and Dorlhène (2007) found that particle numbers measured by the EEPS were close to particle numbers measured by a CPC and an Electrical Low Pressure Impactor (ELPI) for a diesel vehicle operating at steady state speeds and the New European Driving Cycle (NEDC). In addition, the engine was equipped with multiple Diesel Particulate Filters (DPF) to test the effect of concentration. Upstream of the DPFs, the instruments measured particle numbers within an order of magnitude of each other. Downstream the DPFs, the EEPS reached its lower detection limit and there was less agreement. However, its particle numbers were still within 1-2 orders of magnitude of those measured by the CPC and ELPI.

This is the first study to integrate fast time resolved aerosol sizing instrumentation, commonly used for vehicle emissions with traditional CCN measurements. It provides a comprehensive evaluation of the method by applying it to three separate aerosol sources; two stable sources and one transient source. The first stable source is ammonium sulfate aerosolized by atomization. However, atomization can result in charge effects (Liu and Deshler, 2003). Therefore, secondary organic aerosol (SOA) formed from α-pinene ozonolysis is selected as the second stable source. After the method is verified on the two well characterized sources, it is then applied to relevant emissions sources to determine the potential for fresh vehicular emissions to activate as CCN from a chassis dynamometer. The vehicular emissions are generated from a spark ignition direct injection (SIDI) vehicle operating on various alcohol blends. The results of this study demonstrates the utility of

the method on multiple aerosol sources and provides information in regards to how ethanol and iso-butanol blends impact the CCN activity of particulate matter (PM) emissions from a modern light-duty gasoline vehicle.

3.2 Theory and Closure Analysis

3.2.1 κ-Köhler Theory

Köhler theory combines thermodynamic and physical properties to predict the activation diameter at which aerosol will undergo spontaneous growth and activate to form a cloud droplet in the atmosphere (Köhler, 1936). Critical activation diameters (D_d) determine the supersaturations required for cloud droplet activation for aerosols of known chemical composition (Seinfeld and Pandis, 1998). Köhler theory can be defined as

$$lnS_c = \left(\frac{4A^3\rho_w M_s}{27v\rho_s M_w D_d^3}\right)^{1/2}, \quad where\ A = \frac{4\sigma_{s/a}M_w}{RT\rho_w} \qquad (1)$$

Where $\sigma_{s/a}$ is the surface tension, M_w is the molecular weight of water, R the universal gas constant, T is the sample temperature, ρ_w is the density of water, D_d is the dry activation diameter, and S_c is the critical saturation, ρ_s is the density of solute, and v is the dissociation factor of solute. It is important to note that the critical saturation, S_c, is greater than 1, thus critical supersaturation is defined by $SS = S_c - 1$.

Köhler theory requires solute information that is not always readily available, especially for complex ambient aerosols of unknown composition. To model the CCN activity of these aerosols, a single hygroscopicity parameter, κ, that represents the compositional information can be integrated with Köhler theory to relate the aerosol dry

diameter and supersaturation (Petters and Kreidenweis, 2007). κ-Köhler theory is defined by

$$\kappa = \frac{4A^3}{27D_d^3 ln^2 S_c} \qquad (2)$$

The surface tension of the solution is assumed to be that of pure water. Aerosol with a κ between 0.5 and 1.4 are highly hygroscopic and exhibit significant CCN activity. Aerosol with hygroscopicity between 0.01 and 0.5 are slightly to very hygroscopic. Kappa values close to zero are considered nonhygroscopic but wettable.

Köhler theory was originally used to describe the CCN activity of simple inorganic salts. However, atmospheric aerosols are typically highly complex mixtures that may contain organic and inorganic components. Modifications have been made to Köhler theory to account for these complex aerosols, and are used to help constrain aerosol cloud interaction models by predicting CCN concentrations. However, solute information is not always readily available, and in these cases, simplifications and chemical assumptions are applied to predict CCN concentrations. Closure is one way of describing the CCN activity of aerosols of unknown chemical properties. By comparing measured CCN number concentrations to CCN concentrations that were predicted based on assumed compositional information, the accuracy of predictions can be evaluated. Closure is achieved if predicted concentrations agree with measured concentrations. Previous studies have implemented closure study methods to obtain CCN activity information with varying levels of success in regions influenced by urban sources (e.g., but not limited to, VanReken et al., 2003; Asa-Awuku et al., 2011; Padró et al., 2012).

3.2.2 Closure Analysis

Traditionally, CCN concentrations are predicted by applying known or assumed chemical composition information and number size distribution data to Köhler theory (Eqn. 1) to determine D_d for various supersaturations ("classical" Köhler theory). Using measured size distributions and the assumption that all aerosols with a diameter above D_d activate, the size bins can be integrated from D_d up to the largest diameter in the size distribution to determine the predicted CCN concentration. If this predicted concentration agrees with measured CCN concentrations, closure is achieved. However, this classical method of closure, C-Closure, can be inefficient for aerosol samples of unknown compositions that are highly variable with time.

The apparent hygroscopicity can be determined on a second-by second basis without the need for compositional information by deriving critical activation diameters by forcing closure. Using the measured size distributions, D_d is determined by integrating the aerosol concentration from the largest size bin in the distribution down to a D_d until the number concentration, which is the calculated CCN concentration, agrees with the measured CCN concentration at a given SS (reverse fit closure, R-closure). This method to determine hygroscopicity has been previously used in closure studies from field and aircraft measurements (e.g., but not limited to Kammermann et al., 2010; Jurányi et al., 2011). With *SS* and D_d, κ is calculated (Eqn. 2) to describe the apparent hygroscopicity of the aerosol sample. Although, exhaust emissions can be fractal and may effect the electrical mobility diameter measurements (Nakao et al., 2011), the particles are assumed to be

spherical. Thus, the apparent hygroscopicity of ephemeral and transient aerosol samples in this study can be derived through R-Closure using number size distribution data acquired through the use of particle sizing instrumentation with higher time resolutions.

3.3 Instrumentation

To compare a measured CCN concentration to an aerosol concentration, a CCN counter was operated in parallel with a TSI EEPS 3090. The EEPS spectrometer was used to obtain real time second-by-second (10 Hz) particle size distributions with 32 channels between 5.6 to 560 nm. The currents are measured 10 times per second and averaged to give a full size distribution every second. Particles are sampled at a flow rate of 10 L/min to minimize diffusional losses. Particles are charged with a unipolar corona charger and sized based on electrical mobility. With the high charging efficiency of the unipolar corona chargers, both sizing and concentrations are determined through the use of multiple electrometers (22 total, measuring the electrical current to determine the concentration).

CCN activity is measured with a Droplet Measurement Technologies, Inc. single growth column CCN Counter (CCNC). The CCNC utilizes a continuous-flow thermal gradient diffusion column to create a supersaturated environment where water vapor may condense onto CCN active aerosols to form droplets (Lance et al., 2006, Roberts and Nenes, 2005). Aerosols that are exposed to a supersaturation greater than its critical supersaturation activate and form droplets in the column. The droplets are sized and counted with an optical particle counter at the exit of the instrument. The CCNC is operated at a sheath to aerosol flow rate of 10:1 at a total flow rate of 0.5 L/min. To determine the

supersaturations in the column, the CCNC is calibrated regularly using aerosolized dry ammonium sulfate, $(NH_4)_2SO_4$, size distributions from a TSI SMPS and SMCA to determine D_d (Rose et al., 2008; Moore et al., 2010). The SMPS utilizes a long differential mobility analyzer (DMA 3081) and has a 135 second scan time. The particles are passed through a bi-polar krypton-85 charger, sized based on electrical mobility, and concentrations are counted using a butanol based CPC. SMCA setup requires the CCNC to operate in parallel with a CPC after the DMA. This allows the simultaneous measurements of the total aerosol and CCN concentrations at a given supersaturation of the monodispersed aerosols. Operating the DMA in scanning voltage mode provides CCN active aerosol fraction information over a full size distribution. The SS in the column is held constant over the course of the 135 second scan. Theoretical SS values are derived from the measured D_d values.

3.4 Experimental set up

3.4.1 Stable source aerosols: Ammonium sulfate and α-pinene SOA

Before proceeding to a transient source, the method was applied to two stable sources, atomized ammonium sulfate (AS), $(NH_4)_2SO_4$, and α-pinene secondary organic aerosol (SOA) to test the validity of the method using both C-Closure and R-Closure. The hygroscopic properties of ammonium sulfate, AS aerosols (Rose et al., 2008) and α-pinene ozonolysis (Engelhart et al., 2008) products have been well characterized, and thus, were selected for the verification. The CCNC is operated in parallel with an EEPS to obtain

simultaneous size distributions from both instruments. The experimental setup is shown in Figure 3-1. The CCN closure using C-Closure and R-closure for both the $(NH_4)_2SO_4$ aerosols and the α-pinene SOA are presented in Figure 3-2.

AS aerosols were atomized from an aqueous salt solution of AS (Acros, 99.5%) and Millipore© DI water (18 mΩ, < 100ppb), dried, and then passed over ^{210}Po to neutralize the electrostatic charge of the aerosols. To bypass possible charging errors associated with atomization, the method was further verified by oxidizing α-pinene with ozone in a dark 12.5 m^3 2mil FEP environmental chamber available at Center for Environmental Research and Technology (CE-CERT) Atmospheric Processes Laboratory (APL). A more detailed description of the chamber is available in Nakao et al. (2011). Prior to each experiment, the reactor was cleaned with pure air (Aadco 737 series air purification system). Ozone was generated by passing clean air over a Pen-Ray ultraviolet lamp (Part No. B131799, Ultra-Violet Products Inc.) and monitored with a Teledyne 400E ozone monitor. After the ozone concentrations stabilized, the α-pinene (Sigma Aldrich, 98%) was injected by passing clean air over the compound in a glass injection manifold. All experiments were completed using approximately 25 ppb of α-pinene. Any slight changes in initial concentrations <40ppb have been shown to not effect the CCN activity of the SOA (Engelhart et al., 2008). The effective density used for α-pinene SOA predictions was 1.3 g/cm^3 (Alfarra et al., 2006), and the molecular weight was 180 g/mol (Engelhart et al., 2008). Complete solubility was assumed with no dissociation (ν=1).

3.4.2 Test Fuels

A total of six ethanol and iso-butanol biofuels were selected for the fuel blends. The ethanol blends include E10 (10% ethanol and 90% gasoline), E15, E20. E10 was selected as the baseline fuel. The iso-butanol blends include B16, B24, and B32 and were selected as the oxygen equivalent of E10, E15, and E20, respectively. All fuels were match-blended according to Reid vapor pressure, and oxygen content to maintain the fuel properties of the gasoline. A more detailed description regarding fuel and blending properties are available in Karavalakis et al., (2014).

3.4.3 Emissions Testing and Test Cycles

Measurements were conducted in the University of California, Riverside (UCR) CE-CERT Vehicle Emissions Research Laboratory (VERL). VERL is equipped with a Burke E. Porter 48-inch single roller chassis dynamometer, and a constant volume sampler (CVS) for certification quality measurements. The instruments sampled directly off of the CVS tunnel. The experimental setup is shown in Figure 3-1.

A 2012 Mercedes Benz E350 (MBE350) with a spray-guided SIDI (SG-SIDI) engine was tested over the Federal Test Procedure (FTP) and California Unified Cycle (UC). The FTP is representative of city driving conditions for light duty vehicles and consists of three phases: cold start/cold three-way catalyst (TWC) converter (Phase 1), transient/stabilize (Phase 2), and hot start/warm TWC converter (Phase 3). Phase 2 is the stabilized phase. The car is turned off during the hot soak (between phases 2 and 3). The driving pattern in Phase 3 is identical to Phase 1 with the exception that the TWC is now

warm. The UC is similar to the FTP, but has higher average speeds with a higher maximum speed, less idling periods, and a greater maximum rate of acceleration. Additional information in regards to the test procedures and driving cycles are available in Karavalakis et al., (2013) and Appendix A.

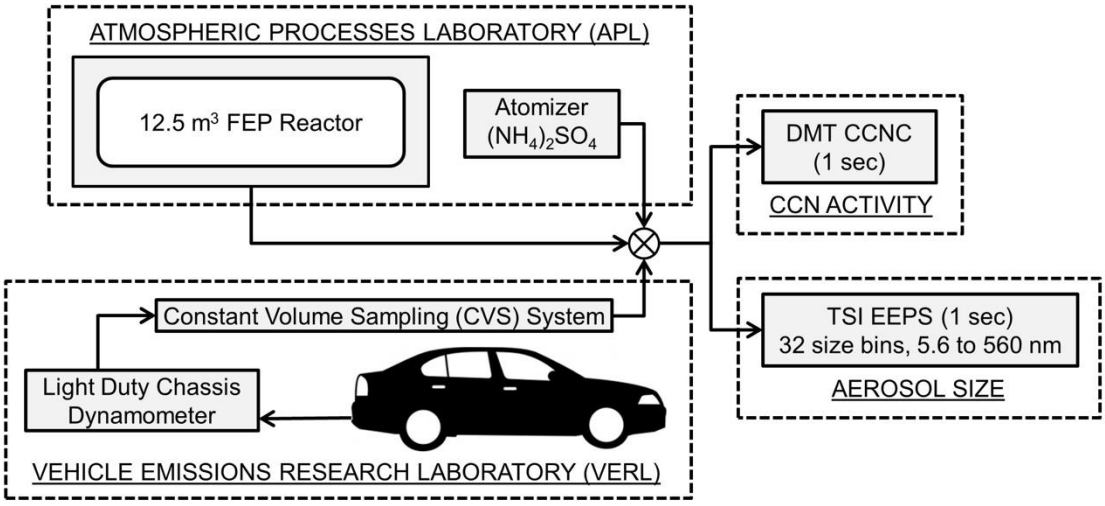

Figure 3-1. Experimental Setup

3.5 Results

3.5.1 Ammonium sulfate and α-pinene SOA: Closure assessment

C-closure and R-closure for AS aerosols is shown in Figure 3-2 (a-c). Figure 3-2a shows a slight over prediction when using C-closure for the higher supersaturations of 0.93% and 1.16 %; this can be attributed to vapor depletion effects. The higher aerosol number leads to water vapor depletion in the CCN counter column, thus CCN active aerosols that would normally activate do not have enough water available to grow to a detectable size (Lathem et al., 2011). However, when applying R-closure, the calculated

concentrations are lower (Figure 2b), which minimizes the effects seen by water depletion for this reverse fit method. C-closure and R-closure for α-pinene SOA is shown in Figure 3-2 (d-e). Similar to $(NH_4)_2SO_4$ aerosols, over prediction is observed for the α-pinene SOA C-Closure.

The critical diameter (in Figures 3-2c and 3-2f) is predicted and derived from the forced closure data set in Figures 3-2b and 3-2e. The critical diameters are compared to literature values (Köhler Theory) used in Figures 3-2a and 3-2d. The D_d derived from both closure methods for AS and α-pinene secondary organic aerosols fell within 10% and 15%, respectively. This slight deviation for the α-pinene SOA may be due to the presence of organics which have been shown to make CCN closure more difficult to achieve (e.g., but not limited to Cantrell et al., 2001; Medina et al., 2007; Martin et al., 2011). There is strong agreement between D_d derived from C-closure and R-closure for both the AS and α-pinene SOA which shows that size distributions measured by an EEPS can be used to predict CCN concentrations using R-closure.

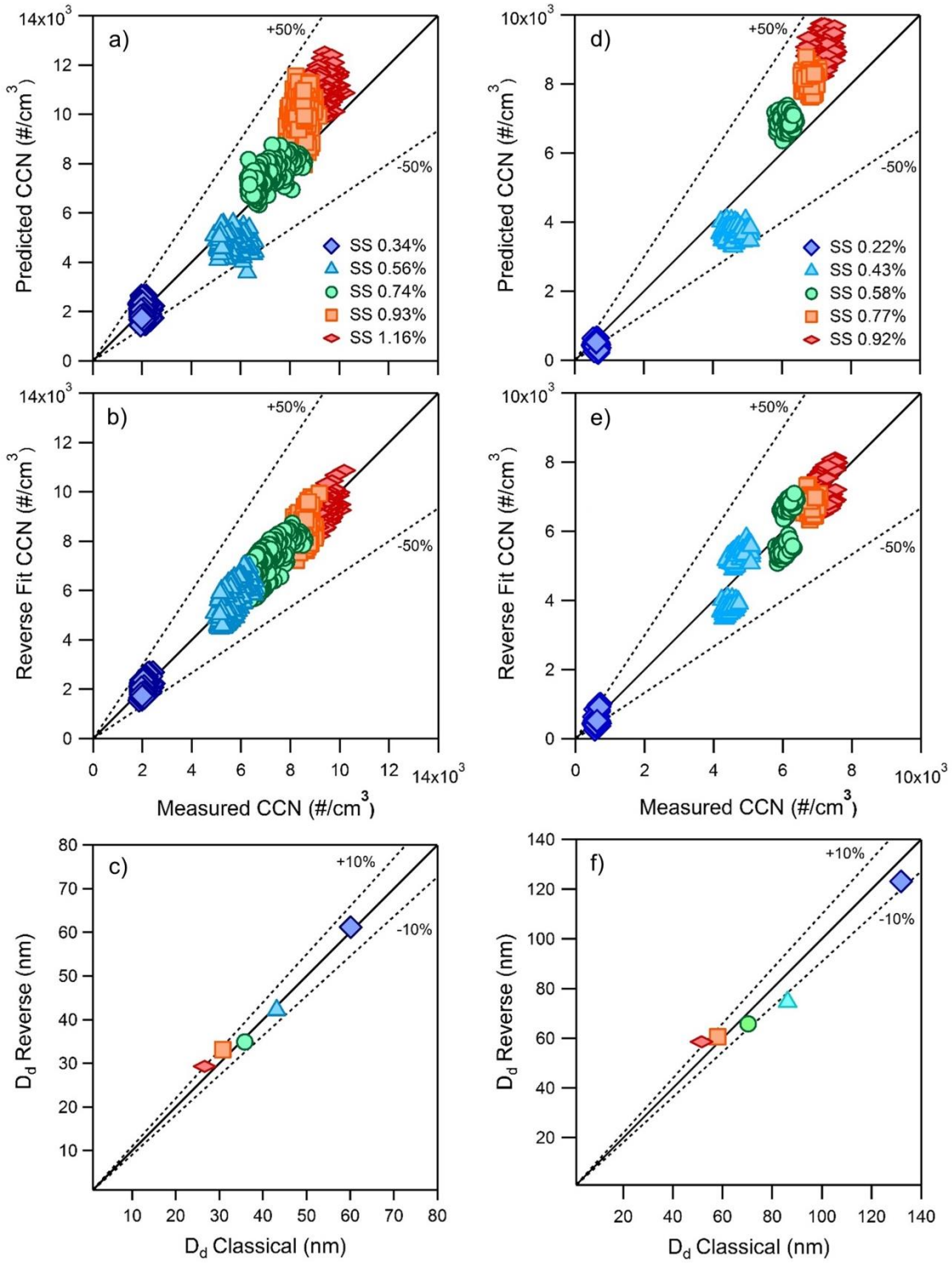

Figure 3-2. Calibrations Ammonium Sulfate A) C-Closure B) R-Closure C) Predicted Dd from R-Closure vs. Predicted Dd from C-Closure; and α-pinene SOA D) C-Closure E) R-Closure F) Predicted Dd from R-Closure vs. Predicted

3.5.2 Selecting an appropriate *SS*

The 2012 Kia Optima with a SIDI engine, operating on E20 was the first vehicle available for the study. Thus, preliminary data collected from this vehicle and fuel determined an appropriate *SS* to best achieve closure. R-closure was applied to three separate FTP cycles, where the CCNC was operated at a constant *SS* for the duration of each cycle (0.19%, 0.58%, and 0.85%). The range of *SS* were selected to represent the different supersaturations characterized for the different cloud types in the atmosphere (Seinfeld and Pandis, 1998).

For the two lowest supersaturations, FTP1 (*SS* 0.18%) and FTP2 (*SS* 0.58%), the measured CCN concentrations do not change significantly; the CCN concentrations are <<100 #/cm^{-3} with a large fraction of the values below 50 #/cm^{-3} throughout the cycle (Figure 3a, b, c). In addition, there is greater variability in predicted CCN concentrations for these lower supersaturations. This lack of closure and variability may be due to a) the lower SS, where the small temperature gradient is difficult to maintain, fluctuations in the instrument SS can result, and the signal to noise ratio may increase, thereby resulting in poorer CCN measurements (Roberts and Nenes, 2005); and b) the large vertical spread, which results from the calculated CCN from R-Closure from the EEPS data set. With low SS, and thus, low CCN concentrations, only the most hygroscopic of the sample aerosol (the upper end of the size distribution) are captured. The EEPS approximates a lognormal fit (Johnson et al., 2004; Xue et al., 2015); the CCN concentrations are derived from few size bins, resulting in fewer approximated counts. Previous work has shown the EEPS reporting lower particle concentrations than those reported by the SMPS in the high

accumulation mode range due to more fractal like particles (Zimmerman et al., 2014; Xue et al., 2015).

Significant differences were not observed between the phases as the D_d were consistently high (Figure 3d). The lower *SS* only captures the most hygroscopic aerosols and is not a good reflection of the changing CCN activity. For the high *SS*, FTP3 (SS 0.85%), instrument counting statistics improved with the higher CCN concentrations and the strongest closure was achieved. With higher CCN concentrations, a stronger signal was obtained, which allowed for stronger closure. Phase 2 (Figure 3-3b) and Phase 3 (Figure 3-3c) produce more hygroscopic particles than those emitted in Phase 1 (Figure 3-3a). Data is shown from the highest measured *SS* for the duration of the emissions testing because the high *SS* had the strongest closure and allowed differences in D_d to be observed (Figure 3-3d).

3.5.3 Iso-butanol and ethanol gasoline blends for a gasoline direct injection vehicle

The effect of ethanol and iso-butanol gasoline blends on the CCN activity of fresh emissions was investigated. CCN concentrations and size distribution measurements were collected for the MBE350 using the six different ethanol and iso-butanol blends described in Section 4.2. The CCNC was operated at *SS* between 0.83% and 1.16% over the course of the transient aerosol tests. R-Closure (Figure 4) was applied to estimate D_d.

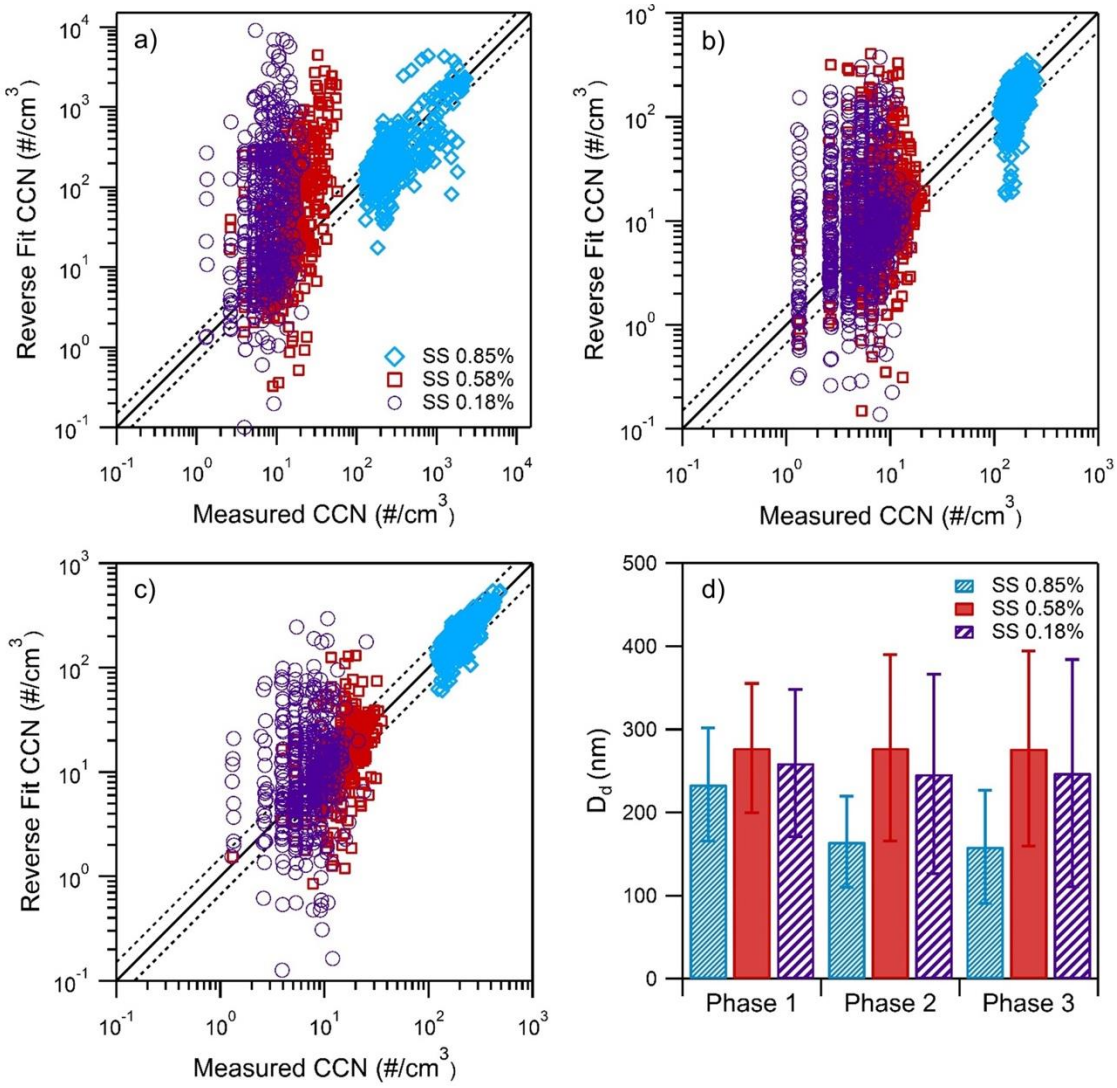

Figure 3-3. CCN R-Closure A) Phase 1 B) Phase 2 C) Phase 3. Solid lines 1:1 line, dashed is ±10%. D) Averaged Dd for each phase of driving cycle

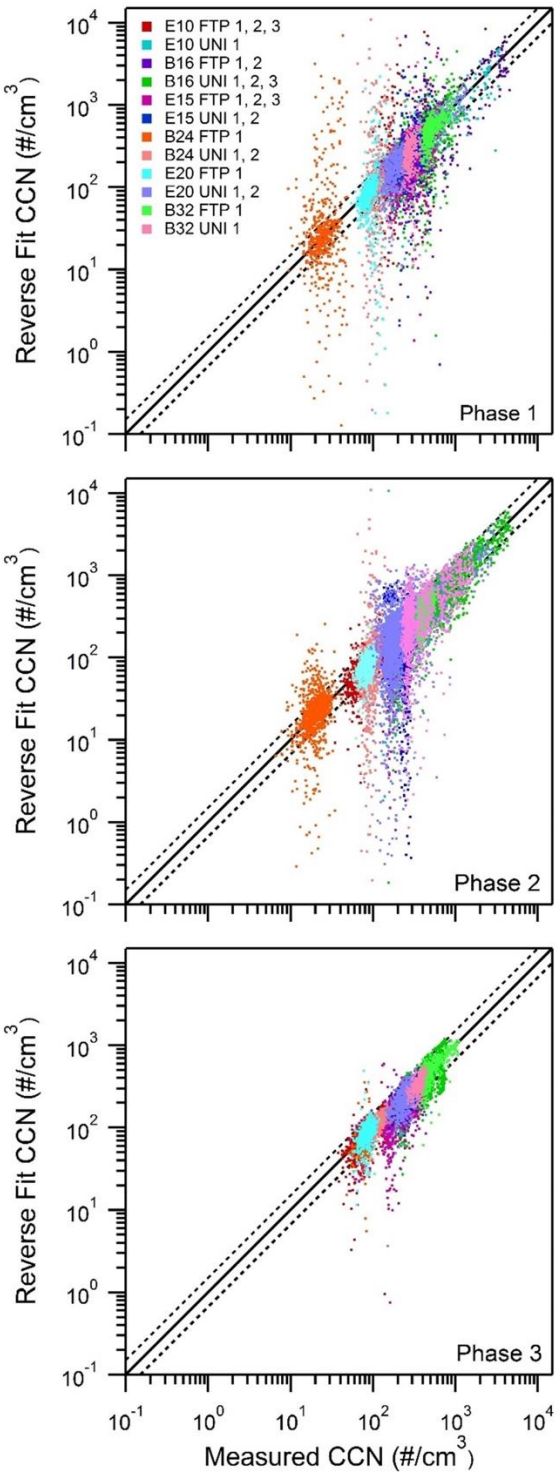

Figure 3-4. Effects of phases 1, 2, and 3 on closure

Overall, the apparent hygroscopicity is consistently low for both biofuels. Iso-butanol blends were observed to produce aerosols that were slightly more hygroscopic than that produced by the ethanol blends. Single hygroscopicity parameter, κ, values ranged from 0.0021 to 0.062 for iso-butanol blends and 0.0019 to 0.022 for ethanol blends (Figure 3-5). The error bars are the average standard deviation derived from the repetition of experiments. The errors associated with the final kappa values, when available, are small and indicate repeatability between measurements. Although this is not a significant difference between the different ethanol and iso-butanol blends, it is consistent with results from Short et al. (2015), who observed lower water insoluble mass fractions for the iso-butanol blends. The effect of alcohol concentrations was also observed; the lower alcohol blends exhibited higher κ values. Karavalakis et al., (2015) reported lower number concentrations of accumulation mode particles for E20 and B32 and in some cases, smaller geometric mean diameters were observed as well when they tested a SG-SIDI vehicle over the FTP and UC cycles. The low hygroscopicity may also be attributed to non-hygroscopic composition such as soot found in the smaller size range. Karavalakis et al. (2015) reported high soot emissions for B24 relative to other iso-butanol blends which is consistent with the low κ value for this fuel. In addition, E15 had low soot emissions relative to the other ethanol blends which is consistent with the high κ values for this fuel. This is consistent with fresh emissions not being very hygroscopic, which may require very large diameters or water soluble compounds for the CCN to activate.

Effects among the cycles were observed for the driving patterns; κ ranged from 0.0021 to 0.017 for the FTP and 0.0019 to 0.062 for the UC cycle. More hygroscopic

particles were observed for the UC cycle, which exhibits higher speeds. The higher hygroscopicity agrees with Short et al. (2015), who observed greater κ values for high steady state speeds than that of lower steady state speeds for a SIDI vehicle operating on ethanol and iso-butanol blends. In addition, the cold-start influence was particularly strong, where for most fuels the cold-start phase emitted the least hygroscopic particles with kappa ranging from 0.0021 to 0.014. Soot emissions are highest during phase 1 operating on the same biofuel blends as a result of the TWC being below its light-off temperature and thus, resulting in lower catalytic efficiency (Karavalakis et al., 2015). Phase 2 and 3 produced more hygroscopic materials and kappa values ranged from 0.0019 to 0.027 and 0.0048 to 0.062, respectively. Closure improves with the more hygroscopic aerosols in Phase 3 (Figure 3-4 and 3-5). Improvements in closure can also be attributed to the calculated concentrations staying above the lower detection limit of the EEPs.

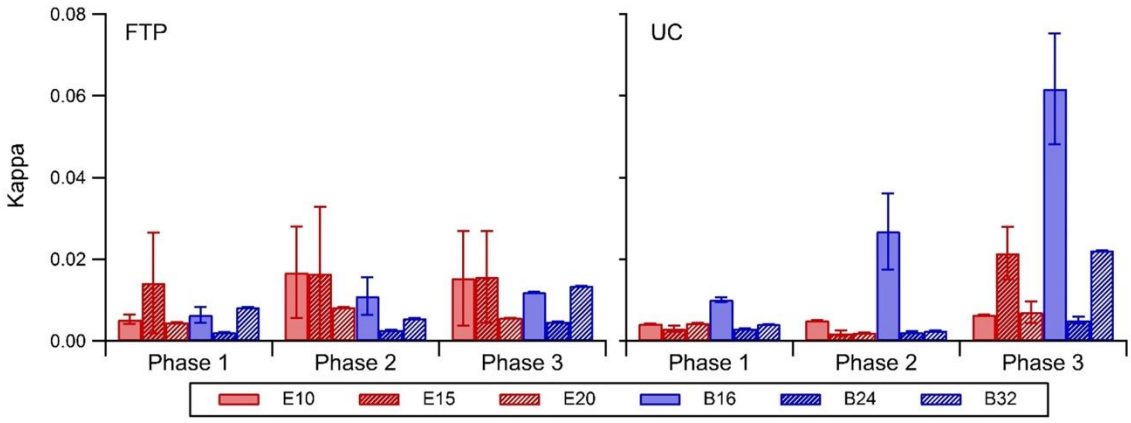

Figure 3-5. Effects of iso-butanol and ethanol fuel blends. Kappa values presented for each phase for supersaturations between 0.83% and 1.16%.

3.6 Summary

This is the first closure study to combine fast resolution CCN activation information from both a continuous CCN counter and an EEPS to study CCN activity for fresh vehicle emissions operating on ethanol and iso-butanol blends. The instrumentation and analytical methods presented are able to characterize the rapidly changing particle composition generated by vehicle accelerations. Six ethanol and iso-butanol blends were tested on a single light-duty SIDI vehicle driving on UC and FTP cycles. The fuels were selected at random for vehicle testing and initial CCN evaluation began with E20 fuel. The greatest hygroscopicity differences in fresh emissions were observed at higher supersaturations. The results suggest that the method is aptly used at higher supersaturations. At higher *SS*, small changes in aerosol composition affect droplet activation changes and derived critical diameters are more readily discerned. Although the EEPS may lack time resolution in size information, the rapid changes in hygrosocopicity of the transient aerosol system with this system can be observed. With the use of fast-time resolved CCN analysis, such as the method presented here, sources with rapidly changing aerosol composition (e.g. combustion studies, aircraft based atmospheric measurements) can be observed.

The shifts in kappa reflect the sensitivity of aerosol composition to the transient nature of the cycles and different fuels. The least hygroscopic particles occurred during Phase 1 when the catalyst was below its light-off temperature and the engine was cold. These results are consistent with the production of soot, from inefficient combustion. The most hygroscopic particles occurred during phases 2 and 3 after the catalyst was warm. Thus particles emitted during warm-start driving conditions will most likely uptake water.

The composition of emissions, particularly aerosol, can significantly change during transient drive cycles. Driving patterns inevitably change, and thus the extent to which each vehicle spends in each phase will modify particle hygroscopicity.

Overall, these fresh emissions exhibit relatively low kappa values ($\kappa < 0.1$). Fresh vehicle emissions initially have hydrophobic properties, which will inhibit the uptake of water and limit the ability to activate as cloud droplets. As a result, localized aerosols near urban sources can exhibit high variability in CCN activity. However, at regional scales where the aerosols have undergone atmospheric aging, the hygroscopicity can be modified under atmospheric conditions, such as oxidation and the condensation of soluble materials (Wittbom et al., 2014) and can exhibit higher CCN activity (Asa-Awuku et al.,2011). Small amounts of soluble material can have large effects on the water uptake properties of insoluble compounds (Bilde et al., 2004). This information collectively suggests that the aging of vehicle emission aerosols could exhibit different physical and chemical properties than the fresh aerosols emitted in this study.

To be able to account for atmospheric interactions such as transport, coagulation, and transformations, modeling atmospheric interactions is highly dependent on source emissions data. Fresh emissions may not directly play a large role in regional indirect effects. However, aerosol emissions from vehicles may be subject to rapid physical and chemical changes. With vehicle technologies changing and new fuel formulations penetrating the market, the impact of aerosol hygroscopicity for regional visibility and cloud droplet formation must be assessed. Information in regards to the amount and how CCN active these primary emissions are important as it provides a measure of their direct

contribution into the atmosphere and can aid in predicting its atmospheric aging behavior in the presence of other aerosol or gas phase species. Additional work is required to understand the evolution of fresh emissions downwind from the initial source; the processed aerosols are more likely to impact regional visibility and modify clouds. The modification of hygroscopic properties due to atmospheric aging must be explored next and compared to the results presented here.

3.7 Acknowledgements

Vehicle testing in this study was substantially supported by the California Energy Commission (CEC) under Grant Number 500-09-051. CCN work was supported by the National Science Foundation Award (NSF) 1151893. Diep Vu would like to acknowledge funding support from the U.S. Environmental Protection Agency (EPA) STAR Fellowship Assistance Agreement no. FP-91751101. Its contents are solely the responsibility of the grantee and do not necessarily represent the official views of the EPA. Further, the EPA does not endorse the purchase of any commercial products or services mentioned in the publication. Daniel Short would like to acknowledge funding support from the University of California Transportation Center (UCTC) Graduate Fellowship. The authors would like to thank Kurt Bumiller and Mark Villela for their technical contribution in conducting the emissions testing.

3.8 References

Alfarra, M. R., Paulsen, D., Gysel, M., Garforth, A. A., Dommen, J., Prévôt, A. S. H., Worsnop, D. R., Baltensperger, U., and Coe, H. (2006). A mass spectrometric study of secondary organic aerosols formed from the photooxidation of anthropogenic and biogenic precursors in a reaction chamber, Atmos. Chem. Phys. 6:5279–5293.

Andreae, M. O., Rosenfeld, D. (2008). Aerosol–cloud–precipitation interactions. Part 1. The nature and sources of cloud-active aerosols, Earth Sci. Rev. 89:13-41, doi:10.1016/j.earscirev.2008.03.001.

Asa-Awuku, A., R.H. Moore, R.H., Nenes, A., Bahreini, R., Holloway, J. S., Brock, C.A., Middlebrook, A. M., Ryerson, T. B., Jimenez, J. L., DeCarlo, P. F., Hacobian, A., Weber, R. J., Stickel, R., Tanner, D. J., Huey, L. G. (2011). Airborne cloud condensation nuclei measurements during the 2006 Texas Air Quality Study, J. Geophys. Res. 116*:D11201, doi:10.1029/2010JD014874.*

Ayala, A. and Herner, J. (2005). Transient Ultrafine Particle Emission Measurements with a New Fast Particle Aerosol Sizer for a Trap Equipped Diesel Truck, SAE Technical Paper 2005-01-3800, doi:10.4271/2005-01-3800.

Bilde, M., Svenningsson, B. (2004). CCN activation of slightly soluble organics: the importance of small amounts of inorganic salt and particle phase, Tellus B. 56:128-134, doi:10.1111/j.1600-0889.2004.00090.

Cantrell, W., Shaw, G., Cass, G., Chowdhury, Z., Hughes, L. S., Prather, K., Guazzotti, S., and Coffee, K. R. (2001). Closure between aerosol particles and cloud condensation nuclei at Kaashidhoo climate observatory, J. Geophys. Res. 106:D22.

Cheung, K. L., Polidori, A., Ntziachristos, L., Tzamkiozis, T., Samaras, Z., Cassee, F. R., Gerlofs, M., and Sioutas, C. (2009). Chemical Characteristics and Oxidative Potential of Particulate Matter Emissions from Gasoline, Diesel, and Biodiesel Cars, *Env. Sci. & Tech. 43:*6334-6340.

Dua, S., Hopke, P., and Raunemaa, T. (2009). Hygroscopicity of diesel aerosols, Water Air Soil Pollut. 112:247–257.

Dusek, U., Frank, G. P., Hildebrandt, L., Curtius, J., Schneider, J., Walter, S., Chand, D., Drewnick, F., Hings, S., Jung, D., Borrmann, S., and Andreae, M. O. (2006). Size matters more than chemistry for cloud-nucleating ability of aerosol particles, Science 312:1375–1378.

Engelhart, G. J., Asa-Awuku, A., Nenes, A., and Pandis, S. N. (2008). CCN activity and droplet growth kinetics of fresh and aged monoterpene secondary organic aerosol, Atmos. Chem. Phys. 8:3937-3949, doi:10.5194/acp-8-3937-2008.

Happonen, M., Heikkilä, J., Aakko-Saksa, P., Murtonen, T., Lehto, K., Rostedt, A., Sarjovaara, T., Larmi, M., Keskinen, J., and Virtanen, A. (2013). Diesel exhaust emissions and particle hygroscopicity with HVO fuel-oxygenate blend, Fuel 103:380-386, doi:10.1016/j.fuel.2012.09.006.

Hasegawa, S., and Ohta, S. (2002). Some measurements of the mixing state of soot-containing particles at urban and non-urban sites, Atmos. Environ. 36:3899–3908.
IPCC, 2013, Summary for Policymakers. In: Climate Change 2013 (2013). The Physical Science Basis. Contribution of Working Group I to the Fifth Assessment Report of the Intergovernmental Panel on Climate Change, Cambridge University Press, Cambridge, United Kingdom and New York, NY, USA.

Johnson, T., Caldow, R., Pöcher, A., Mirme, A., and Kittelson, D. (2004). A New Electrical Mobility Particle Sizer Spectrometer for Engine Exhaust Particle Measurements, SAE Technical Paper 2004-01-1341, doi:10.4271/2004-01-1341.

Jurányi, Z., Gysel, M., Weingartner, E., Bukowiecki, N., Kammermann, L., and Baltensperger, U. (2011). A 17 month climatology of the cloud condensation nuclei number concentration at the high alpine site Jungfraujoch, J. Geophys. Res., *116*:D10.

Kammermann, L., Gysel, M., Weingartner, E., Herich, H., Cziczo, D. J., Holst, T., Svenningsson, B., Arneth, A., and Baltensperger, U. (2010). Subarctic atmospheric aerosol composition: 3. Measured and modeled properties of cloud condensation nuclei, *J. Geophys. Res.*, 115:D04202, doi:10.1029/2009JD012447.

Karavalakis, G., Short, D., Vu, D., Villela, M., Asa-Awuku, A., and Durbin, T. (2013). Criteria Emissions, Particle Number Emissions, Size Distributions, and Black Carbon Measurements from PFI Gasoline Vehicles Fuelled with Different Ethanol and Butanol Blends, SAE Technical Paper 2013-01-1147.

Karavalakis, G., Short, D., Vu, D., Villela, M., Asa-Awuku, A., and Durbin, T. (2014). Evaluating the regulated emissions, air toxics, ultrafine particles, and black carbon from SI-PFI and SI-DI vehicles operating on different ethanol and iso-butanol blends, Fuel 128:410-21.

Karavalakis, G., Short, D., Vu, D., Russell, R., Asa-Awuku, A., Jung, H., Johnson, K., and Durbin, T. (2015). The impact of ethanol and iso-butanol blends on gaseous and particulate emissions from two passenger cars equipped with spray-guided and wall-guided direct injection SI (spark ignition) engines, Energy 82:168-179, doi:10.1016/j.energy.2015.01.023.

Karjalainen, P., Pirjola, L., Heikkilä, J., Lähde, T., Tzamkiozis, T., Ntziachristos, L., Keskinen, J., and Rönkkö, T. (2014). Exhaust particles of modern gasoline vehicles: A laboratory and an on-road study, Atmos. Envir. 97:262-270, ISSN 1352-2310, doi:10.1016/j.atmosenv.2014.08.025.

Kittelson, D.B., Watts, W.F., Johnson, J.P., Rowntree, C., Payne, M., Goodier, S., Warrens, C., Preston, H., Zink, U., Ortiz, M., Goersmann, C., Twigg, M.V., Walker, A.P., and Caldow, R. (2006). On-road evaluation of two diesel exhaust after treatment devices, J. Aerosol Sci. 37:1140-1151.

Köhler, H. (1936). The nucleus in and the growth of hygroscopic droplets, Trans. Farad. Soc., 32:1152-1161.

Lance, S., Medina, J., Smith, J. N., and Nenes, A. (2006). Mapping the Operation of the DMT Continuous Flow CCN Counter, Aeros. Sci. and Tech. 40:242-254.

Lathem, T. L., and Nenes, A. (2003). Water vapor depletion in the DMT continuous-flow CCN chamber: Effects on supersaturationa nd droplet growth, Aer. Sci. and Tech. 45:916-923.

Liu, P., and Deshler, T. (2011). Causes of Concentration Differences Between a Scanning Mobility Particle Sizer and a Condesnation Particle Counter, Aer. Sci. and Tech. 37:604-615.

Martin, M., Chang, R. Y.-W., Sierau, B., Sjogren, S., Swietlicki, E., Abbatt, J. P. D., Leck, C., and Lohmann, U. (2011). Cloud condensation nuclei closure study on summer arctic aerosol, Atmos. Chem. Phys., 11:11335-11350, doi:10.5194/acp-11-11335-2011.

Medina, J., Nenes, *A.*, Sotiropoulou, R.-E. P., Cottrell, L. D., Ziemba, L. D., Beckman, P. J., *and* R. J. Griffin *(*2007*).* Cloud condensation nuclei closure during the International Consortium for Atmospheric Research on Transport and Transformation 2004 campaign: Effects of size-resolved composition, J. Geophys. Res., 112*:D10S31, doi:10.1029/2006JD007588.*

Moore, R. H., Nenes, A., and Medina, J. (2010). Scanning Mobility CCN Analysis - A Method for Fast Measurements of Size-Resolved CCN Distributions and Activation Kinetics, Aer.Sci. & Tech. 44:861-871.

Morela, S.S., Tornatore, C., Marchitto, L., Valentino, G., and Corcione, F.E. (2012). Experimental Invesitigation of Butanol-Gasoline Blends Effects on the Combustion Process in a SI Engine, Intl. J. Energy & Env. Eng., 3:6.

Nakao, S., Shrivastava, M., Nguyen, A., Jung, H. and Cocker III, D. (2011). Interpretation of Secondary Organic Aerosol Formation from Diesel Exhaust Photo-oxidation in an Environmental Chamber, Aer. Sci. and Tech. 45:954-962.

Padró, L. T., Moore, R. H., Zhang, X., Rastogi, N., Weber, R. J., and Nenes, A. (2012). Mixing state and compositional effects on CCN activity and droplet growth kinetics of size-resolved CCN in an urban environment, Atmos. Chem. Phys. 12:10239–10255.

Petters, M. D. and Kreidenweis, S. M. (2007). A single parameter representation of hygroscopic growth and cloud condensation nucleus activity, Atmos. Chem. Phys. 7:1961-1971, doi:10.5194/acp-7-1961-2007.

Roberts, G. C. and Nenes, A. (2005). A Continuous-Flow Streamwise Thermal-Gradient CCN Chamber for Atmospheric Measurements, Aer. Sci. and Tech. 39:206-221, doi: 10.1080/027868290913988.

Rose, D., Wehner, B., Ketzel, M., Engler, C., Voigtländer, J., Tuch, T., and Wiedensohler, A. (2006). Atmospheric number size distributions of soot particles and estimation of emission factors, Atmos. Chem. Phys. 6:1021-1031, doi:10.5194/acp-6-1021-2006.

Rose, D., Gunthe, S. S., Mikhailov, E., Frank, G. P., Dusek, U., Andreae, M. O., and Pöschl, U. (2008). Calibration and measurement uncertainties of a continuous-flow cloud condensation nuclei counter (DMT-CCNC): CCN activation of ammonium sulfate and sodium chloride aerosol particles in theory and experiment, Atmos. Chem. Phys. 8:1153-1179, doi:10.5194/acp-8-1153-2008.

Rose, D., Gunthe, S. S., Su, H., Garland, R. M., Yang, H., Berghof, M., Cheng, Y. F., Wehner, B., Achtert, P., Nowak, A., Wiedensohler, A., Takegawa, N., Kondo, Y., Hu, M., Zhang, Y., Andreae, M. O., and Pöschl, U. (2011). Cloud condensation nuclei in polluted air and biomass burning smoke near the mega-city Guangzhou, China – Part 2: Size-resolved aerosol chemical composition, diurnal cycles, and externally mixed weakly CCN-active soot particles, Atmos. Chem. Phys. 11:2817-2836, doi:10.5194/acp-11-2817-2011.

Seinfeld, J. H. and Pandis, S. N. (2008). Atmospheric Chemistry and Physics: from air pollution to climate change, John Wiley & Sons, INC.

Short, D., Vu, D., Durbin, T., Karavalakis, G., and Asa-Awuku, A. (2015). Particle Speciation of Iso-Butanol and Ethanol Blended Gasoline in Light-Duty Port Fuel Injection, Vehicles, J. of Aerosol Sci. 84:39-52.

Spracklen, D. V., Carslaw, K. S., Pöschl, U., Rap, A., and Forster, P. M. (2011). Global cloud condensation nuclei influenced by carbonaceous combustion aerosol, Atmos. Chem. Phys. 11:9067-9087, doi:10.5194/acp-11-9067-2011.

Tritscher, T., Juranyi, Z., Martin, M., Chirico, R., Gysel, M., Heringa, M.F., DeCarlo, P.F., Sierau, B., Prevot, A.S.H., Weingartner, E., and Baltenspreger, U. (2011). Changes of hygroscopicity and morphology during ageing of diesel soot, Environ. Res. Lett., 6, doi:10.1088/1748-9326/6/3/034026.

Twomey, S. (1974). Pollution and the planetary albedo, Atmos. Environ. 8:1251–1256.

U.S. Environmental Protection Agency (2009). Fuels and Fuel Additives, Renewable Fuel Standard (RFS2), <http://www.epa.gov/otaq/fuels/renewablefuels/regulations.htm>.

VanReken, T. M., Rissman, T. A., Roberts, G. C., Varutbangkul, V., Jonsson, H. H., Flagan, R. C., and Seinfeld, J. H. (2003). Toward aerosol/cloud condensation nuclei (CCN) closure during CRYSTAL-FACE, J. Geophys. Res., 108, D20, doi:10.1029/2003JD003582.

Wang, J., Storey, J., Domingo, N., Huff, S., Thomas, J., and West, B. (2006). Studies of Diesel Engine Particle Emissions During Transient Operations Using an Engine Exhaust Particle Sizer, Aer. Sci. and Tech. 40:1002-1015.

Weingartner, E., Burtscher, H., Baltensperger, U. (1997). Hygroscopic properties of carbon and diesel soot particles, Atmos Environ. 31:2311–2327.

Wittbom, C., Eriksson, A. C., Rissler, J., Carlsson, J. E., Roldin, P., Nordin, E. Z., Nilsson, P. T., Swietlicki, E., Pagels, J. H., and Svenningsson, B. (2014). Cloud droplet activity changes of soot aerosol upon smog chamber ageing, Atmos. Chem. Phys., 14:9831-9854, doi:10.5194/acp-14-9831-2014.

Xue, J., Li, Y., Wang, X., Durbin, T., Johnson, K.C., Karavalakis, G., Asa-Awuku, A., Villela, M., Quiros, D., Hu, S., Huai, T., Ayala, A., and Jung, H. (2015). Comparison of vehicle exhaust particle size distributions by SMPS and EEPS during steady state operating conditions. Aer. Sci. & Tech, DOI: 10.1080/02786826.2015.1088146.

Yao, X. H., Lau, N. T., Fang, M., and Chan, C. K. (2006). On the time-averaging of ultrafine particle number size spectra in vehicular plumes, Atmos. Chem. Phys., 6:4801-4807, doi:10.5194/acp-6-4801-2006.

Zervas, E. & Dorlhène, P. (2006). Comparison of Exhaust Particle Number Measured by EEPS, CPC, and ELPI, Aer. Sci. & Tech. 40:977-984.

Zimmerman, N., Pollitt, K. J. G., Jeong, C. H., Wang, J. M., Jung, T., Cooper, J. M., Wallace, J. S. and Evans, G. J. (2014). Comparison of three nanoparticle sizing instruments: The influence of particle morphology, Atmos. Environ. 86:140–14.

Chapter 4 - Will Aerosol Hygroscopicity Change with Biodiesel and Renewable Diesel Fuels and Emission Control Technologies?

4.1 Introduction

Diesel particulate matter (PM) is associated with adverse health effects and is classified as a toxic air contaminant (CARB, 1998). In an effort to reduce diesel emissions, modern light-duty diesel vehicles are now equipped with robust emission control systems such as diesel oxidation catalysts (DOCs), diesel particulate filters (DPFs), and selective catalytic reduction (SCR) systems. These technologies have been demonstrated to effectively reduce diesel emission rates, however, under certain operating conditions, they may affect particle formation pathways, thereby modifying PM composition (Biswas et al., 2009) and enhancing the formation of ultrafine semi-volatile particles that pass through the filter. Although these ultrafine particles make up a small fraction of PM mass, they represent a higher fraction of the overall particle number count. Thus, at an equivalent mass concentration, the higher number concentrations ultrafine particles may be more detrimental to health than larger particles with the same chemically toxic composition (Zhu et al., 2002; Valavanidis et al., 2008).

DPFs effectively reduce PM emission rates but require periodic filter regenerations through PM oxidation to clear or "burn off" the soot that has accumulated on the filter. The temperature of diesel exhaust gases does not always meet the required temperature to efficiently oxidize the PM collected in the DPF. However, as a result, a variety of strategies were developed to help catalyze the regeneration reaction, such as using catalyst technology to generate nitrogen dioxide (NO_2) from the oxidation of nitric oxide (NO) to assist in the combustion of soot (Cooper et al., 2007), and using fuel-borne catalysts (FBC)

(Blanchard et al., 2002). During DPF regeneration the engine operates under different conditions from those during typical vehicle operation and DPF temperatures reach above 550ºC.

Several studies have investigated the chemical and physical properties of aerosols formed during the regeneration of DPFs for light-duty diesel passenger vehicles (e.g., Bikas and Zervas, 2007; Giechaskiel et al., 2007; Dwyer et al., 2010; Karavalakis et al., 2014). Filter regeneration can produce sharp increases in particle emissions, typically greater by multiple orders of magnitude when compared to non-regeneration operation (e.g., Bikas and Zervas, 2007; Dwyer et al., 2010). Higher emissions have also been measured immediately after a regeneration until a sufficient amount of soot builds up on the filter surface again (Mohr et al., 2006). Mohr et al. (2006) measured particle number concentrations from several vehicles with and without an evaporation tube. For one vehicle in the study, no significant difference in number concentration for measurements made using the evaporation tube during a regeneration was observed. This indicates that the regeneration derived emissions may be dominated by condensed hydrocarbons, and less by solid soot. Giechaskiel et al. (2007) measured the total solid particle number using a particle measurement programme (PMP) compliant system and determined the emitted exhaust can also consist of stored volatile material combined with lubricant oil and unburnt fuel. In addition, the regeneration of DPFs can increase the soluble organic fractions (Bikas and Zervas, 2007). During regeneration, a nucleation mode is typically present; that can be dominated by hydrocarbons and sulfate (Bikas and Zervas, 2007; Maricq et al., 2007 and references therein). DOCs can serve as a sulfur trap by storing sulfur under normal

operating conditions (250°C), which can then desorb at elevated temperatures [Kröcher et al., 2009] during regenerations that can reach above 550ºC. In addition to diesel emission control systems, fuel-based strategies (e.g., biomass-derived fuels) have been used to mitigate greenhouse gas emissions and address climate change concerns. However, the addition of oxygenated biofuels has been shown to modify the water soluble organic carbon fractions of diesel emissions (Cheung et al., 2009; Happonen et al., 2013).

Although several studies have investigated the changes in the physical and chemical nature of these aerosols derived during the regeneration of DPFs for light-duty diesel passenger vehicles, the potential impact of these alternative fuels and diesel emission control systems on aerosol hygroscopicity or its water uptake properties with regards to the cloud condensation nuclei (CCN) budget has not been explored. There is very limited information in regards to the particle CCN activity and apparent hygroscopicity during DPF regeneration, while it has been shown that the regeneration of DPFs can increase the soluble organic fractions and concentration of water soluble materials (e.g., sulfates) emitted and that the addition of oxygenated biofuels can modify the hygroscopicity. Thus, their impacts on human health, regional climate and radiative forcing in regards to the CCN budget are not well known. As a result, the objectives of this study were a) to examine the impact of fuels on the hygroscopictiy of emissions of modern technology light-duty diesel vehicles, and b) to evaluate the impact of aftertreatment control devices on the hygroscopicity particles derived from filter regeneration.

4.2 Experimental Setup

4.2.1 Test fuels, Vehicles, and Driving Cycles

Seven fuels were used in this study. Fuels include a Federal ultra-low sulfur diesel (FED ULSD) and a California Air Recourses Board (CARB) ULSD, and serve as the baseline fuels. Three fatty acid methyl esters (FAMEs), commonly known as biodiesel, produced from soybean oil (SME), animal fat oil (AFME), and waste cooking oil (WCO), respectively, and a hydrogenated vegetable oil (HVO) were utilized as blendstocks to prepare 20 volume % blends with the FED ULSD (FED ULSD/SME-20, FED ULSD/WCO-20, FED ULSD/AFME-20, FED ULSD/HVO-20). Only the WCO biodiesel was used to prepare a 20 volume % blend in the CARB ULSD (CARB ULSD/WCO-20). The main physical and chemical properties of the test fuels are shown in Table B-3.

Two 2012 model year vehicles with direct injection common-rail diesel engines and DOC, DPF, and SCR were used for this study. Vehicle 1 was tested twice over the Federal Test Procedure (FTP) cycle on each of the seven fuels. The FTP consists of three phases: a cold start phase (Phase 1), transient/stabilized operation (Phase 2), and a hot start phase (Phase 3). The Vehicles 1 and 2 were tested over two double EPA Highway Fuel Economy Test (HWFET) cycles for FED ULSD and FED/SME-20 to investigate the emissions generated during DPF regeneration. A double HWFET was conducted to provide adequate time for the regeneration to go to completion. Details of the drive cycles and speed traces for the driving cycles are shown in Fig. A-1a and Fig. B-1. Prior to the first FTP for each of the two regeneration fuels, the DPF was forced to regenerate to eliminate potential artifacts from previous fuels. One baseline double HWFET without a regeneration was

conducted for Vehicle 1 on Fed ULSD. A baseline double HWFET for Vehicle 2 is not available. Following the FTPs and the baseline double HWFETs, the vehicles were driven for ~160 miles on road to build up soot in the DPF. Double HWFETs were then conducted in a manner where the regenerations were designed to trigger and be completed during the course of the test. For Vehicle 1, the engine control module was programmed to regenerate every 170 miles so that it was ready to regenerate after the soot buildup was completed. Regeneration was triggered manually in the laboratory for Vehicle 2. Details of the regeneration testing protocol are described in Figure B-2. A more detailed description of the fuels, preconditioning protocol, and testing procedures is available in Karavalakis et al. (2014).

4.2.2 Emissions Testing and Instrumentation

All measurements were conducted at the University of California, Riverside (UCR) Center for Environmental Research and Technology (CE-CERT) Vehicle Emissions Research Laboratory (VERL). For certification quality measurements, VERL is equipped with a 48-inch single roller chassis dynamometer (Burke E. Porter), and a positive displacement pump constant volume sampling (PDP-CVS) system. PM emissions were sampled directly off of the PDP-CVS tunnel (Figure 4-1).

Supersaturated hygroscopic properties were calculated using online measurements. For the FTP and baseline double HWFET cycles, a TSI, Inc., Engine Exhaust Particle Sizer (EEPS) spectrometer 3090 was operated in parallel with a Droplet Measurement Technologies, Inc., single growth column cloud condensation nuclei counter (CCNC) to

obtain aerosol hygroscopicity measurements every second. The EEPS utilizes a unipolar corona charger and multiple electrometers to charge and measure the particles based on electrical mobility diameters. The currents are measured every 10 Hz and full size distributions are averaged second by second for 32 channels between 5.6 to 560 nm. Using a continuous-flow thermal gradient diffusion column, the CCNC generates a supersaturated environment for water vapor to condense onto hygroscopic aerosols to form droplets (Roberts and Nenes, 2005). The CCNC is operated at a total flow rate of 0.5 L/min using a sheath to aerosol flow ratio of 10:1.

For the double HWFET cycles, size resolved aerosol hygrosocopicity was measured using Scanning Mobility CCN Analysis (SMCA) (Moore et al., 2010). This method characterizes the size resolved aerosol hygroscopicity aerosol properties every 135 seconds. Using a TSI 3080 electrostatic classifier, polydispersed aerosols flow through a bi-polar krypton-85 charger and classified based on electrical mobility with a TSI, Inc., 3081L differential mobility analyzer (DMA). Next, the classified or monodispersed aerosol is split between a butanol based condensation particle counter (CPC) (TSI, Inc., 3772) and a CCNC to obtain the total aerosol concentration (CN) and the CCN active aerosol concentration, respectively. The DMA is operated in scanning voltage mode to provide size resolved aerosol hygroscopicity data over a full size distribution. The CCNC is operated at a single supersaturation, s_c, for the duration of the cycle., The CCNC was calibrated using aerosolized dry ammonium sulfate, $(NH_4)_2SO_4$,to determine the supersaturations in the column (Rose et al., 2008; Moore et al., 2010).

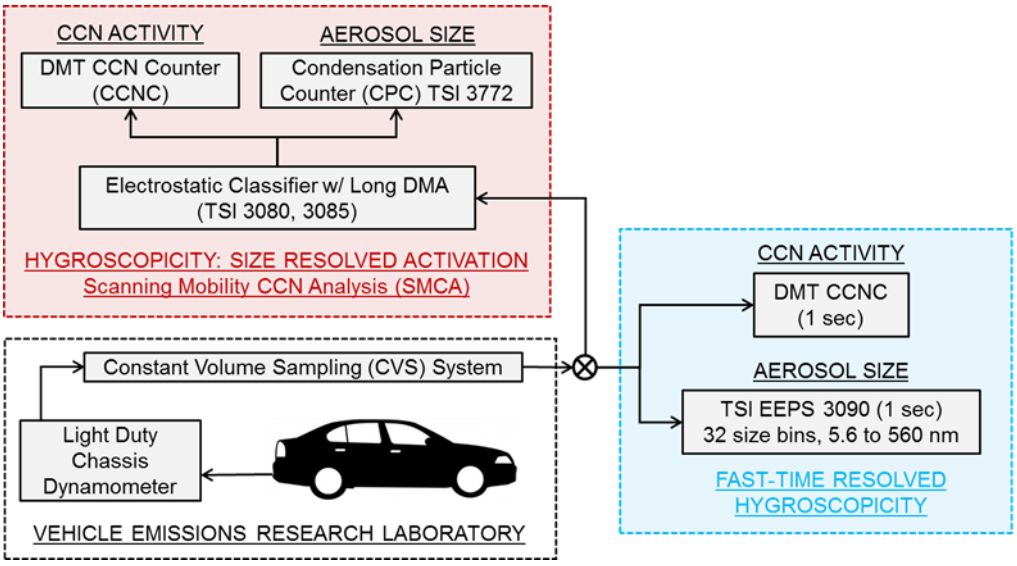

Figure 4-1. Experimental set up

4.2.3 Data Analysis

The apparent hygroscopicity is determined every second by deriving the critical activation diameter (D_d) using number size distribution data measured by the EEPS and CCN concentrations measured with the CCNC. A complete description and evaluation of the method is found in Vu et al., 2015; a brief description is provided here. D_d is derived by integrating the aerosol concentration from the largest size bin in the measured size distribution down to a D_d until the particle number concentration agrees with the measured CCN concentrations from the CCNC.

$$N_{CCN\ (measured)} = -\int_{D_{max}}^{D_d} \frac{dN}{dlogD}(D)dlogD \qquad (1)$$

Hygroscopicity calculated from Eq. (1) has been used in previous studies (e.g., but not limited to, Kammermann et al., 2010; Jurányi et al., 2011; Vu et al., 2015) and is applied to the FTP and baseline double HWFET cycles.

In anticipation of the higher concentrations expected from regenerations during the double HWFET, SMCA was utilized keep the concentration within the counting limitations of the instruments. CCN/CN are measured for a given dry diameter. D_d is determined at the point in which CCN/CN is 0.5 (Moore et al., 2010).

To describe the water uptake potential of particulate vehicle emissions, a single hygroscopcity parameter, κ, can be used. κ incorporates thermodynamic and physical properties, such as aerosol and water density (ρ_s and ρ_w, respectively), molecular weight of water (M_w), temperature (T), and droplet interfacial surface tension ($\sigma_{s/a}$), to describe particle hygroscopicity. It has been applied in studies to determine the relative hygroscopicity of complex aerosols (e.g., but not limited to, Engelhart et al., 2008; Jurányi et al., 2011; Vu et al., 2015).

With s_c, which is derived from the calibration of the CCNC, and D_d derived from one of the two above methods, κ is determined (Köhler, 1936; Petters and Kreidenweis, 2007):

$$\kappa = \frac{4A^3}{27D_d^3 ln^2 S_c}, \quad where\ A = \frac{4\sigma_{s/a} M_w}{RT\rho_w} \qquad (2)$$

where R is the universal gas constant, and S_c is the critical saturation (> 1). The critical supersaturation is defined by $s_c = S_c - 1$. The surface tension of the droplet is assumed to be equivalent to that of pure water. It is noted that the vehicle exhaust emissions may be

fractal, which can affect the electrical mobility diameter measurements and subsequent CCN activation (Nakao et al., 2011; Giordano et al., 2015). However, for the analysis of these emissions, the particles are assumed to be spherical.

4.3 Results and Discussion

4.3.1 Fuel Effects over the FTP: Vehicle 1

The effect of the seven fuels on the hygroscopic properties of fresh vehicle particle emissions operating over the FTP was examined. Size distribution measurements and CCN concentrations and were collected for Vehicle 1 using the seven fuels described in Section 2.1. The CCNC was operated at s_c = 0.54% and 0.88% for the transient aerosol tests. Second-by-second aerosol hygroscopicity measurements were used (Eqn.1).

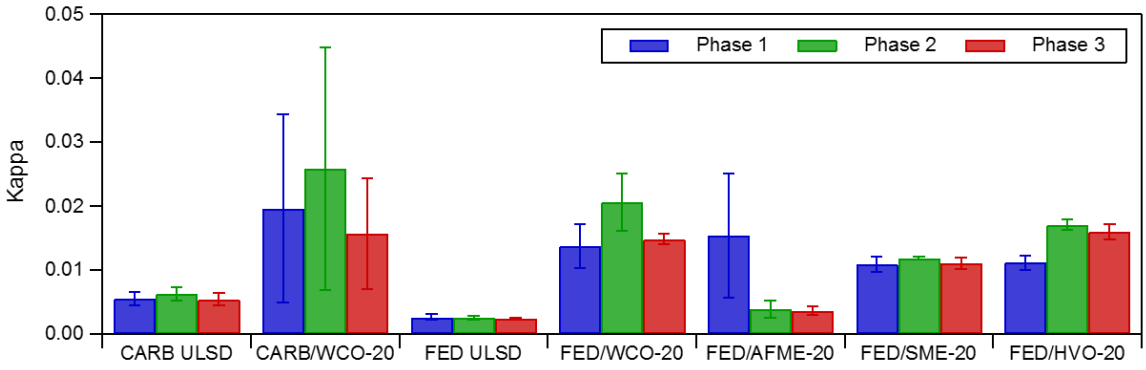

Figure 4-2. Vehicle 1 - Results of the seven different fuels.

Overall, the results indicate consistently low apparent hygroscopicities for all fuels (Fig. 4-2). Although subtle, differences were observed between different driving phases; phase 2 produces slightly more hygroscopic particles than phase 1 and phase 3. The least hygroscopic particles are observed for the Fed ULSD (κ=0.0023 to 0.0026) and the highest for the CARB/WCO-20 blend (κ=0.0157 to 0.0258). The error bars are the averaged

standard deviations obtained from the multiple FTPs for each fuel. The uncertainty associated with the kappa values are relatively small and indicate repeatability between measurements. Detailed kappa results are provided in Table B-4.

These results are consistent with studies finding fresh vehicle emissions with low hygroscopicity and are attributed to an externally mixed state where soluble material are less likely to condense, insoluble material present in the aerosols, such as soot, and small sizes where a majority of these aerosols exist in the nucleation mode (Dua et al., 1999; Weingartner et al., 1997; Hasegawa and Ohta, 2002; Andreae and Rosenfeld, 2008 and references therein; Rose et al., 2011; Tritscher et al., 2011; Vu et al., 2015). When comparing the overall apparent hygroscopicity of particles over the FTP, the results show relatively low hygroscopicity in relation to more hygroscopic species from secondary organics (κ~0.2) and inorganic aerosol species like ammonium sulfate (κ=0.61).

4.3.2 Baseline Effects over the Double HWFET: Vehicle 1

A baseline double HWFET was performed for Vehicle 1 on Fed ULSD with no regeneration. Hygroscopicity is calculated every second (Eqn. 2) during baseline testing. Overall, the apparent particle hygroscopicity was low throughout the baseline test (κ=0.0023 to 0.0026) (Figure 4-3). This range of kappa values is similar to kappa values measured during the FTP cycles for this vehicle.

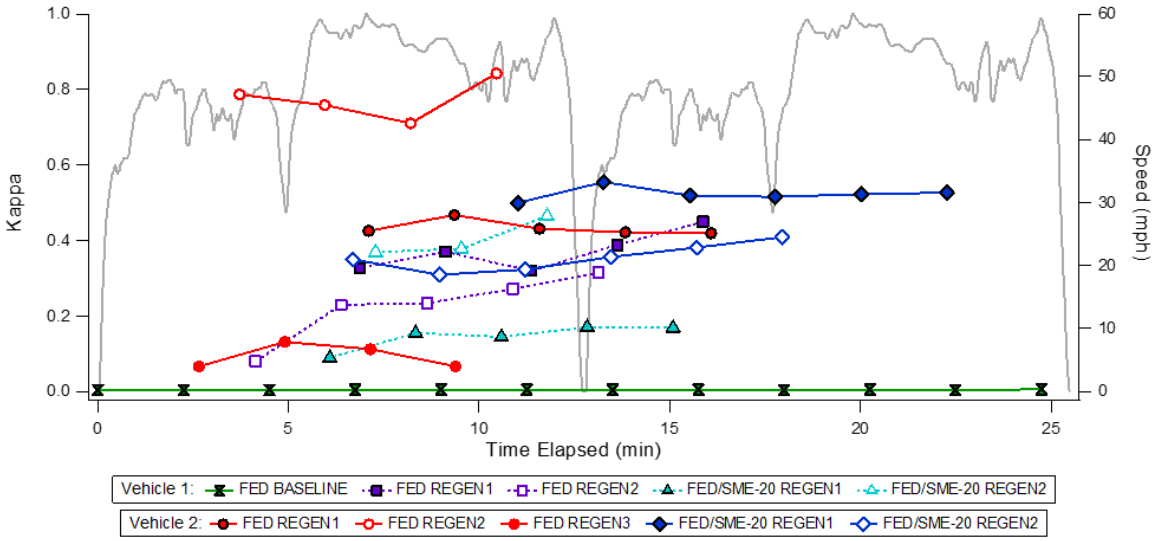

Figure 4-3. Vehicle 1 and 2 regeneration results.- Fed ULSD: one baseline cycle, two cycles w/regeneration, and Fed ULSD/SME-20: two cycles with regeneration. Vehicle 2 - Fed ULSD: three cycles with regeneration, and Fed ULSD/SME-20: two cycles with regeneration

4.3.3 Regeneration Effects over the Double HWFET: Vehicle 1 and 2

Regeneration testing was performed on Vehicle 1 and Vehicle 2 on Fed ULSD and Fed/SME-20 over the double HWFET cycles. Two double HWFET regeneration tests were performed for each of the two fuels with the exception of Vehicle 2, which had three tests on the Fed ULSD. SMCA was used to characterize the hygroscopicity properties. These results are summarized in Figure 4-3 with detailed kappa results in Tables B-5 and B-6.

For Vehicle 1 and 2 the regenerations lasted approximately 7 to 12 minutes and 11 to 22 minutes, respectively. The length of regeneration and the amount of PM emitted can vary as they are a function of the driving patterns of the vehicle (e.g., steady-state high speed cycles) and mileage accumulation (Dwyer et al., 2010). All regeneration events were

signified by elevated exhaust emissions and exhaust temperatures for both vehicles. Size and concentration data (EEPS) are only available for Vehicle 1 (Figure 4-4).

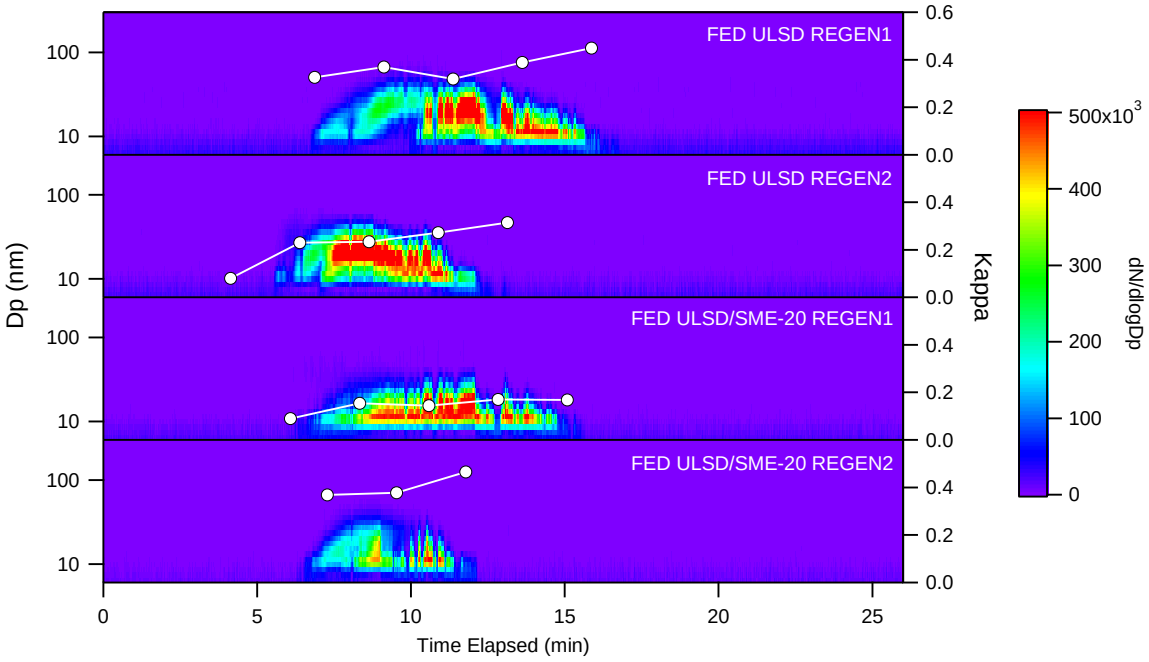

Figure 4-4. Vehicle 1 Regenerations. Particle size distributions shown (left axis) and kappa (right axis) as a function of time elapsed.

A large nucleation mode is observed, which is consistent with other studies conducting regenerations (Maricq et al., 2007 and references therein). The fuels are not observed to effect the size distributions.

The highest hygroscopicity is observed for the aerosols emitted during regeneration for both vehicles and both fuels; with average κ values ranging from 0.242 to 0.434 (Figure 4-5). The highest and lowest hygroscopicity was observed for Vehicle 2 on the FED ULSD (κ =0.843 and κ =0.0661).

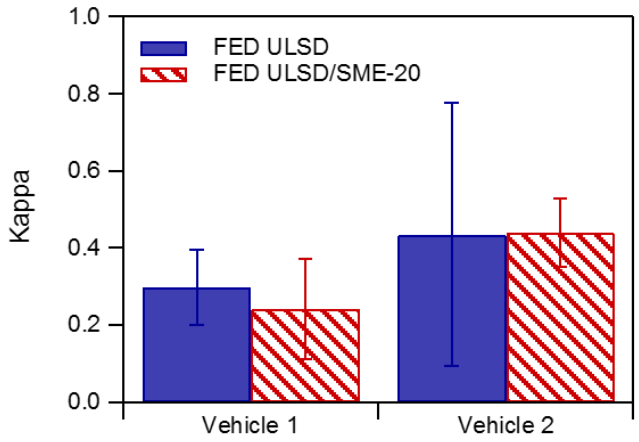

Figure 4-5. Average Kappa values for the regeneration events

Additional kappa values are available in Table B-7. The higher kappa values may be attributed to the higher amount of sulfates released during regeneration (derived from sulfur on the soot particles, sulfur in the DPF). This is consistent with those from Bikas and Zervas (2007) who observed an increase in the nucleation nanoparticles which consisted mostly of HC or sulfates during the regeneration of a non-catalyzed SiC filter and a Pt catalyst retrofitted on a passenger car equipped with a 1.9 L diesel Euro4 engine. They found soluble organic fractions increased during regeneration from 0 to 50%, which were determined to be composed of hydrocarbons with 77% from fuel and the remaining 23% from engine oil. In addition, sulfates made up 12% of the total PM (from 3% before regeneration) and were correlated with increased fuel consumption, higher DPF temperatures, increased sulfate concentrations with larger diameter particles (median diameter of 40 nm). Both vehicles 1 and 2 had lower fuel economy during the DPF regenerations (Karavalakis et al., 2014), thereby increasing the amount of sulfur due to increased fuel consumption.

Sulfur may play an important role in elevating aerosol emission hygroscopicity. To drive the regeneration, ULSD may be injected to lower the required DPF temps for regeneration. An increase in fuel consumption during regeneration measurements can result in an increase in SO_2 (Bikas and Zervas, 2007). Studies suggest that SO2 may be oxidized to SO3 in the catalyst and lead to the formation of sulfate particles in the nucleation mode (Biswas et al., 2009). DOCs can serve as a sulfur trap and store a large fraction of the emitted SO_2; which can oxidize to form SO_3. This can then form sulfuric acid in the presence of water or sulfates with metal oxides (e.g., alumina, titania, zirconia) on the surface of the DOC (Kröcher et al., 2009). This process is irreversible and the sulfuric acid/SO_x can begin desorbing at temperatures as low at 250°C (Kröcher et al., 2009). Sulfuric acid is very hygroscopic, with a reported kappa value of 0.9 (Petters and Kredenweis, 2007). If mixed with less soluble materials, sulfuric acid may greatly modify the CCN activity. Aerosols internally mixed with sulfuric acid vapor can be highly hygrosopic (Khalizov et al., 2009). The observed large kappa values (> 0.8) may be due to sulfuric acid or interactions of SO_x with water vapor in the exhaust or the CCN. It should also be noted that SCR systems use urea to reduce NO_x, ammonia slip may be occurring due to the urea injection system. This ammonia may potentially react with sulfuric acid to form ammonia sulfate, which has a kappa value of 0.61 (Petters and Kredenweis, 2007).

4.4 Summary

This is the first study to investigate the supersaturated hygroscopic properties of particle emissions derived from the regeneration of DPFs while operating on a

commercially available ULSDs and biodiesel blends. For the FTP tests for Vehicle 1, although subtle, the changes in kappa indicate the sensitivity of the chemical composition to the different renewable and biodiesel fuels and the transient nature of the drive cycle. Overall, kappa values did not display any significant differences; emissions directly from the tail-pipe exhibit low kappa values and are consistent with fresh vehicle aerosol emissions typically classified as non-hygroscopic.

Regeneration can produce significantly more particle emissions and the particle hygroscopicity during regeneration was considerably higher than that of the non-regeneration cycles; reaching average kappa values of 0.242 to 0.434, but upwards of 0.843. This indicates the presence of highly soluble materials, which even in small amounts, may greatly effect the water uptake properties of compounds that are insoluble (Bilde et al., 2004).

DPF regeneration increases both particle number and hygroscopicity. The potential impact of modifying a significant fraction of the modern vehicle fleet with diesel engine technologies such as DPFs may have unforeseen environmental consequences. Vehicle emissions are traditionally characterized as non-hygrosopic in radiative forcing estimates. However, this work indicates that diesel vehicle emissions will move from non-hygroscopic to hygroscopic in nature due to the regeneration of the filters. DPFs collect a majority of the PM emissions, but during the oxidation and regeneration process, the particle number and hygroscopic properties are both modified. Current emissions testing that does not incorporate regeneration is not fully representative of the emissions from modern diesel vehicle equipped with these diesel emission control technologies. As more

vehicles continue to utilize this technology, the impact on local health, regional visibility, and climate due to the application of these diesel emission control systems becomes increasingly important and should be evaluated in future studies.

4.5 Acknowledgements

Data used in this study are available in Supporting Information. Vehicle testing in this study was substantially supported by the Coordinating Research Council (CRC) (Project No. AVFL-17b). Aerosol hygroscopicity work was supported by the National Science Foundation Award (1151893). D.V. acknowledges support from the U.S. Environmental Protection Agency STAR Fellowship (FP-91751101). This work is the sole responsibility of the grantee and does not represent the official views of any funding agencies. D.S. acknowledges support from the University of California Transportation Center Graduate Fellowship. The authors additionally thank Kurt Bumiller and Mark Villela for their technical contribution during vehicle testing.

4.6 References

Andreae, M. O., Rosenfeld, D. (2008). Aerosol–cloud–precipitation interactions. Part 1. The nature and sources of cloud-active aerosols, Earth Sci. Rev., 89, 13-41, doi:10.1016/j.earscirev.2008.03.001.

Asa-Awuku, A., R.H. Moore, R.H., Nenes, A., Bahreini, R., Holloway, J. S., Brock, C.A., Middlebrook, A. M., Ryerson, T. B., Jimenez, J. L., DeCarlo, P. F., Hacobian, A., Weber, R. J., Stickel, R., Tanner, D. J., Huey, L. G. (2011). Airborne cloud condensation nuclei measurements during the 2006 Texas Air Quality Study, J. Geophys. Res., 116, D11201, doi:10.1029/2010JD014874.

Bikas, G. and Zervas, E. (2007). Regulated and Non-Regulated Pollutatns Emitted during the Regeneration of Diesel Particulate Filter., Energy Fuels, 21, 1543–1547, doi: 10.1021/ef070024s.

Biswas, S., Verma, V., Schauer, J., and Sioutas, C. (2009). Chemical speciation of pm emissions from heavy-duty diesel vehicles equipped with diesel particulate filter (dpf) and selective catalytic reduction (scr) retrofits, Atmospheric Environment, 43, 1917-1925.

Blanchard, G., Colignon, C., Griard, C., Rigaudeau, C., Slavat, O., and Seguelong, T. (2002). Passenger Car Series Application of a New Diesel Particulate Filter System Using a New Ceria-Based Fuel-Borne Catalyst: From the Engine Test Bench to European Vehicle Certification, SAE Technical Paper 2002-01-2781, doi:10.4271/2002-01-2781

Cantrell, W., Shaw, G., Cass, G., Chowdhury, Z., Hughes, L. S., Prather, K., Guazzotti, S., and Coffee, K. R. (2001). Closure between aerosol particles and cloud condensation nuclei at Kaashidhoo climate observatory, J. Geophys. Res., 106, D22.

CARB, 1998. Proposed identification of diesel exhaust as a toxic air contaminant, Appendix III, Part A: exposure assessment.

Cheung, K. L., Polidori, A., Ntziachristos, L., Tzamkiozis, T., Samaras, Z., Cassee, F. R., Gerlofs, M., and Sioutas, C. (2009). Chemical Characteristics and Oxidative Potential of Particulate Matter Emissions from Gasoline, Diesel, and Biodiesel Cars, Env. Sci. & Tech., 43, 6334-6340.

Cooper, B., Jung, H., and Thoss, J. Treatment of Diesel Exhaust Gases, United States Patent; 4902487. Johnson Matthey, Inc., Valley Forge, Pa. February 20, 1990.

Dwyer, H., Ayala, A., Zhang, S., Collins, J., Huai, T., and Herner, J., and Chau, W. (2010). Emissions from a diesel car during regeneration of an active diesel particulate filter, J. Aerosol Sci., 41, 541-552.

Dua, S., Hopke, P., and Raunemaa, T. (2009). Hygroscopicity of diesel aerosols, Water Air Soil Pollut. 112, 247–257.

Engelhart, G. J., Asa-Awuku, A., Nenes, A., and Pandis, S. N. (2008). CCN activity and droplet growth kinetics of fresh and aged monoterpene secondary organic aerosol, Atmos. Chem. Phys., 8, 3937-3949, doi:10.5194/acp-8-3937-2008.

Giechaskiel, B., Munoz-Bueno, R., Rubino, L., Manfredi, U., Dilara, P., De Santi, G., and Andersson, J. (2007). Particle Measurement Programme (PMP): Particle Size and Number Emissions Before, During and After Regeneration Events of a Euro 4 DPF Equipped Light-Duty Diesel Vehicle., SAE Technical Paper 2007-01 1944, doi:10.4271/2007-01-1944.

Giordano, M., Espinoza, C., and Asa-Awuku (2015). Experimentally measured morphology of biomass burning aerosol and its impacts on CCN ability, Atmospheric Chemistry and Physics, 15, 1807-1821, doi:10.5194/acp-15-1807-2015.

Happonen, M., Heikkilä, J., Aakko-Saksa, P., Murtonen, T., Lehto, K., Rostedt, A., Sarjovaara, T., Larmi, M., Keskinen, J., and Virtanen, A. (2013). Diesel exhaust emissions and particle hygroscopicity with HVO fuel-oxygenate blend, Fuel, 103, 380-386, doi:10.1016/j.fuel.2012.09.006.

Hasegawa, S., and Ohta, S. (2002). Some measurements of the mixing state of soot-containing particles at urban and non-urban sites, Atmos. Environ, 36, 3899–3908.

Jurányi, Z., Gysel, M., Weingartner, E., Bukowiecki, N., Kammermann, L., and Baltensperger, U. (2011). A 17 month climatology of the cloud condensation nuclei number concentration at the high alpine site Jungfraujoch, J. Geophys. Res., 116, D10.

Khalizov, A. F., R. Zhang, D. Zhang, H. Xue, J. Pagels, and P. H. McMurry (2009). Formation of highly hygroscopic soot aerosols upon internal mixing with sulfuric acid vapor, J. Geophys. Res., 114, D05208, doi:10.1029/2008JD010595.

Kammermann, L., Gysel, M., Weingartner, E., Herich, H., Cziczo, D. J., Holst, T., Svenningsson, B., Arneth, A., and Baltensperger, U. (2010). Subarctic atmospheric aerosol composition: 3. Measured and modeled properties of cloud condensation nuclei, J. Geophys. Res., 115, D04202, doi:10.1029/2009JD012447.

Karavalakis G., Durbin, T., and Russell R. (2014). CRC Final Project Report: CRC Project No. AVFL – 17b: Biodiesel and Renewable Diesel Characterization and Testing in Modern LD Diesel Passenger Cars and Trucks.

Köhler, H. (1936). The nucleus in and the growth of hygroscopic droplets, Trans. Farad. Soc., 32, 1152-1161.

Kröcher, O., Widmer, M., Elsener, M., and Rothe, D. (2009). Adsorption and Desorption of SO_x on Diesel Oxidation Catalysts, Ind. Eng. Chem. Res., 48, 9847-9857

Maricq, M. (2007). Chemical characterization of particulate emissions from diesel engines: A review, J. Aer. Sci., 28, 1079-1118.

Moore, R. H., Nenes, A., and Medina, J. (2010). Scanning Mobility CCN Analysis - A Method for Fast Measurements of Size-Resolved CCN Distributions and Activation Kinetics, Aer.Sci. & Tech., 44, 861-871.

Mohr, M., Forss, A., and Lehmann, U. (2006). Particle Emissions from Diesel Passenger Cars Equipped with a Particle Trap in Comparison to Other Technologies. Env. Sci. and Tech., 40, 2375-2383.

Nakao, S., Shrivastava, M., Nguyen, A., Jung, H. and Cocker III, D. (2011). Interpretation of Secondary Organic Aerosol Formation from Diesel Exhaust Photo-oxidation in an Environmental Chamber, Aer. Sci. and Tech., 45, 954-962.

Petters, M. D. and Kreidenweis, S. M. (2007). A single parameter representation of hygroscopic growth and cloud condensation nucleus activity, Atmos. Chem. Phys., 7, 1961-1971, doi:10.5194/acp-7-1961-2007.

Roberts, G. C. and Nenes, A. (2005). A Continuous-Flow Streamwise Thermal-Gradient CCN Chamber for Atmospheric Measurements, Aer. Sci. and Tech., 39, 206-221, doi: 10.1080/027868290913988.

Rose, D., Gunthe, S. S., Mikhailov, E., Frank, G. P., Dusek, U., Andreae, M. O., and Pöschl, U. (2008). Calibration and measurement uncertainties of a continuous-flow cloud condensation nuclei counter (DMT-CCNC): CCN activation of ammonium sulfate and sodium chloride aerosol particles in theory and experiment, Atmos. Chem. Phys. 8, 1153-1179, doi:10.5194/acp-8-1153-2008.

Rose, D., Gunthe, S. S., Su, H., Garland, R. M., Yang, H., Berghof, M., Cheng, Y. F., Wehner, B., Achtert, P., Nowak, A., Wiedensohler, A., Takegawa, N., Kondo, Y., Hu, M., Zhang, Y., Andreae, M. O., and Pöschl, U. (2011). Cloud condensation nuclei in polluted air and biomass burning smoke near the mega-city Guangzhou, China – Part 2: Size-resolved aerosol chemical composition, diurnal cycles, and externally mixed weakly CCN-active soot particles, Atmos. Chem. Phys., 11, 2817-2836, doi:10.5194/acp-11-2817-2011.

Tritscher, T., Juranyi, Z., Martin, M., Chirico, R., Gysel, M., Heringa, M.F., DeCarlo, P.F., Sierau, B., Prevot, A.S.H., Weingartner, E., and Baltenspreger, U. (2011). Changes of hygroscopicity and morphology during ageing of diesel soot, Environ. Res. Lett., 6, doi:10.1088/1748-9326/6/3/034026.

Vu, D., Short., D., Karavalakis, G., Durbin, T. D., and Asa-Awuku, A. (2015). Integrating cloud condensation nuclei predictions with fast time resolved aerosol instrumentation to determine the hygroscopic properties of emissions over transient drive cycles, Aer. Sci. & Tech., 49, 1149-1159, doi: 10.1080/02786826.2015.1105358.

Valavanidis, A., Fiotakis, K., & Vlachogianni, T. (2008). Airborne particulate matter and human health: Toxicological assessment and importance of size and composition of particles for oxidative damage and carcinogenic mechanisms. Journal of Environmental Science and Health - Part C Environmental Carcinogenesis and Ecotoxicology Reviews, 26, 339-362.

Weingartner, E., Burtscher, H., Baltensperger, U. (1997). Hygroscopic properties of carbon and diesel soot particles, Atmos Environ. 31, 2311–2327.

Zelenka, P., Schmidt, S., and Elfinger, G. (2001). An Active Regeneration Aid as a Key Element for Safe Particulate Trap Use, SAE Technical Paper 2001-01-3199, doi:10.4271/2001-01-3199.

Zhu, Y., Hinds, W., Kim, S., and Sioutas, C. (2002). Concentration and Size Distribution of Ultrafine Particles Near a Major Highway, J. of the Air & Waste Management Association, 52, 1032-1042.

Chapter 5 – Using a New Mobile Atmospheric Chamber to Investigate Aged Gasoline Vehicle Emissions, Part I

5.1 Introduction

Vehicle emissions are an important source of volatile and semi-volatile organic compounds, NO_x, CO and particulate matter, which can contribute to secondary organic aerosol and ozone formation in the environment. Gasoline vehicle emissions are a large source of secondary organic aerosol (SOA) precursors in urban areas; gasoline derived SOA was estimated to exceed POA by a factor of three when exposed to atmospherically relevant concentrations of OH ($5x10^7$ molecules cm^{-3} h) (Bahreini et al., 2012). As a result, several studies have focused on identifying the chemical species that contribute to SOA formation. However, the chemical and physical properties of gasoline emissions can vary with the different vehicle types, fuel sources, and driving conditions thereby making the characterization of gasoline SOA challenging.

Previous work has characterized the physical and chemical properties of primary and secondary emissions from different types of vehicles operating on idling conditions and certification quality drive cycles (e.g., but not limited to, Liu et al., 2015; Gordon et al. 2014; May et al., 2014; Platt et al., 2013). Consistent with Bahreini et al. (2012), Nordin et al. (2013) observed significant SOA formation (SOA:POA of 9 to 500) when investigating the SOA formation of emissions derived from warm idling euro LDGVs. This is consistent with Liu et al. (2015) who investigated the SOA formation of two Euro1 and Euro 4 port fuel injection (PFI) light duty gasoline vehicles (LDGV) under warm idling conditions. Large SOA to POA ratios of 12 to 259 (OH exposure of $5x10^6$ molecules cm^{-3} h) was

observed; a large fraction of the SOA formation was attributed to single-ring aromatic precursors and naphthalene. Likewise, Nordin et al. (2014) estimated 60% of the SOA derived from C6-C9 aromatics. The unspeciated non-methane precursors contributed largely to SOA formation as well and have been found to derive from highly oxygenated hydrocarbons (Platt et al. 2013) and branched and cyclic alkanes (Gordon et al., 2014). However, many of these studies focused more on the older technology vehicles, such as Port Fuel Injection (PFI) vehicles, with less attention on current generation vehicles such as gasoline direct injection (GDI) vehicles.

Fresh gasoline vehicle emissions are not hygroscopic and have been characterized with low cloud condensation nuclei (CCN) activity (Vu et al., 2015). However, the primary emissions can undergo physical and chemical changes (e.g. condensation or coagulation of soluble materials, chemical oxidation), which may strongly modify its water uptake properties. Knowledge on SOA and its effect on cloud droplet formation from different gasoline vehicle emissions is limited.

With the push to reduce fuel consumption, GDI technology is estimated to become the preferred standard for gasoline light-duty vehicles in the United States (CARB, 2010). In addition to greater fuel efficiency, GDI technology offers greater specific output and lower CO_2 emissions than conventional PFI engines. However, a drawback of GDI technology is that it emits more particle mass emissions than PFI engines (Karavalakis et al., 2014; Liang et al., 2013). Because of the direct injection of fuel into the combustion chamber, fuel impingement on the piston walls during combustion could lead to higher soot formation

and total hydrocarbons emissions. This effect may be more prominent during cold starts when the three way catalyst (TWC) is cold and the oxidation efficiency is low.

There are currently a handful of smog chambers in use (Cocker et al., 2001; Carter et al., 2005; Leskinen et al., 2015; Liu et al., 2015, Platt et al., 2013, Presto et al. 2011). However, many of these chambers do not have access to chassis dynamometers. For the chambers that do, some of the current mobile chambers have been restricted to a smaller volume to improve mobility (Gordin et al, 2014; Platt et al., 2013). This lowers the surface area to volume ratio and may affect the wall loss rates. Currently, the UCR Chemical Engineering Center for Environmental Research and Technology (CE-CERT) houses a number of research facilities; this includes the atmospheric processes Laboratory (APL) and Vehicle Emissions Research Laboratory (VERL). However, they are not housed directly next to each other. To overcome these limitations, a new UCR Mobile Atmospheric Chamber (MACh) has been designed to integrate the vehicle emissions testing capabilities at the VERL with state-of-the art gas and particle phase instrumentation at APL as a means of characterizing aged emissions sources from driving cycles that are representative of real world driving conditions that are both repeatable and controlled. MACh is ~30 m^3, thereby making it one of the largest mobile chambers currently available. The chamber is placed directly next to the vehicle in the test cell during the emissions collection period and then transported to APL to be photochemically aged. As a result, all experiments are now able to be completed in-house at the research facilities available at CE-CERT.

This work is divided into two parts; a) a brief characterization of a new mobile atmospheric chamber (MACh) that has been designed to interface the vehicle emissions

research laboratory with APL at CE-CERT and b) the demonstration of the functionality of MACh by investigating the effect of photochemically aging emissions for two modern light duty passenger GDI vehicles while operating on a chassis dynamometer. Results of the characterization runs and vehicle testing are presented.

5.2 Methods and Materials

5.2.1 Mobile atmospheric chamber

MACh consists of a single collapsible ~30m^3 2 mil FEP fluoropolymer film (Saint Gobain) chamber, thereby making it one of the largest mobile atmospheric reactors currently available. Some aspects of MACh design are similar to those presented in Carter et al. (2005) and Nakao et al. (2012). This chamber was designed and then constructed in house. The seams were carefully completed using a heat sealer and reinforced with polyester film tape (3M HD 8403). The large volume (surface to volume ratio of ~2.2:1) and the non-reactive chamber material was selected to help minimize wall loss of aerosols (POA/SOA) and semi volatile precursors. Another beneficial feature of the Teflon material is its relatively good resistance to small temperature changes thus minimizing temperature fluctuations inside the chamber when transporting the chamber between facilities. One wall of the chamber has an aluminum sampling plate that has been sealed in the same FEP fluoropolymer film as the chamber. Is it equipped with multiple stainless steel, Teflon, and jaco sampling and injection ports.

The reactor itself is housed in a mobile aluminum frame constructed of aluminum extrusions and anodized aluminum sheets fixed with wheels and a large UV blocking tarp.

This enables the chamber to be transported between the different research facilities housed at CE-CERT thereby allowing MACh to be positioned close to the combustion source during the primary emissions sampling period. After collecting samples, MACh is transported to APL to be aged with black lights and characterized with state-of-the-art particle and gas phase instrumentation.

5.2.2 **Light source and chamber enclosure**

Emissions are photochemically aged with a controlled ultra violet light source consisting of 600 15W 18" black lights mounted onto two walls of the enclosure. The interior of the chamber enclosure is covered with anodized aluminum sheets (4250E Super UltraBrite 95, ACA Corp.) to maximize light intensity throughout the chamber. The irradiance spectrum was measured with a LI-COR 1800 spectroradiometer and normalized to the highest peak (mercury line at 436nm) (figure 5-1). The peak intensity is at 365nm (with a range of 300-430nm). UV lights are not representative of the ground level spectrum, but provide an adequate substitute for sunlight and covers the range for many important atmospheric trace gases such as OH radicals, O_3, HONO, HCHO, and NO_2 (Carter et al., 1995). A limitation of these black lights is that it provides an unnatural spectrum in the higher wavelength which may affect photochemical processes such as the photolysis of NO_3 radicals and certain aromatic products.

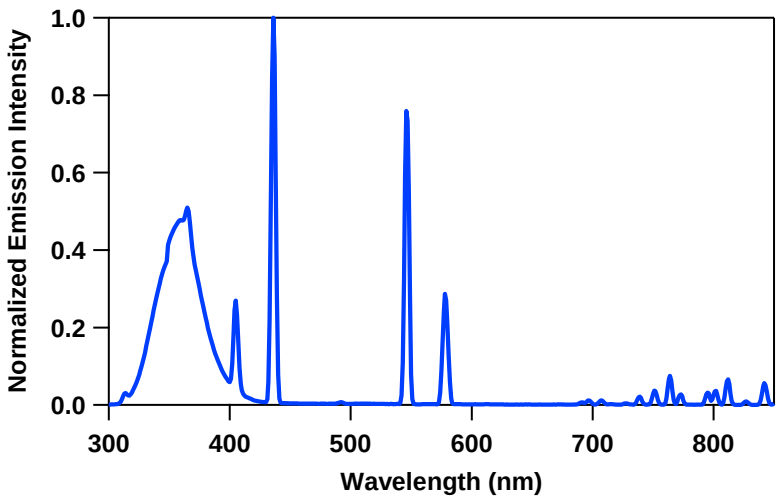

Figure 5-1. Irradiance Spectrum of UV black lights

The photolysis rate (k_1) of NO_2, was determined through a series of actinometry experiments (Seinfeld and Pandis, 1998). A known concentration of NO_2 was injected into a quartz tube placed in the center of the enclosure and irradiated with the black lights. NO_x was recorded and used to determine the photolysis rate.

$$k_1 = \frac{k[NO][O_3]}{[NO_2]} \qquad (1)$$

NO_2 photolysis rate was determined to be 0.23 min^{-2}. To modify the light intensity, the black lights were distributed among 30 individual light panels to allow different lighting configurations.

5.3 Reactor conditioning and characterization runs

Prior to the first characterization run, the chamber was conditioned with pure air and high concentrations of both ozone and OH radicals formed by irradiating H_2O_2. Ozone was

generated by passing clean air over a Pen-Ray ultraviolet lamp (Part No. B131799, Ultra-Violet Products Inc.). To minimize background effects, pure dry air that is free of particles, non-methane hydrocarbons, and NO_x was generated with an AADCO 737 air purifier (AADCO Instruments, Inc.) located at APL. Further details of the APL clean air system are described in Carter et al. (2005). NO_x, CO, and O_3 concentrations were measured by Teledyne gas analyzers (model 200E, 300E, and 400E, respectively).

With stringent certification standards for light duty gasoline vehicles (LDGV), gasoline vehicle emissions are becoming significantly lowered. In anticipation of low reactant concentrations, the chamber was characterized to ensure minimal background effects. A series of characterization runs as described in Carter et al. (2005) were conducted to check for NO_x off-gassing, and background VOCs. A summary of the characterization runs completed for MACh is available in Table 5-1. Humidity was monitored with a using a LI-COR® LI-840A CO_2/H_2O analyzer (down to 0.001%). Particle size and number were measured according to electrical mobility with a TSI Scanning Mobility Particle Sizer (SMPS) spectrometer consisting of a 3081L differential mobility analyzer, a 3080 electrostatic classifier 3080 that is equipped with a bi-polar krypton-85 charger and a butanol based 3776 condensation particle counter (CPC).

Particle loss rates are determined assuming first order wall loss kinetics as described in Cocker et al. (2001). By integrating the following equation,

$$\frac{dN(D_p,t)}{dt} = -\beta(D_p)N(D_p,t) \qquad (2)$$

the wall loss coefficient (β) is estimated according to the particle number concentrations (N) and the particle size (D_p) as a function of time for each individual experiment. Vapor wall losses are not considered in these experiments.

Table 5-1. Results of initial characterization runs

EXPERIMENT		DESCRIPTION
Reactor conditioning	Zero air + O_3 + OH radicals	Reactor walls "scrubbed" to remove any initial impurities
Background VOCs NO_x off gassing Radical sources	Zero air	Would observe background particle formation if walls are a radical source, if NOx is offgasing, or if VOCs are present in clean air
Background VOCs Radical sources	Zero air + NO + CO	Would observe O_3 formation if aerosol precursors (radical sources) come from walls or present in clean air. NO would react to form NO_2 in the presence of a radical, O_3 results from the photolysis of NO_2, and OH is consumed by CO.
NO_x off gassing	Zero air + CO	CO suppresses OH radical and SOA formation. If NO_X is off gasing would observe O_3 formation from photolysis of NO_2

During all tests the chamber was maintained under dry conditions (RH below detection limits) particle formation was less than 1 ug m^{-3} and NO_x concentrations were below detection limits. For the zero air, NO/CO, and CO runs less than 10, 50, 11 (6 hours) ppb of ozone were detected, respectively. Any particle formation is the result of NO_x or precursors such as HONO off-gassing from the chamber walls. The pure air may be a source as well, but is less likely.

5.4 Test vehicles and fuels

For this study, two low mileage 2015 light duty gasoline vehicles equipped with wall-guided GDI (WG-GDI) engines and three way catalysts were investigated. The first vehicle is a Honda Accord and the second a Hyundai Accent. Each vehicle was tested over the California Unified Cycles (UC) on commercially available E10 gasoline. The UC was

developed by the California Air Resources Board (CARB) to represent typical California driving conditions and includes higher average speeds and acceleration rates with fewer stop and less idling time compared to the standard Federal Test Procedure (FTP) certification cycle. It consists of a cold start phase, a stabilization phase, a ten minute hot soak, and a warm start phase (figure 5-2). Prior to the first UC, the vehicle was preconditioned with a LA4 drive cycle and prior to all UCs, the vehicle was cold soaked overnight for a minimum of 8 hours. Testing modern GDI engine with the aggressive driving conditions in the UC presents a unique emissions profile for atmospheric chamber studies.

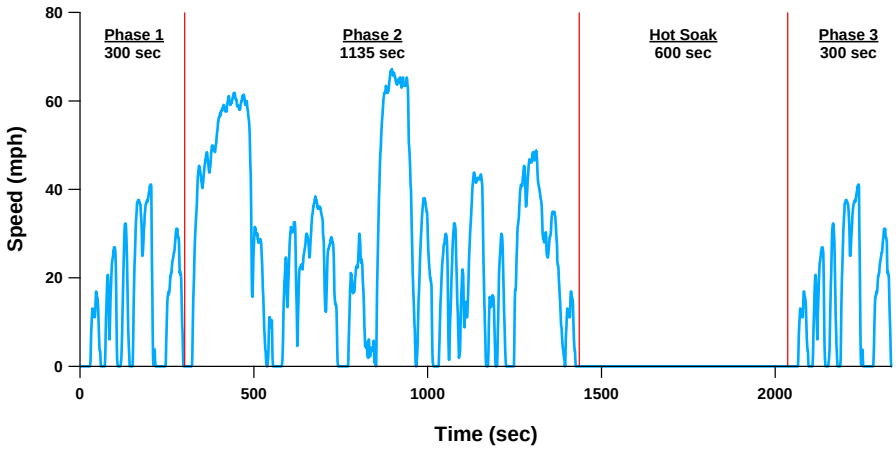

Figure 5-2. Unified Cycle

5.5 Emissions Testing and photochemical oxidation

A series of chassis dynamometer experiments were completed to investigate the aging of the vehicle emissions. Certification quality vehicle emissions testing was completed on a Burke E. Porter 48-inch single roller chassis dynamometer located in the CE-CERT vehicle emissions research laboratory (VERL). The chamber was positioned in the test cell

and was directly connected to a positive displacement pump constant volume sampling (CVS) system. Two ejector diluters built from single stage vacuum generators (Air-Vac TD11OH) operating in parallel were used to introduce the diluted emissions to MACh. A separate pure air generator was constructed for the injection system. Compressed air is passed through a general purpose particle filter, multiple silica gel columns (dewpoint below -40ºC), activated charcoal (heat conditioned to remove lower carbon compounds), purafil, and carulite canisters, a coalescing filter and then hepa filtered before passing through the injection system. The air had no detectable particles, NO_X, or non-methane hydrocarbons.

Prior to each emissions test, the chamber was injected with O_3 and irradiated with black lights for 2-3 hours and then continuously flushed overnight using the AADCO pure air system located at APL. The chamber was then filled to approximately a third of the volume with pure air and transported to VERL where the diluted exhaust was cumulatively collected over phases 1, 2 and 3 of the Unified Cycle, thereby representing trip average emissions. Upon completion the chamber is transported back to APL and the remainder of the chamber is filled with pure air until the chamber reaches a pressure 0.05 inH_2O. The overall dilution from tailpipe to chamber was ~114:1 and 60:1 for the Hyundai Accent and the Honda Accord, respectively. 70 ppb of H_2O_2 was injected as an OH radical source and PFH was injected to track bag dilution. The NO_X to VOC ratios were not adjusted. The exhaust was then photochemically aged for 12 hours. During the tests, the temperature was maintained at ~25to 30°C. The experimental setup is shown in Figure 5-3. The relative humidity in the chamber for the Hyundai and Honda was 3% and 6%, respectively.

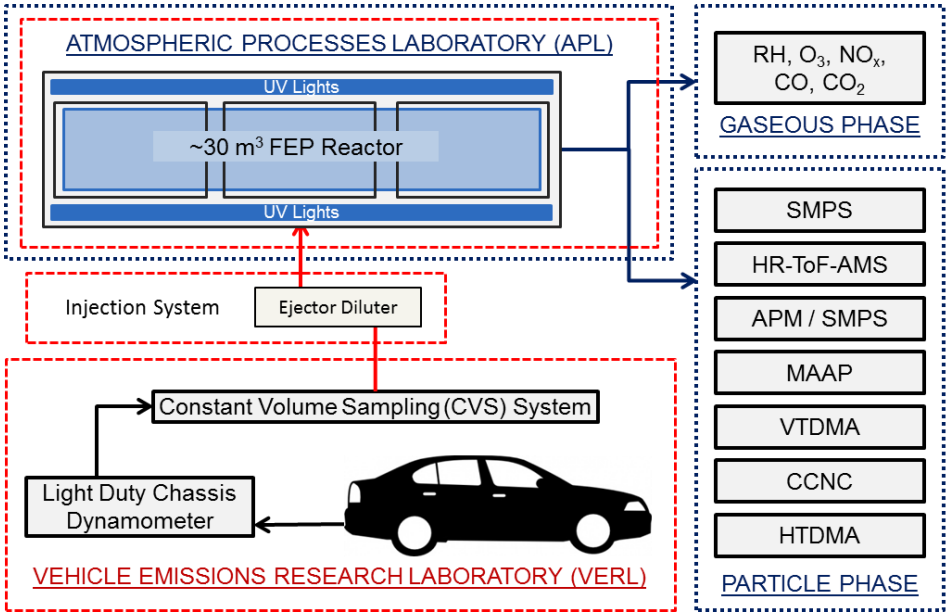

Figure 5-3. Experimental Setup

5.6 Additional Instrumentation and Analysis

The concentration of black carbon was measured with a ThermoScientific Multi-Angle Absorption Photometer (MAAP) which utilizes an aerosol-filter based system and a 670 nm light source to detect the black carbon mass loading (Petzold et al., 2002). To provide a more accurate total mass, and to provide an indication of the composition, effective density measurements for the vehicles were determined by selecting the peak sizes in the distribution. The particle effective density was measured by operating a Kanomax particle mass analyzer (APM) in series with an SMPS (Malloy et al., 2009). The APM was programmed to detect the particle mass according to a user selected diameter to determine the effective density. The diameter was selected according to the peak mode diameters obtained from the SMPS. The volatility was measured with a volatility tandem DMA (VTDMA). The thermodenuder was operated at 50°C. The volume fraction remaining is

determined based on the volume ratio of the aerosol after passing through the thermodenuder and before. Both the APM and the VTDMA were size selected according to the mobility diameter.

The non-refractory bulk chemical composition, relative mass, and size was measured with an Aerodyne high-resolution time-of-flight aerosol mass spectrometer (HR-ToF-AMS) (DeCarlo et al., 2006). The HR-ToF-AMS was alternated between the mass spectrum W-mode and the particle ToF V-mode. The data from W-mode was used to characterize the chemical composition, while the V-mode was used to provide information regards to the size and relative concentration of the bulk composition.

CCN activity is measured with a Droplet Measurement Technologies, Inc. single growth column continuous-flow thermal gradient diffusion column CCN Counter (CCNC) (Lance et al., 2006, Roberts and Nenes, 2005). Aerosols with a critical supersaturation greater than the column supersaturation activate. The droplets are then counted with an optical particle counter at the exit of the column. The CCN activation curves are obtained by either operating the CCNC-SMPS in scanning mobility analysis mode (SMCA) which scans the DMA voltage to obtain CCN active aerosol fractions for each size for the full size distribution or by selecting a single size and scanning through multiple column supersaturations.

To determine the total PM mass, a unit density can be assumed, or a density derived from the chemical composition measured by an AMS (e.g. density of ~1.4 g cm^{-3} for SOA and 1.72 g cm^{-3} for ammonium nitrate) can be applied to volume data. However, for experiments where there is a large contribution of fractal soot particles, these methods can

lead to an over estimation of PM (Nakao et al., 2011). For this study, effective density measurements from the APM-SMPS were applied to volume data from the SMPS to account for the varying density and determine the total PM mass. In addition, for experiments where the total non-refractory mass measured by the AMS and the BC mass measured by the MAAP did not agree with the total mass derived from the SMPS, a scaling factor, AMS_{sf}, as described by May et al., (2014) is applied (eqn. 2). The difference in mass is assumed to have the same chemical composition as that identified by the AMS.

$$AMS_{sf} = \frac{C_{SMPS} - C_{BC}}{C_{ORG} + C_{SO_4} + C_{NO_3} + C_{NH_4}} \qquad (2)$$

For this study, a single hygroscopicity parameter, κ, relating the aerosol dry diameter (D_d) and critical saturation (S_c) were used to describe the aerosol water uptake properties (eqn. 3) (Petters and Kreidenweis, 2007; Köhler, 1936).

$$\kappa = \frac{4A^3}{27D_d^3 ln^2 S_c}, \quad where\ A = \frac{4\sigma_{s/a} M_w}{RT\rho_w} \qquad (4)$$

R is the universal gas constant, T is the temperature, $\sigma_{s/a}$ is the droplet interfacial surface tension, and M_w and ρ_w are the molecular weight and density of water, respectively. The critical supersaturation is defined by $SS = S_c - 1$. This can be used to determine κ for the supersaturated regime. For the subsaturated regime, κ was determined using the growth factor (Petter and Kredenweis 2007).

$$\frac{\kappa}{gf^3 - 1} = \frac{100}{RH} exp\left(\frac{A}{D_d gf}\right) - 1 \qquad (5)$$

For the hygroscopicity calculations, particles are assumed to be spherical.

5.7 Results and discussion

Photochemical oxidation was initiated at time 0 and continued over the course of 12 hours. Significant secondary aerosol formation consisting of SOA and ammonium nitrate occurred within the first hour and peaked approximately 2-3 hours into photo chemical aging. The NO is oxidized to NO_2 during the first hour for the Honda, and second for the Hyundai (Figure C1 and C2). The experiments were wall loss corrected to quantify the secondary aerosol produced in the chamber. The estimated wall loss rates for the Hyundai and the Honda Accord were 0.12 hr^{-1} and 0.13 hr^{-1}, respectively. These wall loss rates are comparable to other chambers of similar size (Wang et al., 2014; Cocker at al., 2002).

As shown in Table 5-2 and figure 5-3, the final mass significantly exceeds that of the initial mass with a SA:POA of 19.6 and 31.1 for the Hyundai and the Honda, respectively. This indicates LDGV to be a large source of secondary aerosol precursors. However, it is important to note that initial particle concentrations could be higher; the SMPS has a cutoff point of 14nm, so particles <14nm are not accounted for, and approximately 10% the volume was lost while transporting MACh from VERL to APL. Thus, the SA:POA ratios may be overestimated.

The cold start phase may be the largest contributor to the secondary PM because particle and gaseous emissions are typically the highest during cold start driving conditions when the least efficient combustion occurs and the oxidation efficiency of the TWC is low. Elevated THC and PM concentrations during the cold portion of the UC cycle have been observed (Karavalakis et al., 2014). Beyond the cold start, the emissions were then the

highest during accelerations and decelerations (Karjalainen et al., 2015). Measuring the SOA forming potential in real time using a potential aerosol mass (PAM) reactor system, Karjalainen et al. (2015) who also investigated a GDI vehicle, observed the highest secondary PM emissions occur from the cold start portion of their drive cycle.

Table 5-2. Summary of POA/SOA. SOA was taken from the peak conc.

Vehicle	POA (ug m^{-3})	SOA (ug m^{-3})	SOA/POA
Hyundai	7.1	138.7	19.6
Honda	1.3	41.4	31.1

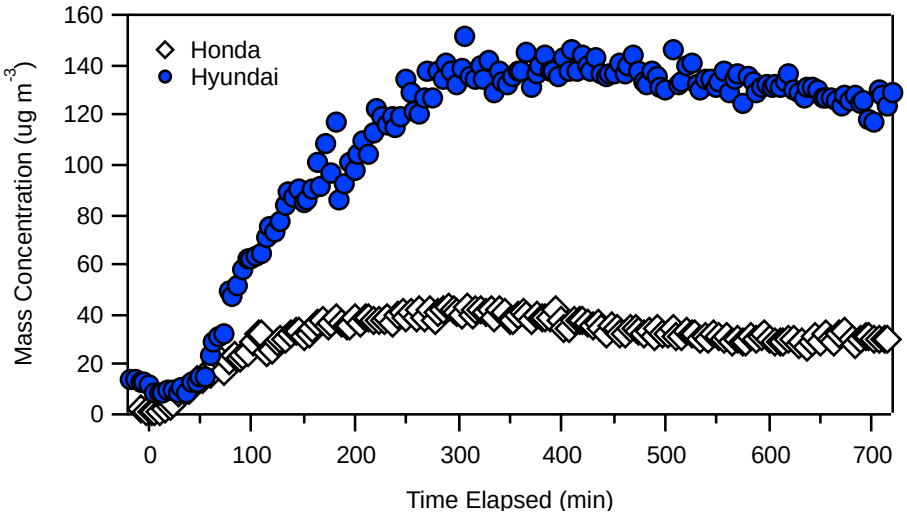

Figure 5-4. Measured concentrations as function of time elapsed after lights on

The initial POA was higher for the Hyundai than the Honda, which may play a role in secondary aerosol formation by acting as a surface for oxidized compounds to condense onto thereby effecting the overall size distribution of the secondary aerosol. As shown in the aerosol size distributions in figure 5-5, for the Hyundai Accent and Honda Accord, the initial unimodal distribution splits to form a trimodal and bimodal distribution,

respectively. In addition, particle growth is observed and indicates condensation of organic or inorganic vapors and separate nucleation events.

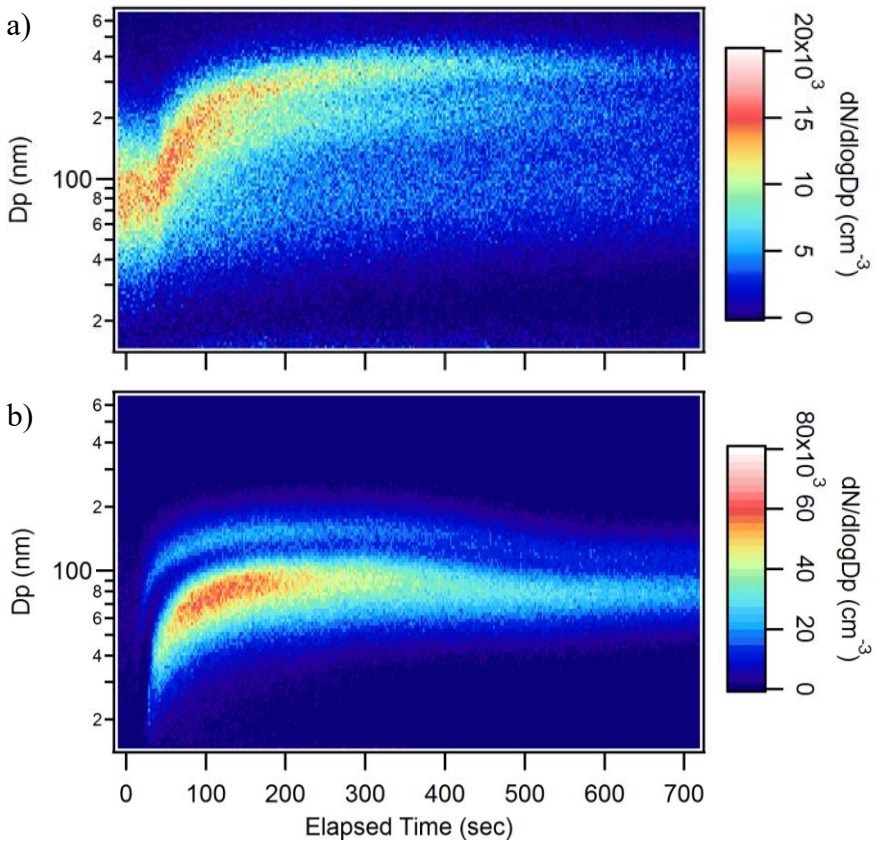

Figure 5-5. Size distributions during course of experiment. A) Hyundai Accent B) Honda Accord

Mass fractions of the non-refractory aerosol composition is presented in figure 5-5 and are not wall loss corrected. For both vehicles, the fresh aerosols (time 0) are a mixture of black carbon, organic and inorganic compounds. However, the chemical changes at the onset of photochemical oxidation is apparent with the modification in the mass fractions of BC, organics, and inorganic nitrates. For both vehicles, the secondary PM is dominated by inorganic nitrates with less organics at the onset of secondary PM formation (figure 5-6).

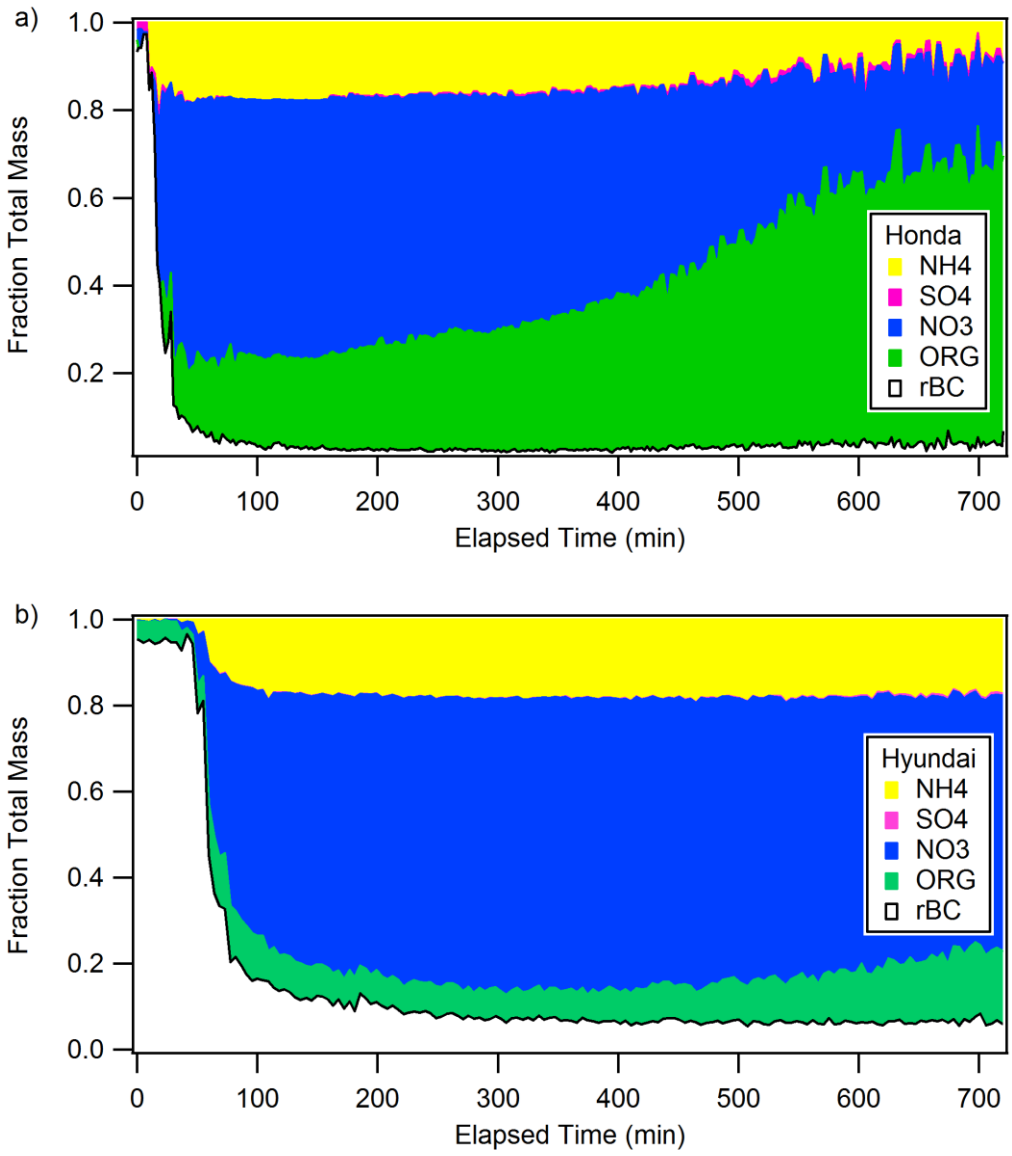

Figure 5-6. Mass fractions of the aerosol measured by the AMS for a) Honda Accord and b) Hyundai Accent. Data are not wall loss corrected.

Although ammonia measurements are not available, it is presumed that ammonium formation occurs as a byproduct when reducing NO in the TWC; this has been correlated with fuel rich conditions associated with accelerations (Karjalainen et al, 2015). Nitric acid formed from the oxidation of NO_x can then react with ammonia to form the inorganic

nitrates in the chamber. This is consistent with May et al., (2014) who reported high inorganic nitrates formation for a small number of vehicles in their study. For the Honda Accord, the organic fraction represents approximately 20% of the overall of the secondary aerosol five hours into photochemical aging and continues to increase for the course of the experiment. For the first 8 hours the inorganic mass fraction appears stable, but the organic fraction continues to increase, which indicates that the SOA is still forming. Beyond 8 hours, the sharp decrease in inorganic salt fraction indicates evaporation and is consistent with the overall decrease in mass. Unlike the Accord, the organic fraction for the Hyundai Accent is a modest 10% five hours in and then continues to gradually increase.

The effective density measurements for both vehicles are presented in figure 5-7. For the Hyundai Accent, two density modes are observed and indicate fractal particles for the smaller particles ($\rho_{eff} < 1 g\ cm^{-3}$) and an inorganic secondary aerosol with a density that is consistent with ammonium nitrate ($\rho = 1.72 g\ cm^{-3}$) for the larger sizes. Although the fractal particles and the inorganic nitrates appear to dominate the two modes, the increase in the initial ρ_{eff} and then the slight increase and decrease in ρ_{eff} for the larger and smaller sizeds mode indicates a certain degree of internal mixing with organics. Unlike the Hyundai, the Honda Accord has a single density that is close to that of NH_4NO_3 which may indicate a distribution that is dominated by a large internally mixed population.

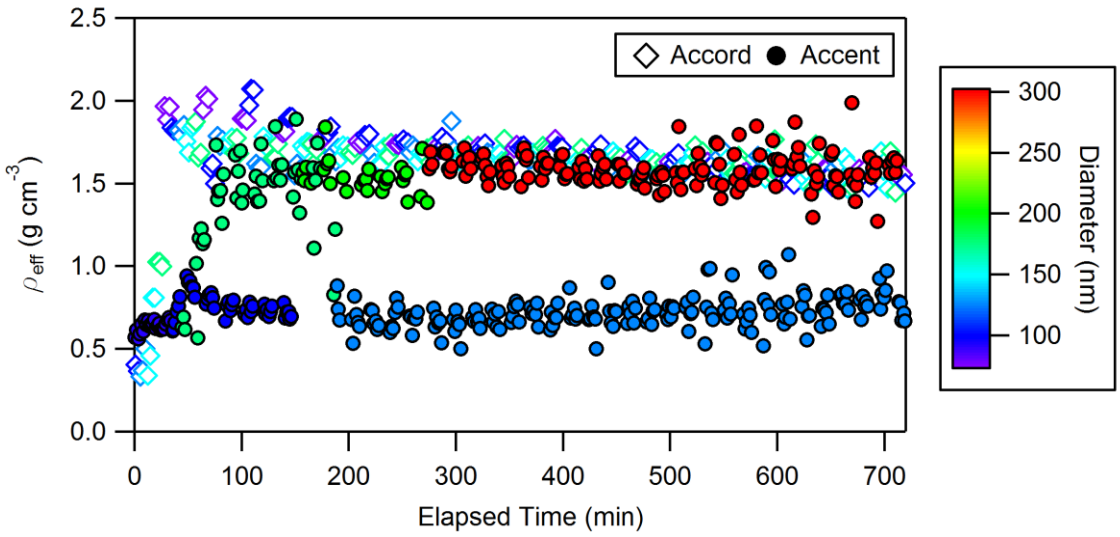

Figure 5-7. Effective density measurements for vehicle 1 and 2.

The Van Krevelen plot can be used to describe the chemical evolution of the total organic aerosol composition where the slope provides an indication of the oxidation pathway (Heald et al., 2010). As seen in figure 5-8, the O:C ratio >1 indicates the formation of a highly oxidized low volatile organic aerosol for the Hyundai. This high O:C has not been previously seen in other work. However, for the Honda Accord, the O:C ratio of ~ 0.85 was observed which is higher than the O:C observed by Platt et al., (2013) (O:C ~0.7) for a Euro 5 car and Karjalainen et al, (2015) (O:C 0.5-0.6). Platt et al., (2013) suggests that the highly oxidized aerosol are a result of smaller unspeciated prescursor hydrocarbons. Nordin et al., (2013) observed an O:C~0.4 for aged emissions from warm idling Euro 2-4 vehicles, and attributed 60% of of the SOA to C6-C9 light aromatic compounds.

Although the organic fraction represents only a modest amount of the overall secondary aerosol, the VOC profile present in these vehicle emissions are unique in that they produced highly oxidized SOA. It is also important to note that during the UC cycle there is a large number of accelerations and decelerations, so the more oxidized SOA may be the result of more aggressive driving conditions. Using a potential aerosol mass (PAM) reactor and oxidant concentrations 100-100 times higher, Karjalainen et al., (2015) observed real time measurements of the secondary particulate during a new European drive cycle (NEDC) for a 2011 GDI vehicle. The highest secondary emissions were observed to originate from gaseous precursors present in the cold start portion of the NEDC where the secondary emissions were dominated by organics from the cold start. Gordin et al., (2014) also observed higher SOA formation for vehicles tested over cold start conditions compared to warm start tests.

For the Honda Accord, the shallow slope in the Van Krevelen plot indicates the SOA formation pathways through the formation of acetaldehyde (oxidized VOCs) and thus, addition of carboxylic acid or the addition of an alcohol and carbonyl but also may indicate that alcohol or peroxide group may be occurring in addition to the acid addition (Sally Ng., 2011). The increase in O:C is consistent with the increase in *m/z* 44 (figure 5-9), which indicates that acids play a role in the oxidation of the vehicle OA. These slopes are similar to those reported by Presto et al., (2014), for the photochemical oxidation of emissions for a LEV-1 and LEV-2 gasoline vehicles. The more shallow slope of the Hyundai suggest that oxidation pathways may occur through alcohol or peroxide addition.

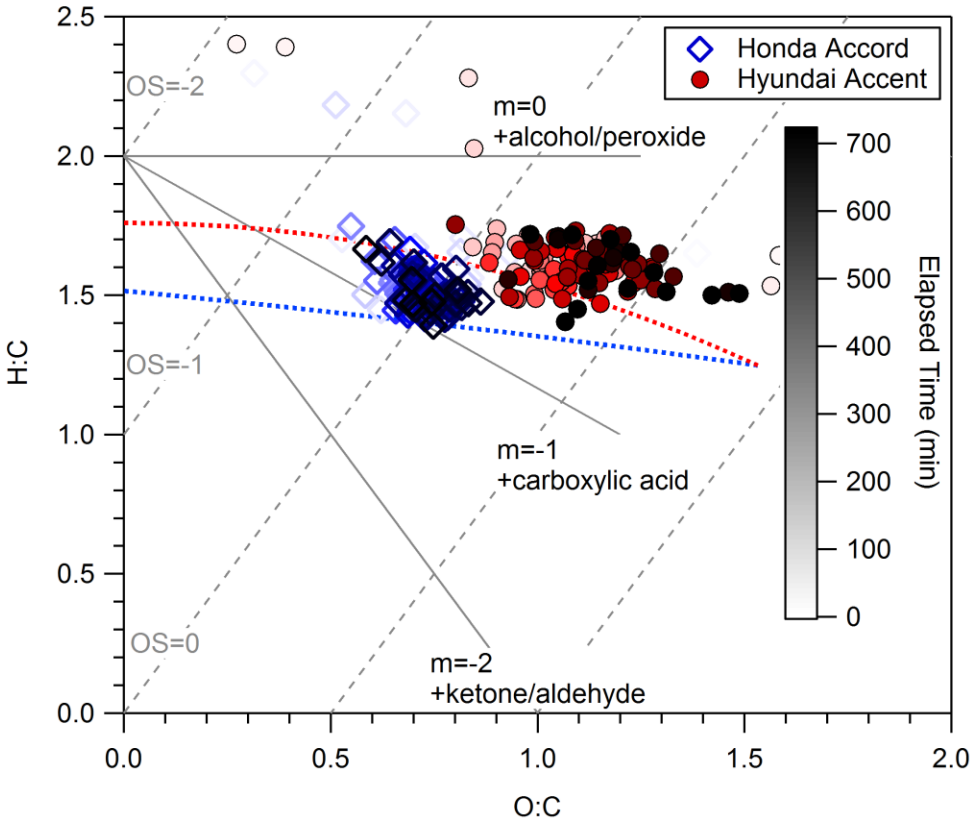

Figure 5-8. Van Krevelen plot for Honda Accord and Hyundai Accent

m/z 44 (CO_2^+) is a marker of OA oxidation and the fragment ion *m/z* 43 can be used to represent semi-volatile SOA which is associated with fresh SOA ($C_2H_3O^+$) (Canagaratna et al., 2007; Kroll et al., 2009). For both vehicles, *m/z* 44 increases as the aerosol is photochemically aged, this suggests that with increasing OA oxidation, acid formation occurs. (Duplissey et al., 2011; Ng. et al., 2011). For both vehicles, the variability in the oxidation levels is apparent with the level of scattering. However, as the emissions continue to age, the data converges into a relatively tight cluster in the *f*44 vs. *f*43 plot which suggests chemical similarity towards the end of each experiment with *f*44

dominating. It also shows that they fall within the boundaries for ambient oxidized OA (Ng et al., 2010); the Honda more so than the hyundai.

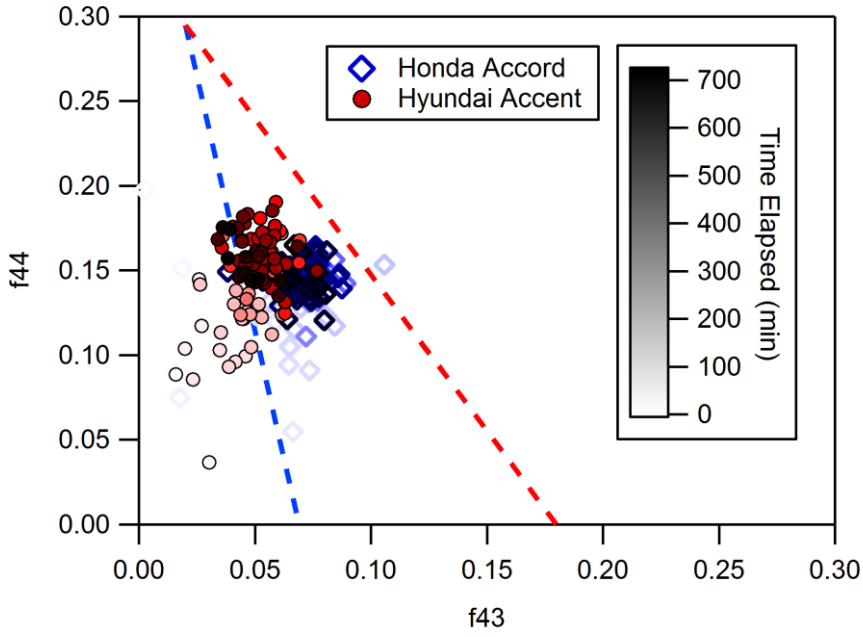

Figure 5-9. Triangle plots for the Hyundai Accent and the Honda Accord.

HR mass spectra data of the aerosol the beginning of the experiment (0 hours) and the aged aerosol after 10 hours is presented in figures C-3 and C-4 for the Honda and Hyundai, respectively. After 10 hours of aging, *f*44 (CO_2^+) is the most abundant peak for the Honda, which are consistent with significant levels of oxidation (low volatile oxygenated organic aerosols). For the Hyundai *f*29 (CHO) and *f*44 are the most abundant.

The VFR for the Honda is presented in figure 5-10. VFR for Hyundai is not available. The aerosols formed at the beginning of the experiment are highly volatile. This can be due to the significant amount of secondary nitrate formation, which has a higher vapor pressure and can evaporate at elevated temperatures.

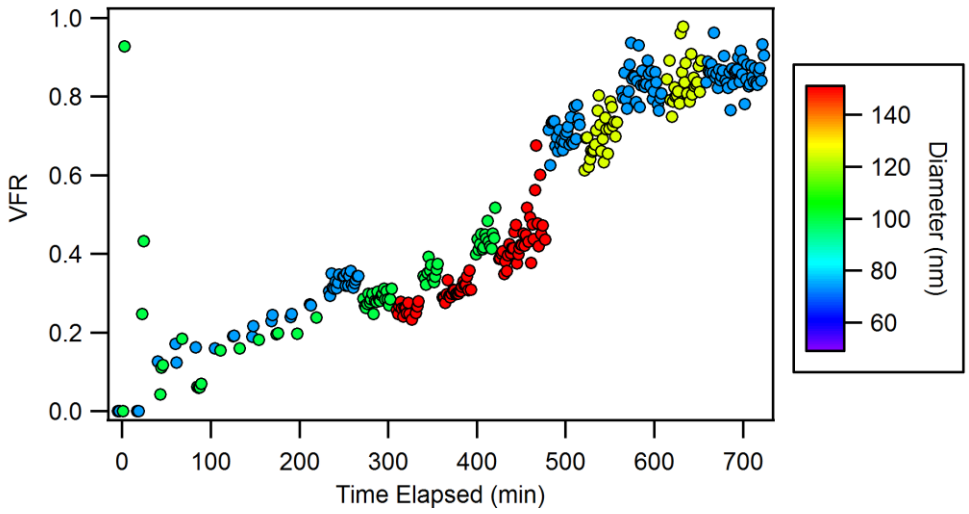

Figure 5-10. VFR data for Honda Accord.

The photochemical oxidation and subsequent nitrate formation and hydrophilic organic compounds of vehicle exhaust resulted in various levels of aerosol hygroscopicity. At time zero, there is no measured CCN activity and is attributed to water insoluble combustion aerosol that is soot dominated. However, the CCN activity increases for both vehicles with the formation of hydrophilic oxidation products and inorganic nitrates. The CCN activity of the Accord lowered with decreasing aerosol volatility, and increase in organic mass fractions. Also, fractal material is present during the course of the experiment, which can also effect the measured hygrosocopicity. Overall, for both vehicles, the apparent hygroscopicity derived from the subsaturated measurements were lower than those measured in the supersataurated regime. The κ_{GF} from the beginning to the end of the experiment for the Accord and the Accent ranged from 0.06 to 0 and 0 to 0.03, respectively. They follow the same general trend in the supersaturated regime where κ_{CCN}

decreases and increases for the Honda and Hyundai, respectively. The subsaturated conditions in the HTDMA may not provide the required amount of water vapor to fully dissolve the aerosols, thereby limiting their ability to reach their deliquescence point. Also, GF values of <1 were observed which indicates restructuring during the hydration process in the HTDMA.

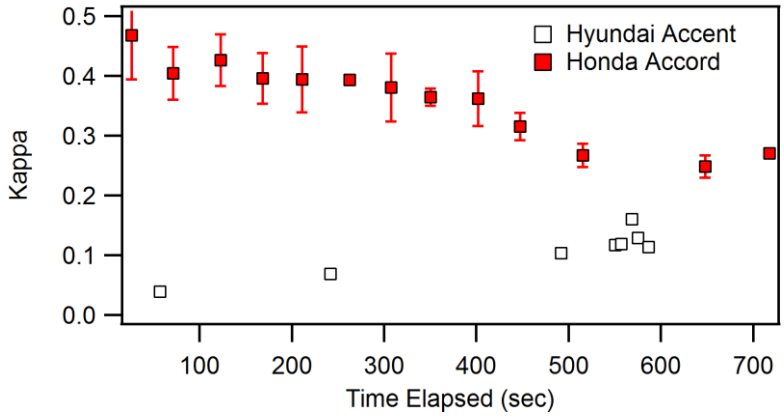

Figure 5-11. Kappa measure by the DMT CCNC for the Honda Accord and the Hyundai Accent. For the Accord, the CCNC was measured using SMCA. The Accent was measured using scanning SS mode while keeping a selected size constant.

For the supersaturated regime, the Honda Accord displayed a higher apparent hygroscopicity and appears to be more CCN active than the Hyundai Accent (Figure 5-11). However, it is important to note that previous studies have observed evaporation artefacts for inorganic salts in the both the CCNC and the HTDMA (Romakkaniemi et al., 2014; Tang et al., 2014; Hu et al., 2011). NH_4NO_3 has a high vapor pressure and can partition into the gas phase at the elevated temperatures seen during standard CCNC and HTDMA operating conditions.

With NH_4NO_3 having a measured κ_{CCN} of 0.74 (Tang et al., 2014), the large fraction of inorganics salts observed in the chamber should be apparent in the CCN measurements. Using a DMT CCNC, Tang et al. (2014) observed changes in CCN activity of NH_4NO_3 for temperatures greater than 21C and under longer CCNC resident times and Romakkaniemi et al. (2014) observed changes for SS between 0.1% and 0.7% under standard operating conditions. This loss of water soluble inorganic salts can lead to smaller aerosol diameters and, thereby leading to the underestimation of CCN activity (Romakkaniemi et al., 2014; Tang et al., 2014). Because of these evaporation artifacts, the hygroscopcity measurements here may be underestimating the CCN activity of the aerosols. The effect of different column temperatures is apparent for the Accord; the κ_{CCN} at the lower SS (0.21, .51%) were higher than those measured at the higher SS (0.79) for the first 6 hours of the experiment. For the remainder of the experiment, lower κ_{CCN} values were observed for the lower SS.

5.8 Conclusion

The design of MACh has allowed for the integration of VERL with the the higly advanced physical and chemical characterization capabilities available at APL. MACh was characterized and demonstrated to be a vital means of investigating mobile combustion sources. Using MACh, the effect of photochemical aging on vehicles emissions for two current generation GDI vehicles where characterized. Atmospheric aging occurred at the onset of UV radiation, where secondary PM formation from modern gasoline direct injection vehicles greatly exceeded the primary emissions in both mass and number and

produced highly oxidized SOA, where O:C ratios where higher than observed in previous studies. However, depending on the vehicle, the chemical composition can be non-uniform across sizes which was apparent in the effective density and volatility data. In addition, the hygrosocopicity was enhanced with aging. “Fresh” diluted vehicle exhaust does not activate as it is mostly composed of insoluble materials such as soot. Physiochemical changes of primary emissions with photochemical oxidation was shown to modify aerosol water uptake properties. However, the apparent hygrosocopicity may not reflect the true water uptake properties; hygrosocopicity analysis is challenging in the presence of fractal particles, complex aerosol mixtures, and varying compositions across aerosol sizes.

5.9 Acknowledgements

Vehicle testing in this study was supported by the Southern California Air Quality Management District. Aerosol hydroscopicity work was supported by the National Science Foundation Award (NSF 1151893). D. Vu would like to acknowledge funding support from the U.S. Environemtnal Portection Agency STAR Fellowship (FP-91751101). The authors would like to thank Kurt Bumiller for aiding in the design of the chamber, and Mark Villela for the technical contribution in conducting the emissions testing.

5.10 References

Bahreini, R., et al. (2012), Gasoline emissions dominate over diesel in formation of secondary organic aerosol mass, Geo- phys. Res. Lett., 39, L06805, doi:10.1029/2011GL050718.

CARB, 2010. Preliminary Discussion Paper - Proposed Amendments to California's Low-emission Vehicle Regulations - Particulate Matter Mass, Ultra fine Solid Particle Number, and Black Carbon Emissions. California Air Resources Board, Sacramento, CA. 11 May.

Carter, W. P. L., Luo, D., Malkina, I. L., and Pierce, J. A.; Environmental chamber studies of atmospheric reactivities of volatile organic compounds. Effects of varying chamber and light source; Final report to National Renewable Energy Laboratory; 1995.

Carter, W. P. L., Cocker, D. R. III, Fitz, D. R., Malkina, I. L., Bumiller, K., Sauer, C. G., Pisano, J. T., Bufalino, C., and Song, C. (2005). A new environmental chamber for evaluation of gas-phase chemical mechanisms and secondary aerosol formation, Atmos. Environ., 39:7768–7788, doi:10.1016/j.atmosenv.2005.08.040.

Cocker, D. R., Flagan, R. C., Seinfeld, J. H.: State-of-the-art chamber facility for studying atmospheric aerosol chemistry. Environ. Sci. Technol., 35, 2594−2601, 2001.

DeCarlo, P.F., Kimmel, J.R., Trimborn, A., Northway, M.J., Jayne, J.T., Aiken, A.C., Gonin, M., Fuhrer, K., Horvath, T., Docherty, K.S., Worsnop, D.R., and, and Jimenez, J.L. (2006), Field-Deployable, High-Resolution, Time-of-Flight Aerosol Mass Spectrometer, *Analytical Chemistry* 2006 *78* (24), 8281-8289. DOI: 10.1021/ac061249n.

Gordon, T. D., Presto, A. A., May, A. A., Nguyen, N. T., Lipsky, E. M., Donahue, N. M., Gutierrez, A., Zhang, M., Maddox, C., Rieger, P., Chattopadhyay, S., Maldonado, H., Maricq, M. M., and Robinson, A. L.: Secondary organic aerosol formation exceeds primary particulate matter emissions for light-duty gasoline vehicles, Atmos. Chem. Phys., 14, 4661-4678, doi:10.5194/acp-14-4661-2014, 2014.

Karavalakis, G., Short, D., Vu, D., Villela, M., Asa-Awuku, A., and Durbin, T. (2014). Evaluating the Regulated Emissions, Air Toxics, Ultrafine Particles, and Black Carbon from SI-PFI and SI-DI Vehicles Operating on Different Ethanol and Iso-Butanol Blends. Fuel, 128:410–21.

Karjalainen, P., Pirjola, L., Heikkilä, J., Lähde, T., Tzamkiozis, T., Ntziachristos, L., Keskinen, J., and Rönkkö, T.: Exhaust particles of modern gasoline vehicles: a laboratory and an on-road study, Atmos. Environ., 97, 262–270, doi:10.1016/j.atmosenv.2014.08.025, 2014.

Karjalainen, P., Timonen, H., Saukko, E., Kuuluvainen, H., Saarikoski, S., Aakko-Saksa, P., Murtonen, T., Dal Maso, M., Ahlberg, E., Svenningsson, B., Brune, W. H., Hillamo, R., Keskinen, J., and Rönkkö, T.: Time-resolved characterization of primary and secondary particle emissions of a modern gasoline passenger car, Atmos. Chem. Phys. Discuss., 15, 33253-33282, doi:10.5194/acpd-15-33253-2015, 2015.

Köhler, H. (1936). The nucleus in and the growth of hygroscopic droplets, Trans. Farad. Soc., 32:1152-1161.

Lance, S., Medina, J., Smith, J. N., and Nenes, A. (2006). Mapping the Operation of the DMT Continuous Flow CCN Counter. Aeros. Sci. Tech., 40:242–254.

Leskinen, A., Yli-Pirilä, P., Kuuspalo, K., Sippula, O., Jalava, P., Hirvonen, M.-R., Jokiniemi, J., Virtanen, A., Komppula, M., and Lehtinen, K. E. J. (2015). Characterization and testing of a new environmental chamber, Atmos. Meas. Tech., 8:2267-2278, doi:10.5194/amt-8-2267-2015.

Liang B., Ge Y., Tan J., Han X., Gao L., Hao L., Ye W., Dai P. (2013). Comparison of PM emissions from a gasoline direct injected (GDI) vehicle and a port fuel injected (PFI) vehicle measured by electrical low pressure impactor (ELPI) with two fuels: Gasoline and M15 methanol gasoline. Journal of Aerosol Science, 57, 22-31.

Liu, T., Wang, X., Deng, W., Hu, Q., Ding, X., Zhang, Y., He, Q., Zhang, Z., Lü, S., Bi, X., Chen, J., and Yu, J. (2015). Secondary organic aerosol formation from photochemical aging of light-duty gasoline vehicle exhausts in a smog chamber, Atmos. Chem. Phys., 15:9049-9062, doi:10.5194/acpd-15-10553-2015.

Malloy, Q., Nakao, S., Qi, L., Austin, R. L., Stothers, C., Hagino, H., and Cocker, D. R. (2009). Real-Time Aerosol Density Determination Utiliz- ing a Modified Scanning Mobility Particle Sizer—Aerosol Particle Mass Analyzer system. Aerosol Sci. Technol., 43:673–678.

Nordin, E. Z., Eriksson, A. C., Roldin, P., Nilsson, P. T., Carlsson, J. E., Kajos, M. K., Hellén, H., Wittbom, C., Rissler, J., Löndahl, J., Swietlicki, E., Svenningsson, B., Bohgard, M., Kulmala, M., Hallquist, M., and Pagels, J. H.: Secondary organic aerosol for- mation from idling gasoline passenger vehicle emissions investi gated in a smog chamber, Atmos. Chem. Phys., 13, 6101–6116, doi:10.5194/acp-13-6101-2013, 2013.

Petters, M. D. and Kreidenweis, S. M. (2007). A single parameter representation of hygroscopic growth and cloud condensation nucleus activity, Atmos. Chem. Phys. 7:1961-1971, doi:10.5194/acp-7-1961-2007.

Petzold A, Kramer H, and Schönlinner M, Continuous Measurement of Atmospheric Black Carbon Using a Multi-angle Absorption Photometer. Environmental Science and Pollution Research, Special Issue 4, 78-82, 2002.

Platt, S. M., El Haddad, I., Zardini, A. A., Clairotte, M., Astorga, C., Wolf, R., Slowik, J. G., Temime-Roussel, B., Marchand, N., Ježek, I., Drinovec, L., Močnik, G., Möhler, O., Richter, R., Barmet, P., Bianchi, F., Baltensperger, U., and Prévôt, A. S. H. (2013). Secondary organic aerosol formation from gasoline vehicle emissions in a new mobile environmental reaction chamber, Atmos. Chem. Phys., 13:9141-9158, doi:10.5194/acp-13-9141-2013.

Presto, A. A., Gordon, T. D., and Robinson, A. L.: Primary to secondary organic aerosol: evolution of organic emissions from mobile combustion sources, Atmos. Chem. Phys., 14, 5015-5036, doi:10.5194/acpd-14-5015-2014, 2014.

Roberts, G. C., and Nenes, A. (2005). A Continuous-Flow Streamwise Thermal-Gradient CCN Chamber for Atmospheric Measurements. Aer. Sci. Tech., 39:206–221, doi: 10.1080/027868290913988.

Romakkaniemi, S., Jaatinen, A., Laaksonen, A., Nenes, A., and Raatikainen, T. (2014) Ammonium nitrate evaporation and nitric acid condensation in DMT CCN counters, Atmospheric Measurement Techniques, 7(5), 1377-1384.

Seinfeld, J. H. and Pandis, S. N. (2008). Atmospheric Chemistry and Physics: from air pollution to climate change, John Wiley & Sons, INC.

Van Krevelen, D. W.: Graphical-statistical method for the study of structure and reaction processes of coal, Fuel, 24, 269–284, 1950.

Wang, X., Liu, T., Bernard, F., Ding, X., Wen, S., Zhang, Y., Zhang, Z., He, Q., Lü, S., Chen, J., Saunders, S., and Yu, J.: Design and characterization of a smog chamber for studying gas-phase chemical mechanisms and aerosol formation, Atmos. Meas. Tech., 7, 301-313, doi:10.5194/amt-7-301-2014, 2014.

Chapter 6 - Aged Gasoline Vehicle Emissions. Part II

6.1 Introduction

Emissions can vary from vehicle to vehicle, which can provide unique SOA precursor profiles. To gain a comprehensive understanding of the secondary aerosol from modern gasoline direct injection (GDI) vehicles, part II extends on the work presented in Part 1 (Chapter 5) by investigating the effect of photochemical aging for the emissions of two additional low accumulated mileage (<10,000miles) 2015 wall guided GDI vehicles; a Kia Soul and a Chevy Impala. Both vehicles followed the same testing protocol for the vehicles outlined in chapter 5. Each vehicle was testing over triplicate California Unified Cycles (UC) while operating on commercially available E10 gasoline. The dilution ratios for the Impala were 59:1 (UC1), 45:1 (UC2), and 43:1 (UC3). The dilution ratios for the Soul were consistent for all three; ranging from 68:1 to 70:1.

6.2 Results

While transporting the Mobile Atmospheric Chamber (MACh) from VERL to APL, the humidity stayed within 1% of the measured RH before and after transporting. All experiments were conducted under dry conditions where the relative humidity in the chamber was less than 7%. For both vehicles, emissions from UC1 and UC2 were each aged for approximately 8 hours, and UC3 was aged for 10 hours or until the chamber reached the end of its lifetime. For each vehicle, the results of the triplicate UC cycles were similar.

6.2.1 Gas and Particle Phase Characterization

For both vehicles, NO converted to NO_2 within the first hour after turning on the lights (Figures D-1 to D-4). For the Chevy Impala, the SOA was 2.6 times as high as the primary aerosol (Figure 6-1 and Table 6-1). However, for the Kia Soul, the secondary emissions significantly increased and continued to increase for the first five hours. The secondary PM was 8.9 times as high as the primary. These ratios are somewhat lower than those seen in Part I.

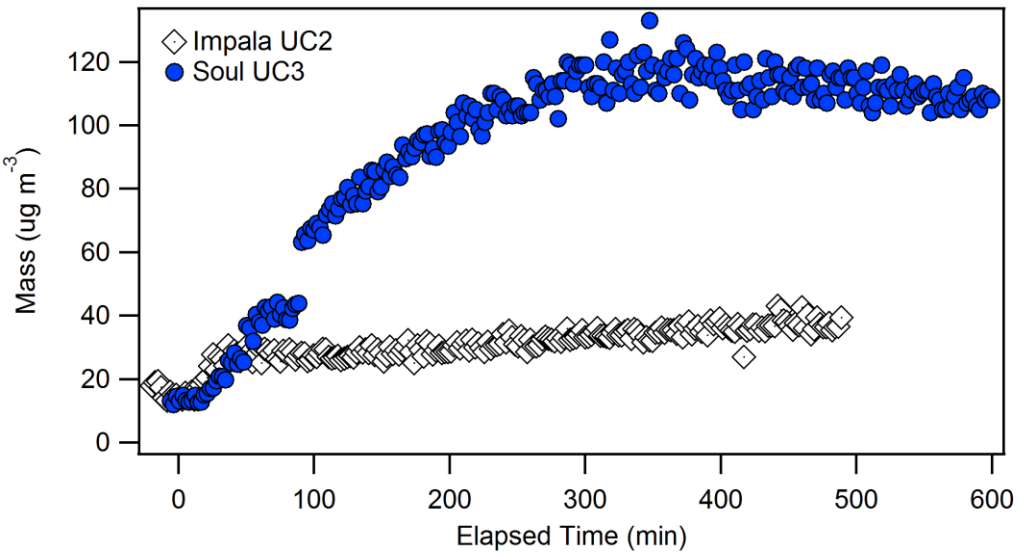

Figure 6-1. Mass concentrations during photo oxidation of vehicle exhaust

Table 6-1. Summary of POA/SOA. SOA was taken from the peak conc.

Vehicle	POA (ug m^{-3})	SOA (ug m^{-3})	SOA/POA
Soul	13.1	116.6	8.9
Impala	14.4	37.1	2.6

For the Kia Soul, initial unimodal distribution split to form a trimodal distribution that grows in size; this indicates condensation and separate nucleation events (figure 6-2). This is consistent with the two vehicles presented in chapter 5. However, for the Chevy Impala,

unimodal number size concentrations are observed over the entire course of the experiment which were consistent for all three UCs.

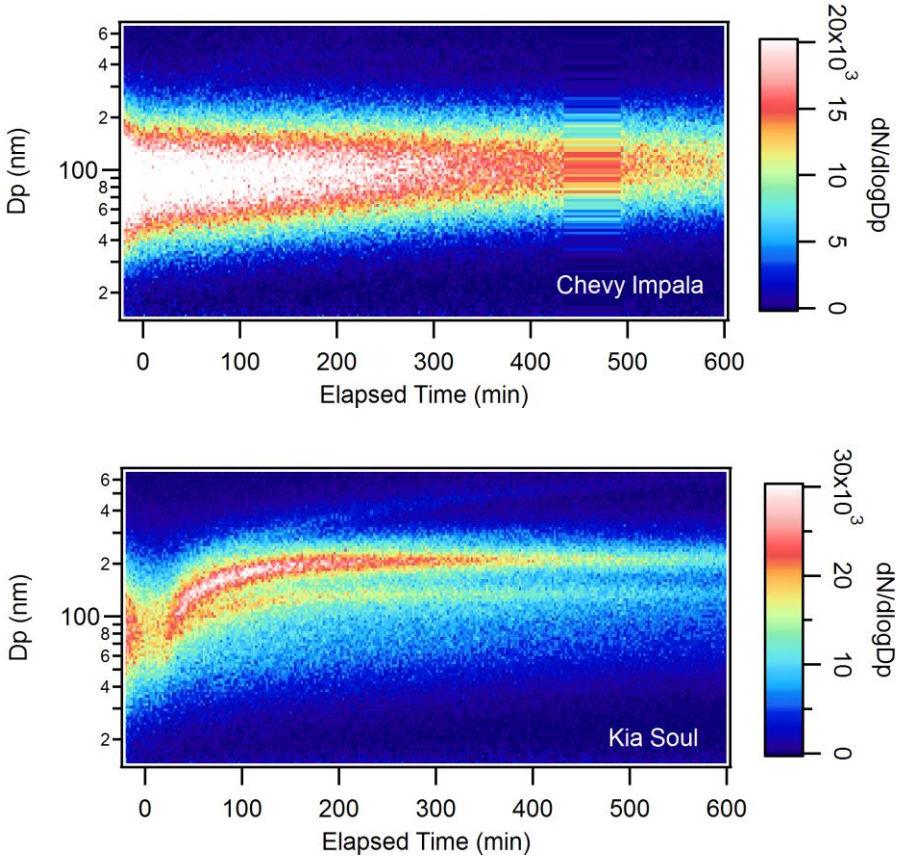

Figure 6-2. Time series of particle size number concentrations during the course of the experiment for Chevy Impala (UC3) and Kia Soul (UC3). At time zero, the black lights are turned on to initiate photochemical aging.

Effective density measurements are shown in figure 6-3. For the Chevy Impala, a single diameter of 75nm was selected for UC1 and 2 and indicated a singular density very similar to that observed for the first 8 hours of UC3. However, during UC3, a second diameter of 100 nm was selected approximately 6 hours into the experiment and indicates a more fractal population. This may be because the larger agglomerates may still have void spaces have not been filled. Similar to the Hyundai Accent in Chapter 5, the Kia Soul has two

relatively distinct effective densities. The larger particles have densities comparable to that of ammonium nitrate, the smaller ones appear to be fractal, and the 150 nm particles have various densities. All of this indicates different degrees of mixing.

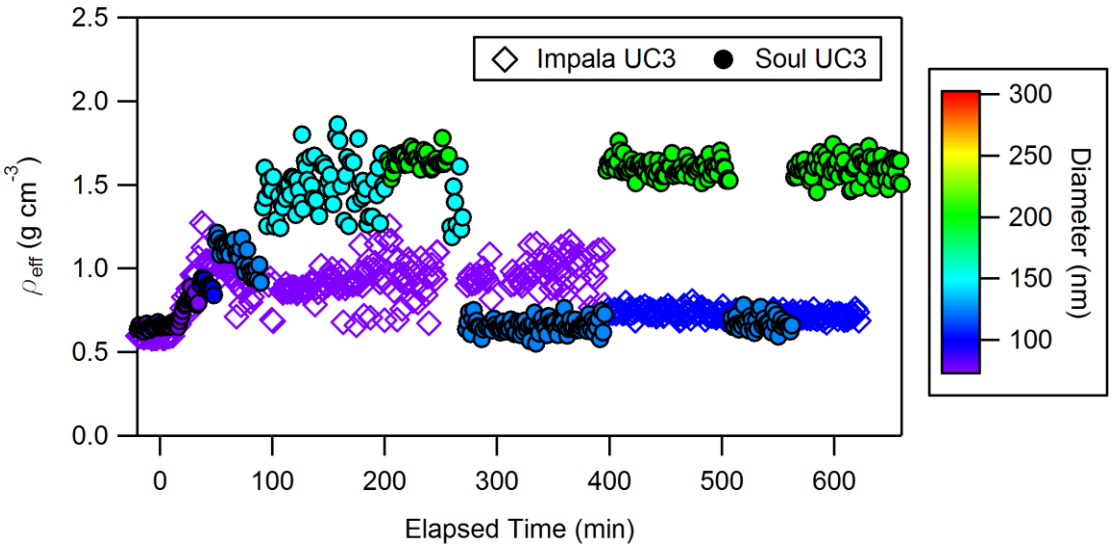

Figure 6-3. Effective Density measurements

The aerosol volatility at 50°C was measured. For the Chevy Impala displays a high initial VFR followed by a slight drop in the VFR. However, this drop is very minimal and is consistent with the low formation of nitrates (figure 6-5). Again, the Kia Soul is similar to the Hyundai; at time zero there is a high VFR. However, as the secondary aerosols begins forming, the VFR drops drastically and is in line with the formation of highly volatile nitrates.

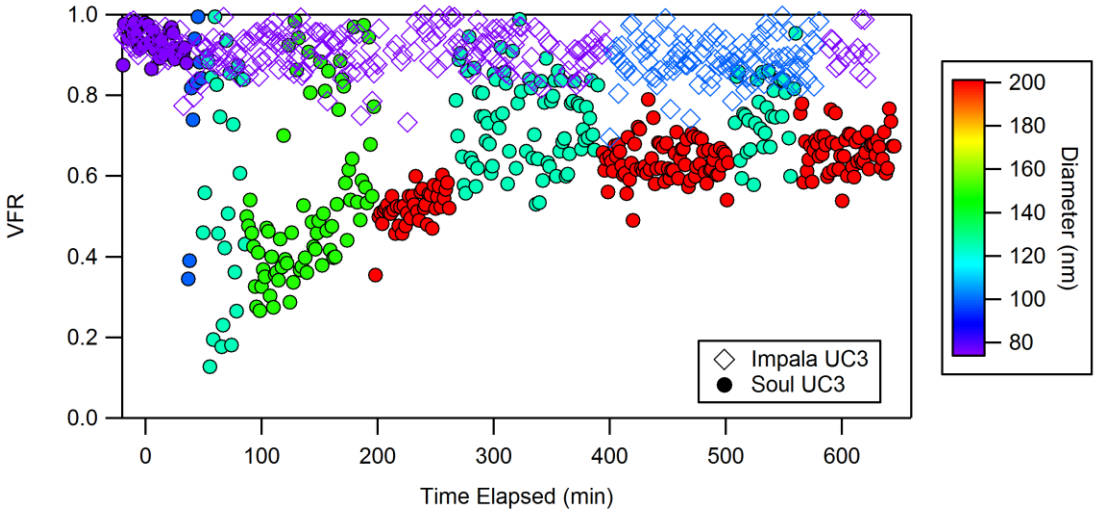

Figure 6-4. Volume fraction remaining measurements for vehicles 1 and 2.

6.2.2 PM Composition

The non-refractory mass fraction data for the Chevy Impala is presented in figure 6-5. These two cycles had comparable mass fractions; the data presented is the average of UC2 (first 450 min) and UC3. UC1 had the highest dilution ratio and thus very minimal SOA formation (Figure D-5). For all three cycles, the organics were the largest mass fraction with little secondary nitrate formation.

The average mass fractions for all three UC cycles for the Kia Soul is presented in figure 6-6. The mass fraction observed for the Kia Soul are similar to that observed for the Hyundai Accent, where the secondary nitrate dominates the aerosol mass.

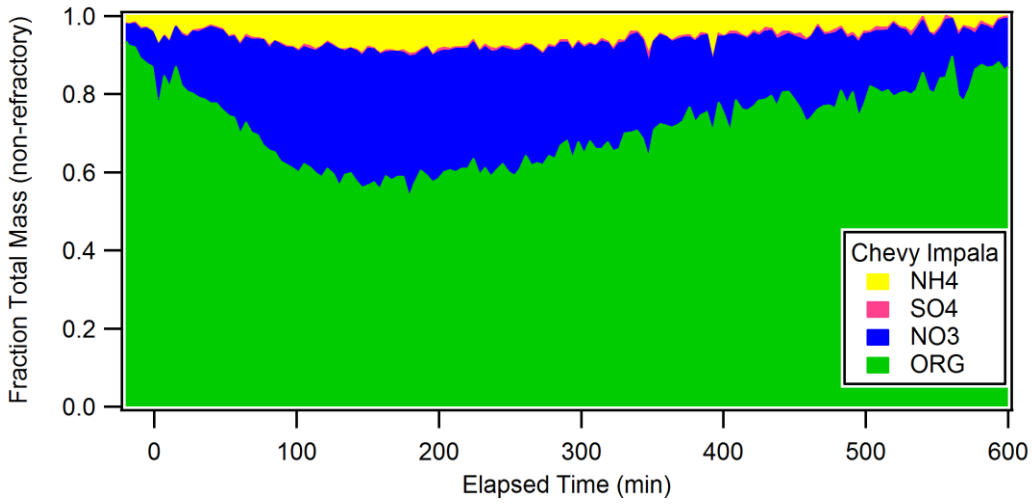

Figure 6-5. Vehicle 1 – Non-refractory mass fractions of average of UC2 and UC3

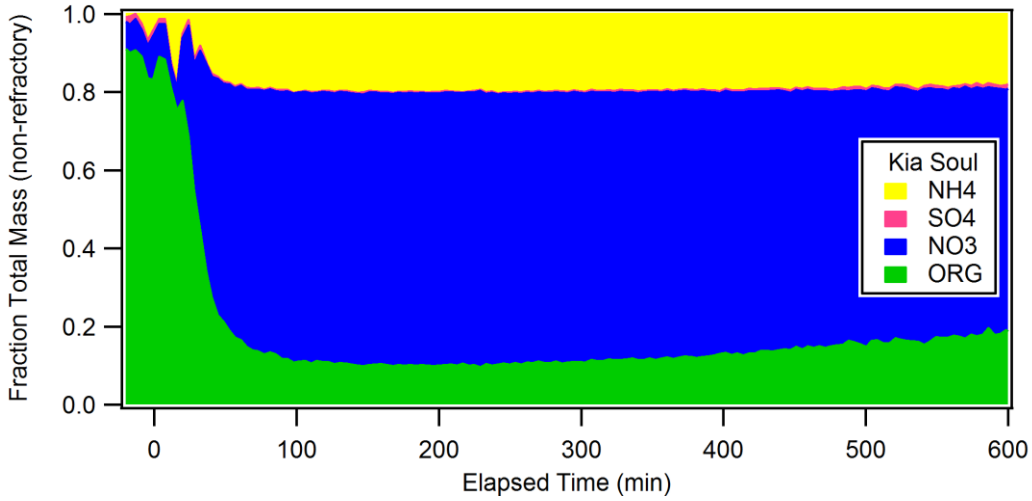

Figure 6-6. Vehicle 2, the first 8 hours are the average of UC 1,2 and 3 with the last two hours being just UC3.

Secondary PM chemical analysis is completed for all tests. However, composition information indicated chemical similarity from cycle to cycle for each of the vehicles. Thus, PM composition analysis is presented for test with the highest organic signal (Figure 6-7). The O:C ratio can provide an indication of the level of oxidation and can range from

0.25 to 1 which indicates highly aged or oxidized organic aerosol (Jimenez et al., 2009). After 8 hours of irradiation, the O:C ratios were ~1.1 for the Kia Soul; this is slightly higher than the O:C reported for the Honda in Part 1 but lower than the Hyundai. However, for the Chevy Impala, the O:C ratio reaches ~2.1. O:C ratios this high have not been previously reported for aged vehicle emissions. The slopes here are similar to those reported by Presto et al. (2014) and Liu et al. (2015). This indicates SOA formation pathways through the addition of both carboxylic acid and alcohol/peroxides (Ng et al., 2011).

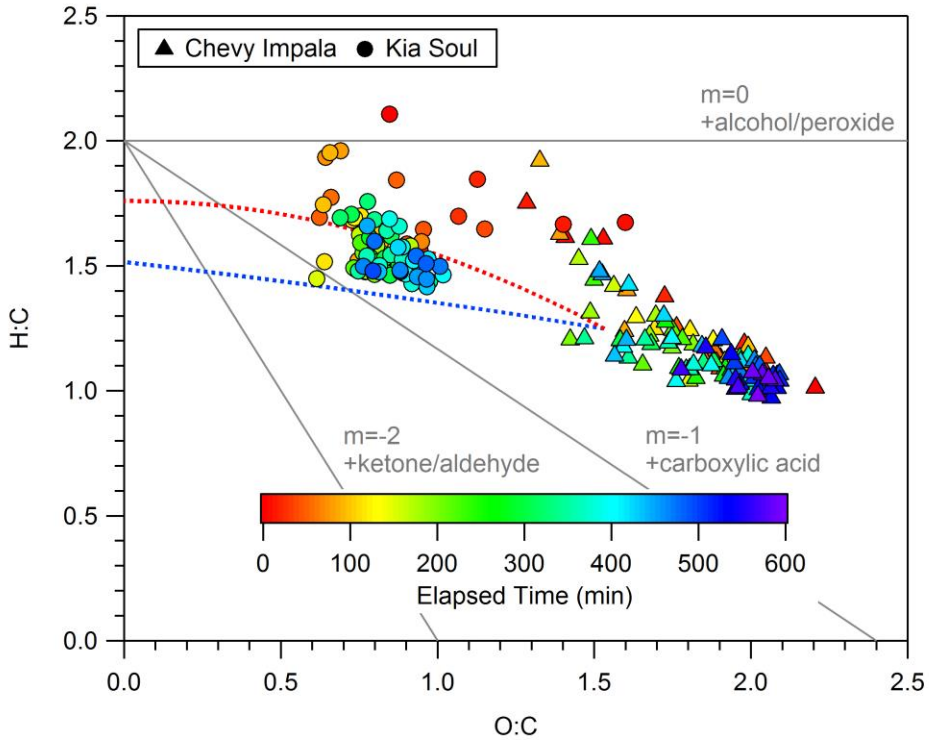

Figure 6-7. Van Krevelen plots for the Chevy Impala (UC3) and Kia Soul (UC2), which are photochemically aged for 10 and 8 hours, respectively.

The fractions of total organic signal at f43 vs. *f*44 are presented in figure (6-8). For both vehicles, there is an initial spread of the data, but they both converge into a cluster upon oxidation. The Kia Soul data fall mainly in the low volatility oxidized organic aerosol (LV-

OOA) region in the upper end of the triangle which is consistent with Presto et al. (2014). However, for the Chevy Impala, the aerosol is highly oxidized at the beginning of the experiment with an indication of slightly different oxidation levels. However, the data converges into tight clusters indicating that the aerosol population reached chemical similarity towards the end of the experiment.

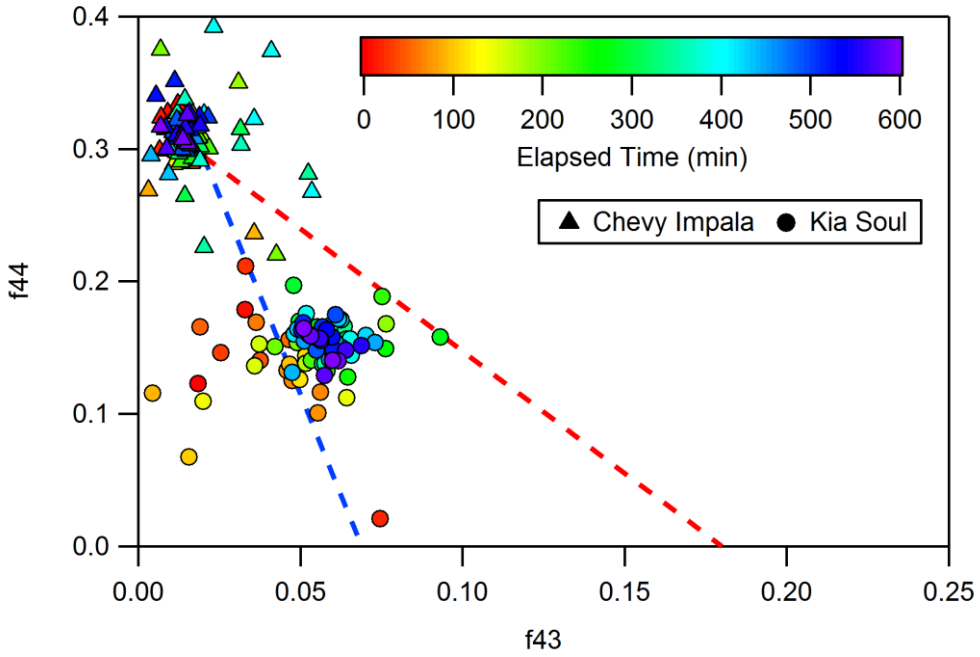

Figure 6-8. f43 vs. f44 for Chevy Impala (UC3) and Kia Soul (UC2)

Previous gasoline emissions studies have identified hydrocarbon ions series ($C_nH_{2n+1}^+$, m/z 29, 43, 57, etc.) with branched alkanes originating from fuel and lubricating oil (Dallmann et al., 2015, Canagaratna et al., 2007). The high resolution mass spectra at time 0 and after 10 and 8 hours of aging are presented in figure 6-9 and 6-10 for the Chevy Impala and Kia Soul, respectively. The Kia Soul is dominated by peaks at m/z 29 (CHO), 43 ($C_2H_3O^+$ and C_3H_7) and 44 (CO_2). However, there is a small contribution at m/z 27, 41

and 55 ($C_nH_{2n-1}^+$) which indicates unsaturated aliphatic compounds such as cyclohexanes and alkenes (Dallmann et al., 2015). For the Chevy Impala the high peak at m/z 44 at t(0hrs) and t(10hrs) is dominated by CO_2 and is consistent with the observation with the aerosols in a highly oxidized state when entering the chamber. There is also little evidence of a signal at *m/z* 43, and *m/z* 29 is dominated by CHO.

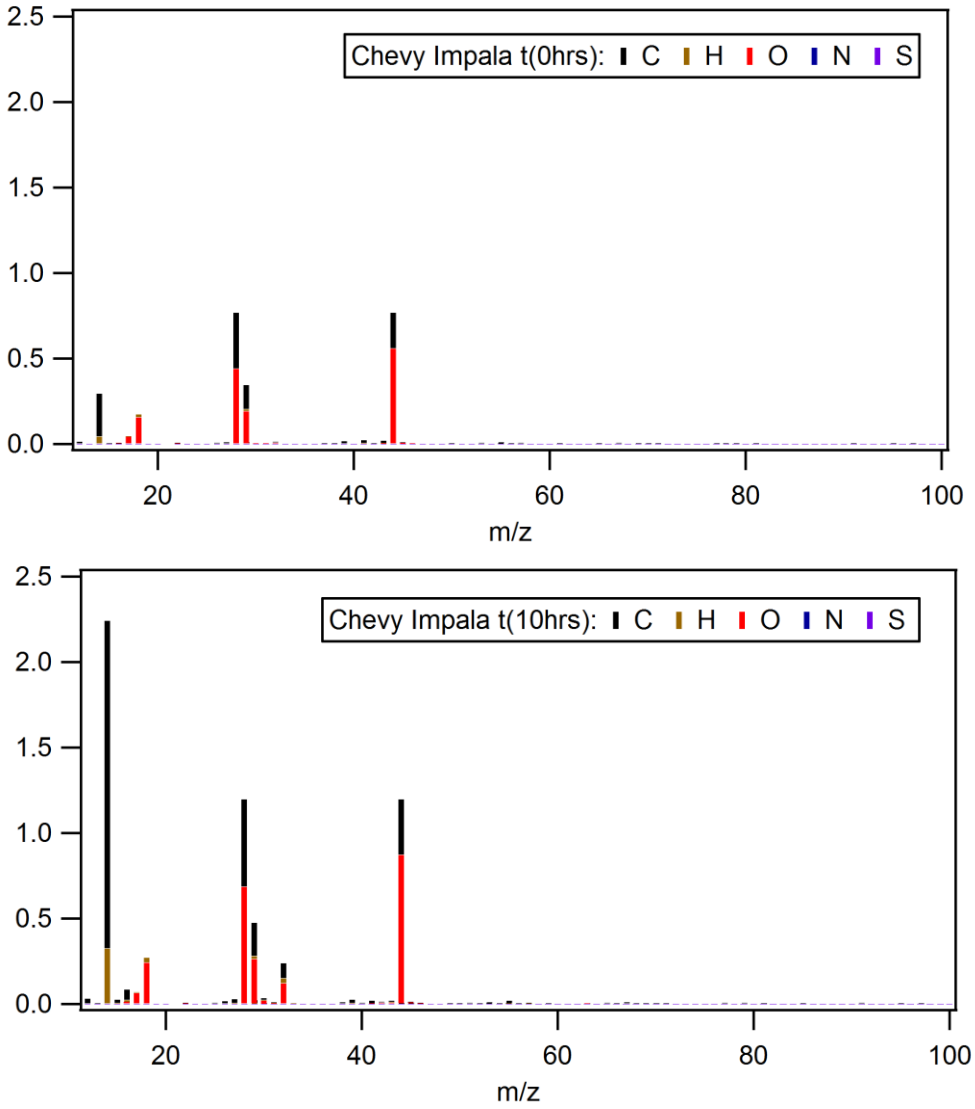

Figure 6-9. Comparison of aerosol at time 0 and 10 hours after lights on for the Chevy Impala (UC3)

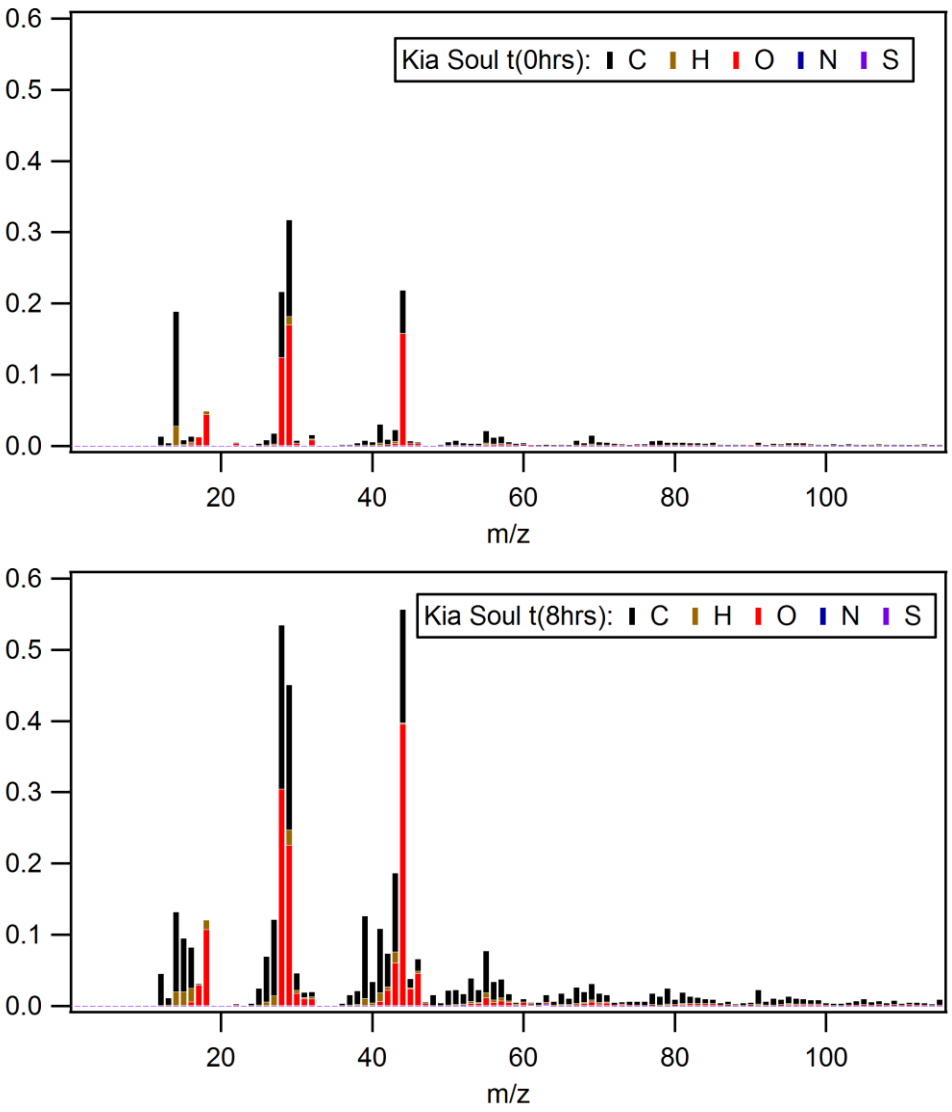

Figure 6-10. Comparison of aerosol at time 0 and 10 hours after lights on for the Kia Soul (UC2)

6.2.3 Aerosol Hygroscopicity

The aerosol hygroscopicity for both vehicles are presented in figure 6-11. At time 0, both vehicles exhibited no CCN activity although there is the presence of organic material. At this point, it is believed that the soot, which is highly non hygroscopic dominates the aerosol mass and the organic material is not hygroscopic enough to activate

the aerosol. These observations are consistent with those seen in Chapter 5. However, within the first hour, the CCN activity for the Impala increases and remain relatively consistent throughout the experiment with a kappa value of ~ 0.05. For the Soul, the CCN activity increases 1.5 hours into the experiment and continues increasing reaching a kappa value ~0.05. This is consistent with the formation of hygroscopic nitrates and the oxidation of POA, which can increase the hygroscopicity. The κ_{GF} vs. κ_{CCN} for Chevy Impala are comparable. However, for the Kia Soul, the κ_{GF} is significantly higher than κ_{CCN}. The markers are sized according to the size selected by the HTDMA.

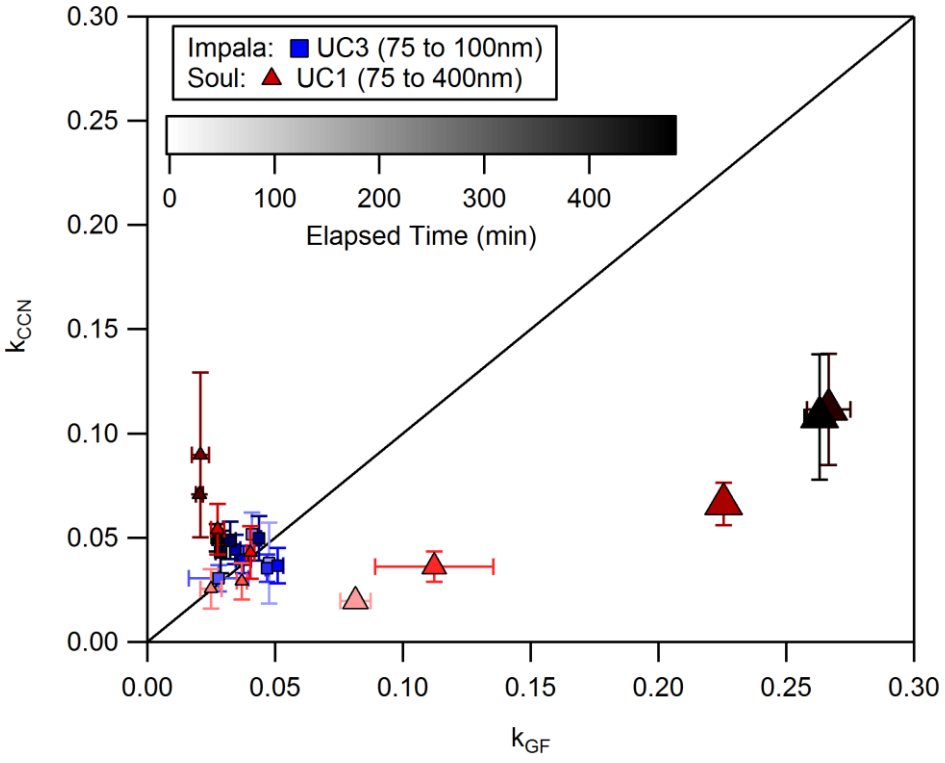

Figure 6-11. κ_{GF} vs. κ_{CCN} Apparent hygroscopicity results for both vehicles. The sizes selected for the HTDMA ranged from 75 to 100nm and 75 to 400nm for the Impala and Soul, respectively. The size of the markers indicates the size selected.

For the Kia Soul, the large sizes (225 and 400nm) indicate a higher kappa value. The larger particles activate more readily and for the Kia Soul, the nitrates may have a larger mass contribution than the smaller sizes. In addition, during the hydration process in the CCN counter and the HTDMA, the smaller fractal particles can undergo restructuring which can effect the growth factor values (Wittbom et al., 2014). Evaporation effects as described in Chapter 5 could affect CCN measurements as well.

6.3 Conclusion

The results show the formation of SOA and ammonium nitrates for both vehicles. The relative mass fraction of secondary nitrate to total organics varied from vehicle to vehicle. In addition, all organic aerosols were found to be highly oxidized with aging, more so than that seen for the Hyundai and the Honda. The Impala in particular had a significantly higher level of oxidation. The formation of hydrophilic compounds due to POA oxidation and the formation of water soluble nitrates modified the water uptake properties of the initially non CCN active aerosols.

6.4 Acknowledgements

Vehicle testing in this study was supported by the Southern California Air Quality Management District. Aerosol hydroscopicity work was supported by the National Science Foundation Award (NSF 1151893). D. Vu would like to acknowledge funding support from the U.S. Environemtnal Portection Agency STAR Fellowship (FP-91751101). The

authors would like to thank Kurt Bumiller for aiding in the design of the chamber, and Mark Villela for the technical contribution in conducting the emissions testing.

6.5 References

Canagaratna, M. R., Jayne, J. T., Jimenez, J. L., Allan, J. D., Al- farra, M. R., Zhang, Q., Onasch, T. B., Drewnick, F., Coe, H., Middlebrook, A., Delia, A., Williams, L. R., Trimborn, A. M., Northway, M. J., DeCarlo, P. F., Kolb, C. E., Davidovits, P., and Worsnop, D. R.: Chemical and microphysical characterization of ambient aerosols with the Aerodyne Aerosol Mass Spectrometer, Mass Spectrom. Rev., 26, 185–222, 2007.

Dallmann, T. R., Onasch, T. B., Kirchstetter, T. W., Worton, D. R., Fortner, E. C., Herndon, S. C., Wood, E. C., Franklin, J. P., Worsnop, D. R., Goldstein, A. H., and Harley, R. A.: Characterization of particulate matter emissions from on-road gasoline and diesel vehicles using a soot particle aerosol mass spectrometer, Atmos. Chem. Phys., 14, 7585-7599, doi:10.5194/acp-14-7585-2014, 2014.

Jimenez, J. L., Canagaratna, M. R., Donahue, N. M., Prevot, A. S. H., Zhang, Q., Kroll, J. H., DeCarlo, P. F., Allan, J. D., Coe, H., Ng, N. L., Aiken, A. C., Docherty, K. S., Ulbrich, I. M., Grieshop, A. P., Robinson, A. L., Duplissy, J., Smith, J. D., Wil- son, K. R., Lanz, V. A., Hueglin, C., Sun, Y. L., Tian, J., Laak- sonen, A., Raatikainen, T., Rautiainen, J., Vaattovaara, P., Ehn, M., Kulmala, M., Tomlinson, J. M., Collins, D. R., Cubison, M. J., E., Dunlea, J., Huffman, J. A., Onasch, T. B., Alfarra, M. R., Williams, P. I., Bower, K., Kondo, Y., Schneider, J., Drewnick, F., Borrmann, S., Weimer, S., Demerjian, K., Salcedo, D., Cot- trell, L., Griffin, R., Takami, A., Miyoshi, T., Hatakeyama, S., Shimono, A., Sun, J. Y., Zhang, Y. M., Dzepina, K., Kimmel, J. R., Sueper, D., Jayne, J. T., Herndon, S. C., Trimborn, A. M., Williams, L. R., Wood, E. C., Middlebrook, A. M., Kolb, C. E., Baltensperger, U., and Worsnop, D. R.: Evolution of Or- ganic Aerosols in the Atmosphere, Science, 326, 1525–1529, doi:10.1126/science.1180353, 2009.

Ng, N. L., Canagaratna, M. R., Jimenez, J. L., Chhabra, P. S., Se- infeld, J. H., and Worsnop, D. R.: Changes in organic aerosol composition with aging inferred from aerosol mass spectra, At- mos. Chem. Phys., 11, 6465–6474, doi:10.5194/acp-11-6465- 2011, 2011.

Presto, A. A., Gordon, T. D., and Robinson, A. L.: Primary to sec- ondary organic aerosol: evolution of organic emissions from mo- bile combustion sources, Atmos. Chem. Phys., 14, 5015–5036, doi:10.5194/acp-14-5015-2014, 2014.

Wittbom, C., Eriksson, A. C., Rissler, J., Carlsson, J. E., Roldin, P., Nordin, E. Z., Nilsson, P. T., Swietlicki, E., Pagels, J. H., and Svenningsson, B. (2014). Cloud droplet activity changes of soot aerosol upon smog chamber ageing, Atmos. Chem. Phys., 14:9831-9854, doi:10.5194/acp-14-9831-2014.

Chapter 7 - Conclusions

The work in chapter 2 is the first to provide information on the shifts in CCN activation due to external to internal particle mixing from controlled laboratory sources. Results showed that activation curves consisting of single and double activation points were consistent with internal and external mixtures, respectively. In addition, the height of the plateau at the activation points were reflective of the externally mixed concentration in the mixture. This indicates that activation curves consisting of multiple activation points may not be multiply charge particles as previously perceived, but reflect externally mixed aerosols of varying solubility where the more soluble material dissolves at the first plateau before the less soluble material does. The work is also the first to show controlled CCN activation of black carbon and subsequent mixtures with more soluble material. CCN activation analysis methods are shown to be robust and maybe applied to more complex aerosol compositions of unknown origin.

The work in chapter 3 was the first closure study to integrate fast time resolved aerosol sizing instrumentation commonly used to measure engine exhaust, with traditional CCN measurements. The method was calibrated in the lab and then applied to chassis dynamometer tests to estimate the impact of six ethanol and iso-butanol gasoline blends on the hygroscopic properties of emissions downstream of a single modern spark ignition direct injection (SIDI) light duty passenger vehicle over two transient drive cycles; Federal Test Procedure (FTP) and California Unified Cycle. This work is beneficial because it provides a) a method to characterize the rapidly changing particle hygroscopicity generated by vehicles operating over transient drive cycles; and b) information related to the

hygroscopicity of emissions derived from the use of different biofuels in a vehicle with modern engine technology.

The work in Chapter 4 investigated the effect of using biodiesel and renewable diesel fuels in modern diesel vehicles equipped with advanced emissions control technologies such as diesel oxidation catalysts, diesel particulate filters (DPF), and selective catalytic reduction systems on aerosol hygroscopicity and cloud condensation nuclei (CCN) activity. Vehicle emission advanced technologies are currently employed and the use of renewable fuels is inevitable. There is very limited information in regards to the particle CCN activity and apparent hygroscopicity during traditional drive cycles and DPF regeneration (especially that of renewable fuels). This work provided insight into the potential impact of alternative fuels and diesel emission control systems on aerosol hygroscopicity with regards to the cloud condensation nuclei (CCN) budget. It presented a) information related to the hygroscopicity of emissions derived from the use of different biofuels in a vehicle with modern engine technology and emissions control technology while operating on transient drive cycles; and b) information in regards to the effect of aftertreatment technology (DPF regeneration) on aerosol hygroscopicity necessary to understand and predict future emissions. The results are the first to provide evidence that changes in fuel oxygenation do not impact overall supersaturated hygrosocopicity for diesel vehicles. However, the aerosols regenerated over the DPF are significantly more hygroscopic and CCN active. This indicates that diesel vehicle emissions will migrate from non-hygroscopic to hygroscopic in nature due to the regeneration of the filters.

Chapters 5 and 6 investigated the effect of photo-oxidation of vehicles exhaust for four GDI vehicles operating over a chassis dynamometer. The experiments showed the formation of SOA and ammonium nitrates for all vehicles; however, the relative fraction of secondary nitrate to total organics varied from vehicle to vehicle. In addition, all organic aerosols were found to be highly oxidized with aging. The formation of hydrophilic compounds due to POA oxidation and the formation of water soluble nitrates modified the water uptake properties of the initially non CCN active aerosols.

The work in this dissertation investigated fresh vehicle emissions from both diesel and gasoline sources. Although it's generally accepted and agree with some of the results in this work that fresh combustion aerosol from vehicle sources are not CCN active with hygroscopicity, it has been shown that under certain operating conditions, such as DPF regeneration, the water uptake properties can be significantly modified. The mixing state also has a strong influence, especially on CCN spectra where evidence of a carrying levels of hygroscopicity is apparent in CCN spectra. It has also been shown that the hygroscopicity of combustion aerosols can be highly modified if internally mixed with a slightly more soluble aerosol species. And lastly, the effect of photochemical aging on aerosol hygroscopicity results in highly oxidized secondary aerosol and water soluble inorganic compounds that greatly modifies CCN activity of combustion aerosol.

Appendix A

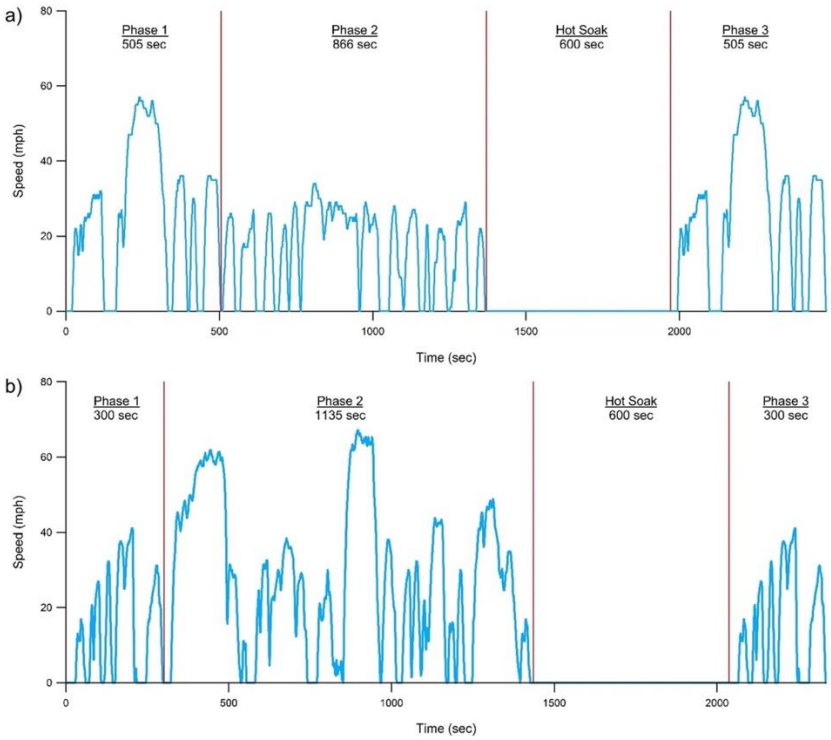

Figure A-1. Drive Cycles a) Federal Test Procedure Cycle b) Unified Cycle

Table A-1. EPA and California Air Resources Board Chassis Dynamometer Driving Schedules

Dynamometer Driving Schedule	Distance (miles)	Duration (sec)	Average Speed (mph)	Top speed (mph)
Federal Test Procedure (FTP)	11.04	1874	21.2	56.7
California Unified (UC)	9.82	1435	24.61	67.2

Appendix B

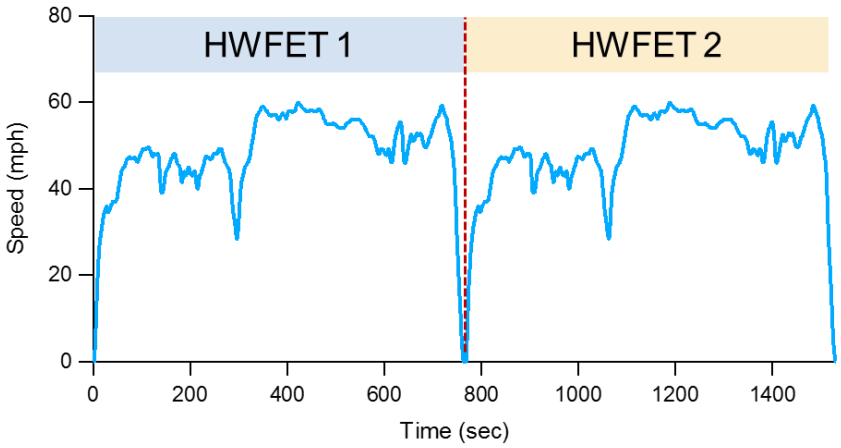

Figure B-1. USEPA Highway Fuel Economy Cycle (HWFET). 10.26 miles long, 765 seconds and has an average speed of 48.3 mph.

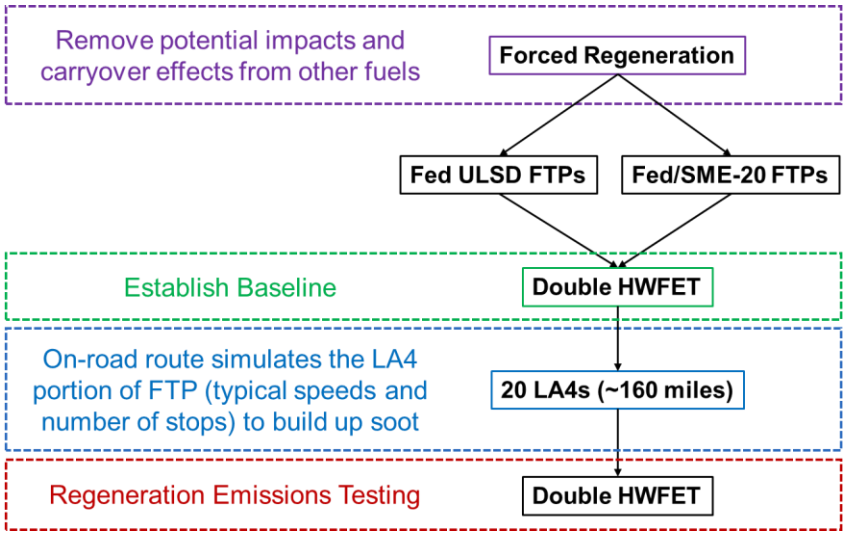

Figure B-2. Regeneration Emissions Testing Protocol

Table B-1. Physical and chemical properties of test fuels

Property	Method	Federal ULSD	Fed/ SME-20	Fed/ AFME-20	Fed/ WCO-20	Fed/ HVO-20	CARB ULSD	CARB/ WCO-20
Sulfur in HC by Oxidative Combustion and Ultraviolet Fluorescence (UVF), ppm	D5453	7.9	6	6.63	6.14	5.75	9.9	9.8
Cloud Point (ºF)	D5773	3.7	10.9	27	11.5	1.3	19.9	21.6
Cetane Number	D613	44.21	45.89	49.32	46.99	51.85	57.54	56.85
Derived Cetane Number by IQT	D6890	45.36	45.67	49.76	47.88	50.86	54.85	54.80
CHNS by combustion (wt%)	D5291							
C (wt%)		86.75	84.97	84.72	84.98	86.55	86.55	84.84
H (wt%)		12.66	12.57	12.65	12.66	13.14	13.14	13.15
N (wt%)		<0.15	<0.15	<0.15	<0.15	<0.15	<0.15	< 0.15
S (wt%)		<0.40	<0.40	<0.40	<0.40	<0.40	<0.40	< 0.40
Density by Digital Density Meter (API Gravity) at 60ºF	D4052	34.98	33.64	34.06	33.64	37.95	39.04	36.95
Distillation	D86							
IBP (ºF)		331.3	344.7	344.3	341.6	333.3	345.4	349.5
T50 (ºF)		509.0	546.3	543.0	545.0	511.7	502.3	538.5
T90 (ºF)		610.7	631.6	627.1	632.5	597.6	622.9	636.6
FBP (ºF)		659.7	661.8	658.0	664.2	652.8	675.3	674.2
Flash Point by Pensky-Martins Closed Cup (ºF)	D93	139	147	147	156	165	153	164
Lubricity by HFRR at 60ºC (microns)	D6079	315.5	180.5	186	172.5	386	415.0	156.5
BTU Gross and Net by Bomb Calorimeter (Btu/lb)	D240	19,572	19,108	19,092	19,058	19,731	19,813	19,322
Viscosity by Capillary Viscometer (mm^2/s at 40ºC)	D445	2.654	2.809	2.896	2.898	2.543	2.536	2.907
Oxygen by Atomic Emission Detection w/ extraction prep	GC-AED-O w/ prep	0.03	3.14	3.13	2.98	0.02	0.02	2.47
Hydrocarbon Types by Fluorescent Indicator Absorption (FIA)	D1319							
Aromatics (vol%)		34.2	41.6	41.6	40.0	23.4	20.0	30.0
Olefins (vol%)		1.9	2.4	2.3	2.0	2.0	2.1	2.5
Saturates (vol%)		63.9	56.0	56.1	58.0	74.6	77.9	67.5

Table B-2. Vehicle 1 kappa values

FUEL	kappa			standard deviation		
	Phase 1	Phase 2	Phase 3	Phase 1	Phase 2	Phase 3
CARB ULSD	5.46E-03	6.19E-03	5.36E-03	1.03E-03	1.09E-03	9.92E-04
CARB/WCO-20	1.96E-02	2.58E-02	1.57E-02	1.48E-02	1.90E-02	8.71E-03
FED ULSD	2.59E-03	2.52E-03	2.34E-03	4.63E-04	2.89E-04	1.24E-04
FED/WCO-20	1.37E-02	2.06E-02	1.48E-02	3.46E-03	4.49E-03	8.06E-04
FED/HVO-20	1.12E-02	1.70E-02	1.59E-02	1.11E-03	8.07E-04	1.14E-03
FED/AFME-20	1.53E-02	3.86E-03	3.61E-03	9.69E-03	1.36E-03	6.48E-04
FED/SME-20	1.09E-02	1.18E-02	1.11E-02	1.14E-03	1.95E-04	8.79E-04

Table B-3. Kappa values associated for the double HWFET tests for Vehicle 1. * denotes the values that reached the detection limits of the SMPS and CCNC

Baseline	**FED ULSD REGEN1**	**FED ULSD REGEN2**	**FED ULSD/SME-20 REGEN1**	**FED ULSD/SME-20 REGEN2**
3.76E-03	3.26E-01	7.95E-02	1.68E-01	3.69E-01
3.91E-03	3.70E-01	2.30E-01	8.91E-02	3.78E-01
3.81E-03	3.19E-01*	2.34E-01	1.55E-01	4.65E-01
4.14E-03	3.88E-01*	2.72E-01	1.44E-01	
4.14E-03	4.49E-01	3.15E-01	1.70E-01	
4.43E-03				
4.39E-03				
4.08E-03				
3.96E-03				
4.15E-03				
3.95E-03				
5.39E-03				

Table B-4. Kappa values associated for the double HWFET tests for Vehicle 2. * denotes the values that reached the detection limits of the SMPS and CCNC.

FED ULSD REGEN1	FED ULSD REGEN2	FED ULSD REGEN3	FED ULSD/SME-20 REGEN1	FED ULSD/SME-20 REGEN2
4.26E-01*	7.87E-01	6.63E-02	4.99E-01	3.50E-01
4.67E-01	7.58E-01*	1.31E-01	5.55E-01	3.09E-01
4.31E-01*	7.11E-01*	1.12E-01	5.19E-01	3.23E-01
4.21E-01*	8.43E-01	6.61E-02	5.15E-01	3.56E-01
4.19E-01			5.23E-01	3.81E-01
			5.26E-01	4.09E-01

Table B-5. Averaged kappa values during regeneration

	FED ULSD	FED ULSD/SME-20
Vehicle 1	0.298±0.0974	0.242±0.130
Vehicle 2	0.434±0.342	0.439±0.88

Appendix C

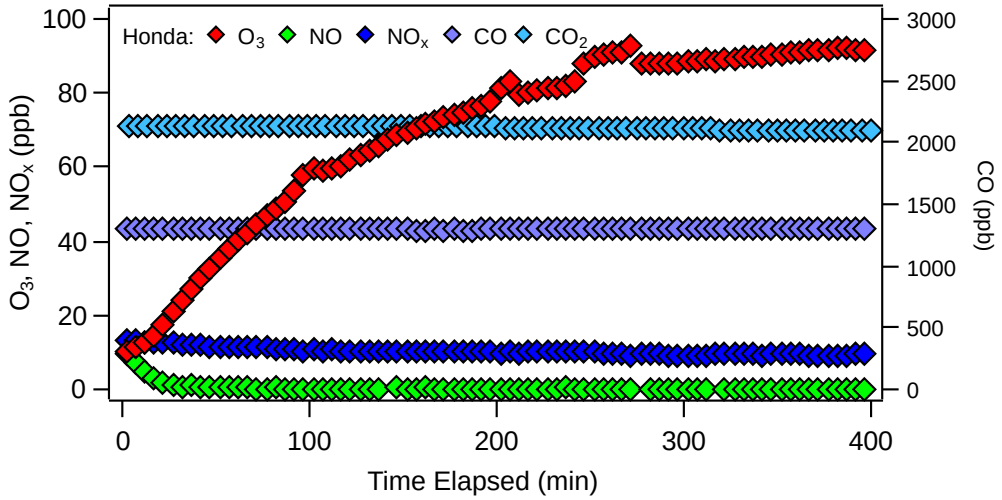

Figure C-1. Measured gas phase concentrations for Honda.

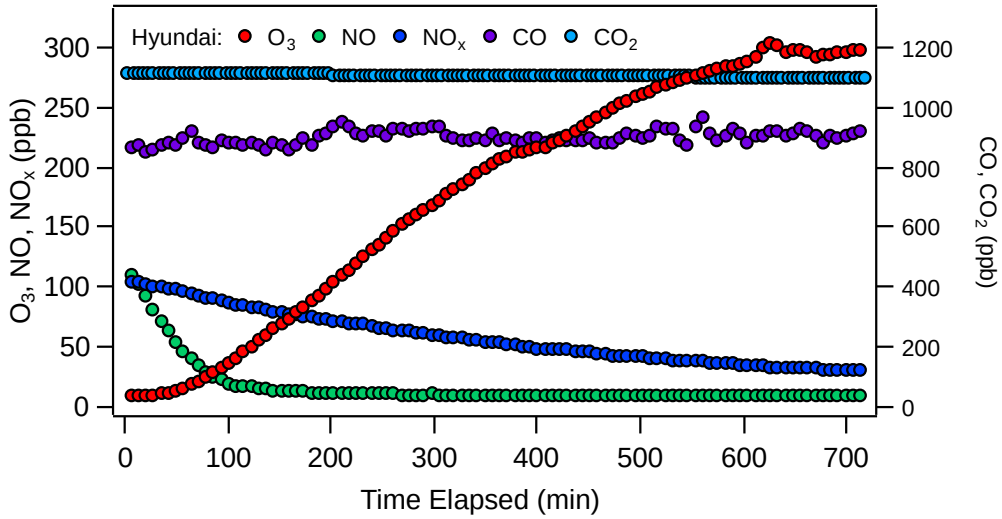

Figure C-2. Measured gas phase concentrations for Hyundai

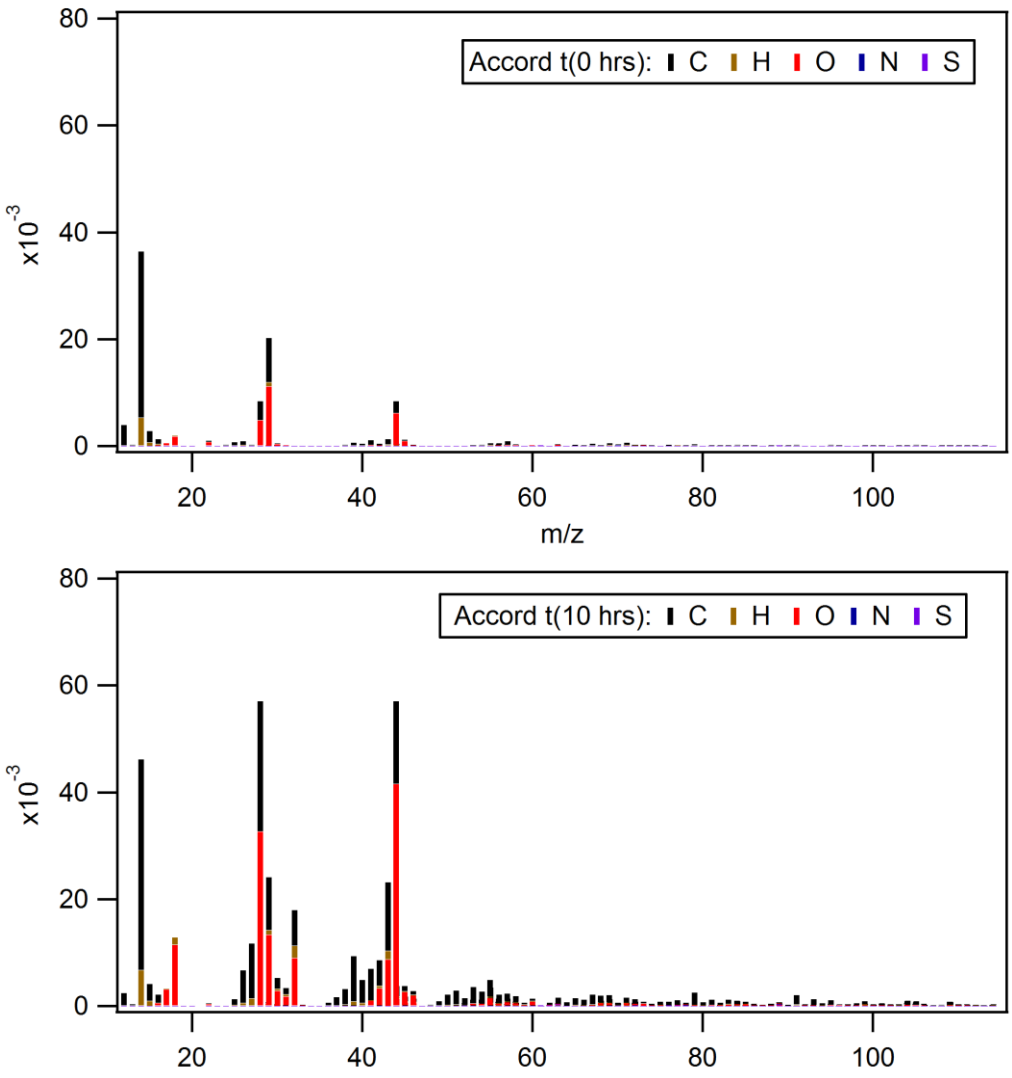

Figure C-3. Comparison of aerosol at time 0 and 10 hours after lights on for the Honda

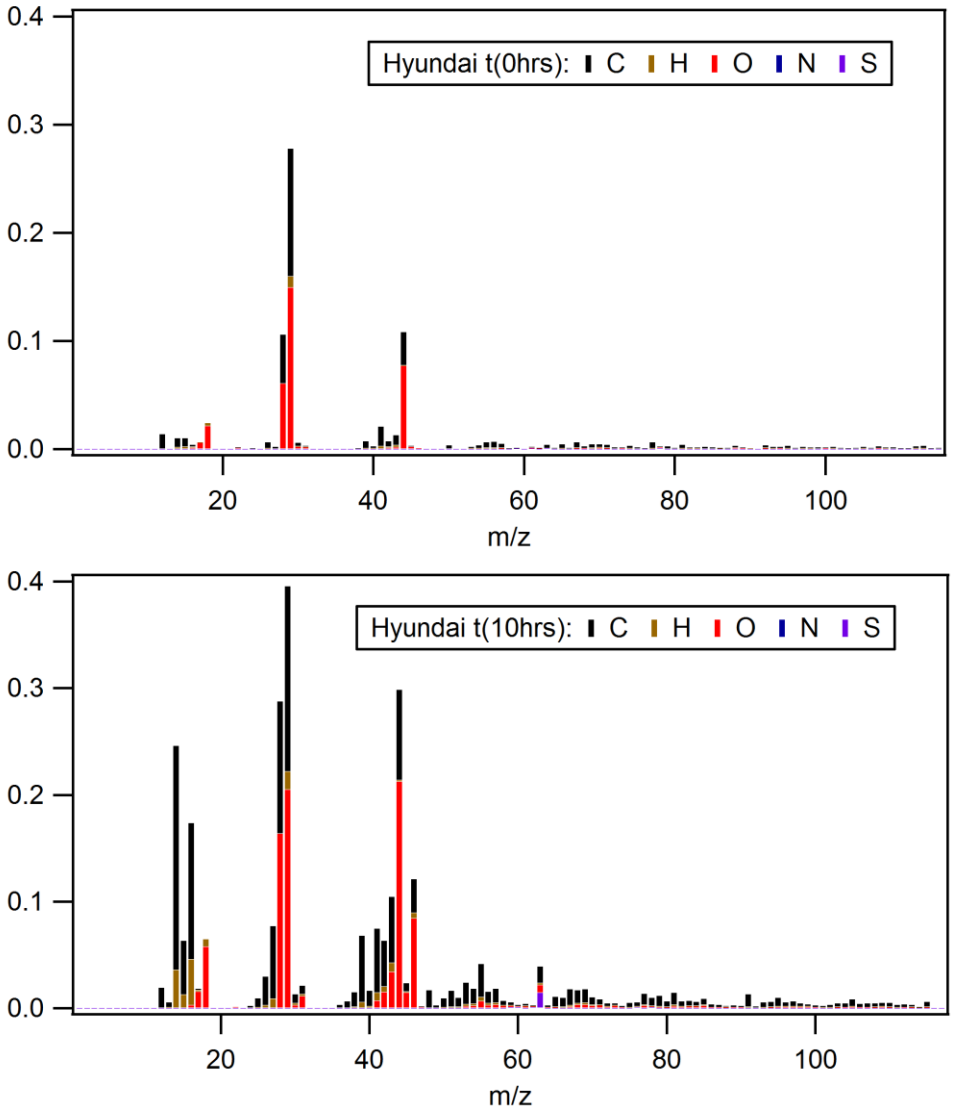

Figure C-4. Comparison of aerosol at time 0 and 10 hours after lights on for the Hyundai

Appendix D

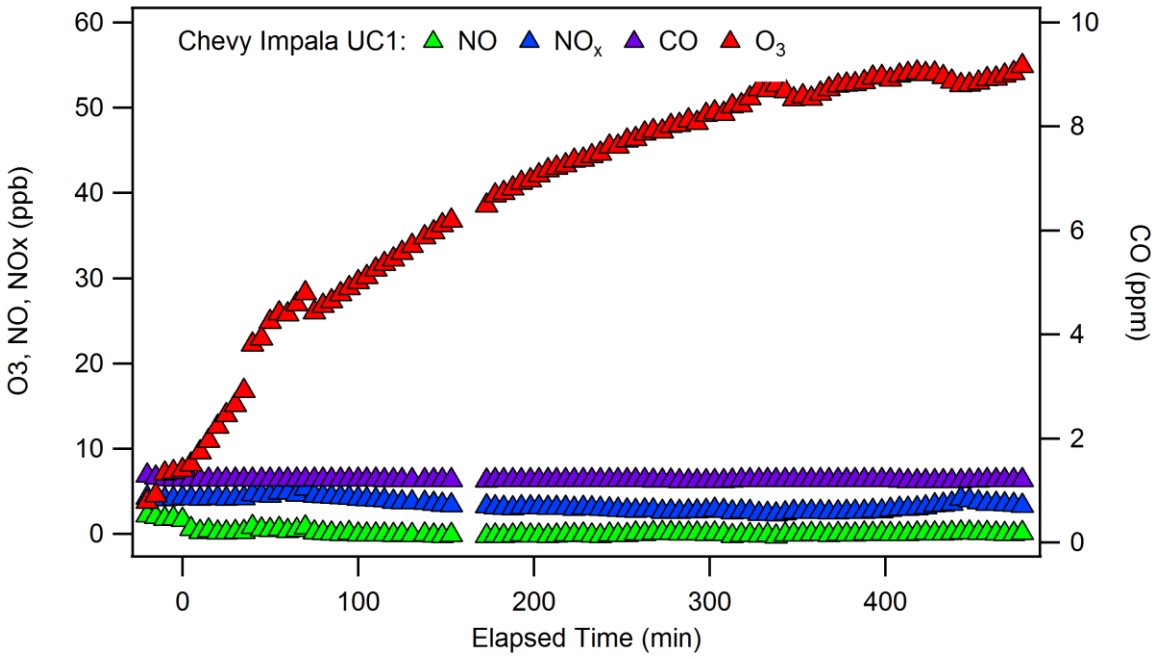

Figure D-1. Gas Data for Chevy Impala UC1

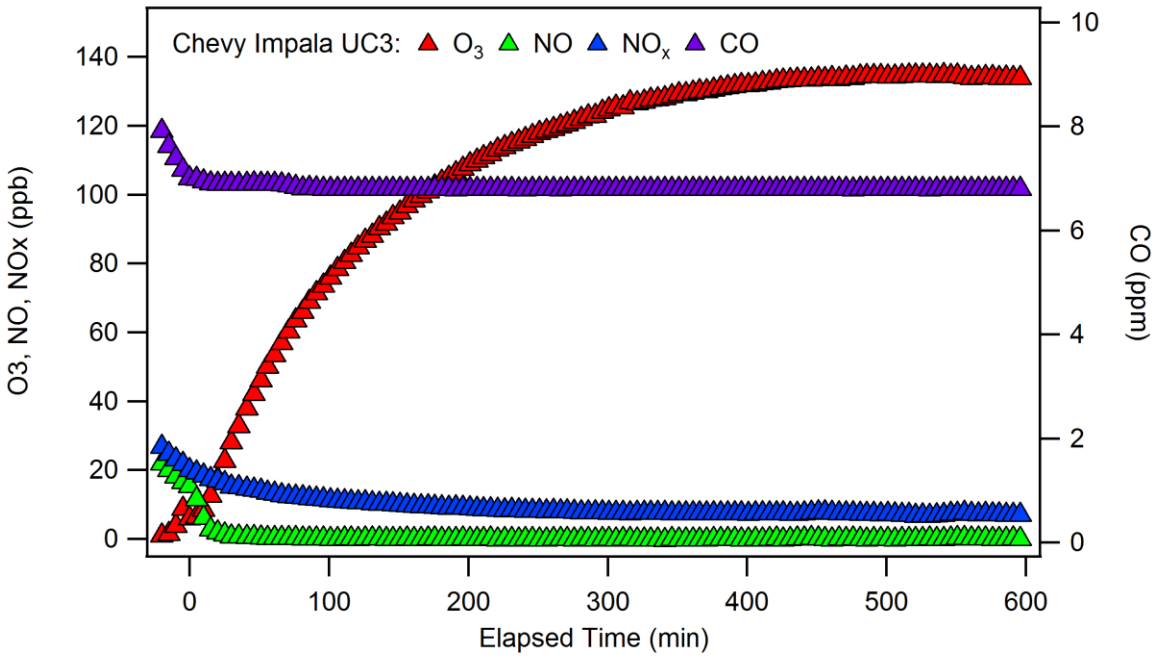

Figure D-2. Gas Data for Chevy Impala UC2 and UC3 are comparable. UC3 is presented.

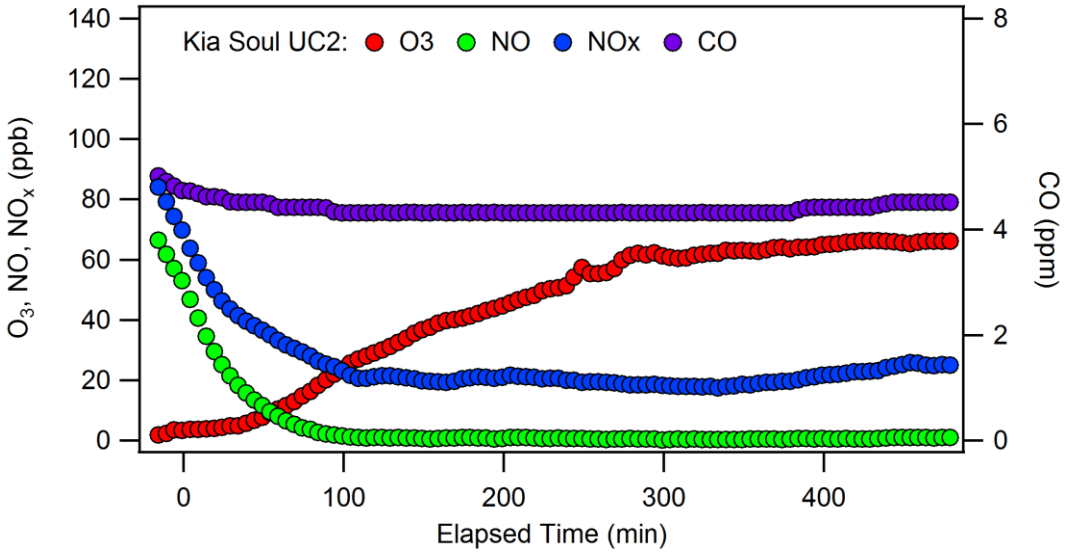

Figure D-3. Measured gaseous concentrations for the Kia Soul. UC1 and UC2 are similar. UC2 is presented

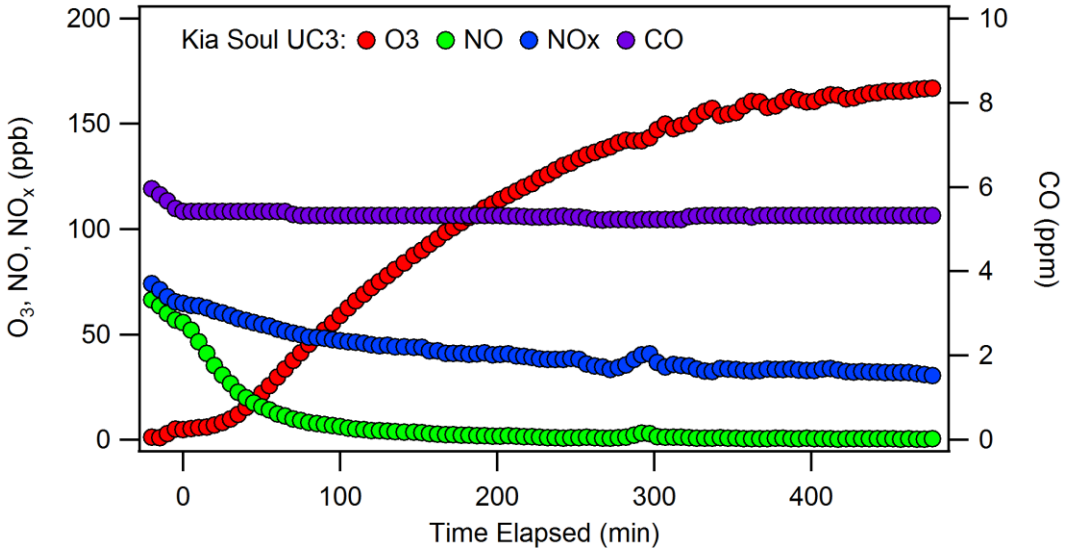

Figure D-4. Measured gaseous concentrations for Kia Soul UC3

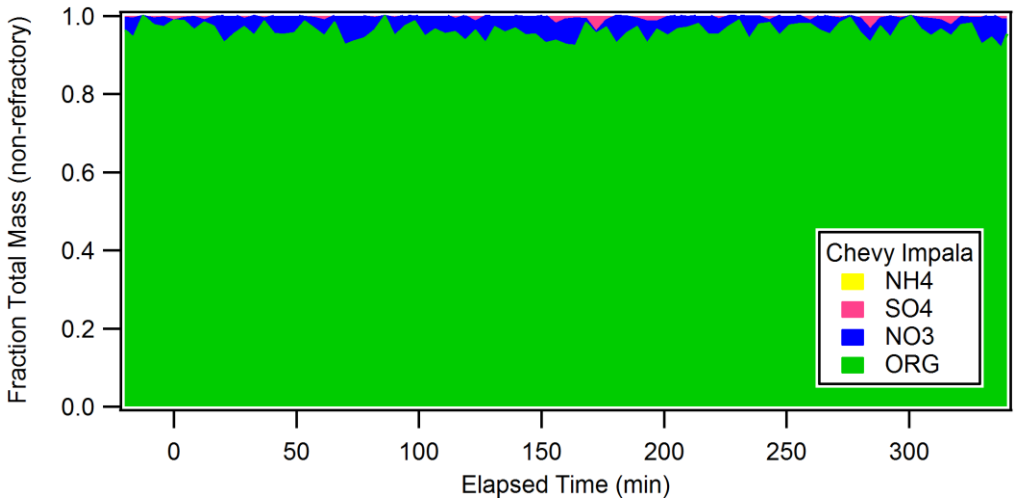

Figure D-5. Mass fraction of nonrefractory aerosol measured by thr AMS for the Chevy Impala (UC1). Data are not wall loss corrected.